Intrinsic and nonlinear coupling of nanomechanical SiN string resonators

Dissertation submitted for the degree of *Doctor of Natural Science*
(Dr. rer. nat.)

by
Katrin Gajo

at the

Universität Konstanz

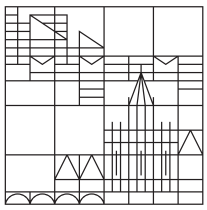

Faculty of Sciences
Department of Physics

Konstanz, 2019

Date of the oral examination: 25.07.2019

1. referee: **Prof. Dr. Eva M. Weig**

2. referee: **Prof. Dr. Elke Scheer**

Zusammenfassung

Diese Arbeit widmet sich der Untersuchung zweier gekoppelter, beidseitig aufgehängter nanomechanischer Silizium-Nitrid Resonatoren hoher Güte. Insbesondere sind die lineare mechanische, sowie die nichtlineare dispersive Modenkopplung der fundamentalen Biegemoden der beiden Resonatoren Gegenstand dieser Forschung.
Um eine rein mechanische Modenkopplung dieser Biegemoden zu realisieren, muss ein Energieaustausch zwischen den Resonatoren stattfinden können. Die speziell konstruierte Geometrie eines gemeinsamen Aufhängepunktes der Resonatoren ermöglicht eine mechanische, durch Verspannung im Silizium-Nitrid begünstigte Kopplung der fundamentalen Biegemoden des Systems. Eine dielektrische Antriebstechnik erlaubt es, die Eigenfrequenzen der Moden zu verstimmen und somit zwei, oder drei Moden des Systems in Resonanz zu bringen. Im Falle der 3-Moden Resonanz spielt sowohl die dielektrische Modenkopplung zwischen den Moden eines Resonators, als auch die rein mechanische Kopplung zwischen den Moden der beiden Resonatoren eine Rolle. Die Kopplung der Moden kann mittels eines sogenannten genetischen Algorithmus quantifiziert werden. Des Weiteren kann durch Lösen des Eigenwertproblems der gekoppelten Bewegungsgleichungen der Moden deren Polarisation untersucht werden.
Zusätzlich zum dielektrischen Antriebsmechanismus können weitere statische elektrische Felder an das System angelegt werden, welche wiederum einen eklatanten Einfluss auf die Eigenfrequenzen und die Verstimmbarkeit selbiger haben. Dieser Zusammenhang wird im Verlaufe der vorliegenden Arbeiten systematisch untersucht. Dabei kann gezeigt werden, dass die Verstimmbarkeit der Frequenz durch Anlegen eines zusätzlichen elektrischen Feldes je nach Modenpolarisation um bis zu 180% gegenüber dem Fall ohne zusätzliches Feld erhöht, oder die Verstimmbarkeitsrichtung sogar umgekehrt werden kann.
Neben der linearen mechanischen Kopplung ist es möglich eine nichtlineare, dispersive Modenkopplung zu erhalten, sofern die Resonatoren stark angetrieben werden. In diesem Fall können die Resonanzen der Moden nicht mehr mit einer linearen Lorentzkurve beschrieben werden, sondern werden im Rahmen der Duffing-Nichtlinearität betrachtet. Wird nun eine der Moden nichtlinear getrieben, so erfahren die jeweils gekoppelten Moden eine Frequenzänderung in ihrer Eigenfrequenz, die von der Amplitude der getriebenen Mode abhängt. Sowohl die Kopplungsstärke dieser nichtlinearen dispersiven Modenkopplung, als auch die Duffing-Nichtlinearität der jeweils getriebenen Mode hängen in nichttrivialer Weise von der Modenpolarisation ab. Um diese Abhängigkeit präzise zu beschreiben wird ein theoretisches Modell auf Basis nichtlinear gekoppelter Moden entwickelt und qualitativ mit Messdaten verglichen.

Abstract

This work investigates on two coupled, doubly clamped silicon nitride string resonators with high quality factors. In particular, this thesis will focus on linear mechanical as well as nonlinear dispersive coupling of the fundamental flexural modes of the two resonators.
For realizing purely mechanical mode coupling, it is necessary to allow for energy transfer between the resonators. The specially designed geometry of one shared clamping point of the resonators favors the exchange of oscillatory energy, and hence enables a pure mechanical, strain-mediated mode coupling. A dielectric actuation technique allows for detuning of the modes' eigenfrequencies, and thus bringing two, or even three modes of the system in resonance. In case of the 3-mode resonance, dielectric coupling of the modes within on resonator, as well as mechanical mode coupling between the modes of the two resonators can be observed. The multi-mode coupling can be quantified utilizing a so called genetic fitting algorithm. Furthermore, the modes' polarizations can be obtained by solving the eigenvalue problem of the coupled equations of motion of the system.
In addition to the dielectric actuation technique, it is possible to expose the resonators to a secondary static electrical field, which has a strong impact on the eigenfrequencies and the tunability of the modes. This work provides a systematic analysis of this correlation. It is shown, that the tunability of the modes can be increased by applying an additional electric field by up to 180% compared to the case without the additional field, depending on the mode polarization. For some mode polarizations even the tuning direction can be changed.
Besides the linear mechanical coupling, it is possible to realize a nonlinear, dispersive mode coupling, if the resonators are driven strongly enough. In this case, the frequency response of the modes can no longer be described with a Lorentzian curve, but within the framework of the Duffing model. If one of the modes is driven in the nonlinear response regime, the corresponding coupled modes will experience a change in eigenfrequency, which depends on the amplitude of the driven resonator. The coupling strength of this nonlinear dispersive mode coupling, as well as the Duffing nonlinearity of the respective driven mode strongly depend on the mode polarization in a non-trivial way. A theoretical model based on nonlinearly coupled modes that describes this polarization dependence is developed and a qualitative comparison with the measurement data is made.

Contents

Introduction

The primary goal of technological research in these times is to improve and simplify our everyday life, be it in terms of communication, transportation and safety or living itself. We use cellphones with micromechanical gyroscope sensors for automatic rotation of the displayed pictures and wireless headphones that convert electromagnetical signals in sound waves. We drive cars with spacial and speed sensors that keep track of the surrounding traffic and give a warning when cars come too close, or they even drive all autonomously. The smart fridge at home sends a message to our phone when we run out of cheese, so the navigation system of our car immediately searches for the nearest grocery store. New technologies are an essential part of our society and all these technological achievements owe their success to the size and integrability of micro-electromechanical systems (MEMS). Therefore, the aim of technological research in this area is to further decrease the size for higher sensitivity and integrability. This leads to devices with lower masses, and thus potentially higher sensitivity, turning from micro-electromechanical to nano-electromechanical systems (NEMS). Also, the operational area of NEMS can be increased by coupling the system to other physical degrees of freedom such as optical, electrical, plasmonic, spin or mechanical properties.

Here, opto-electromechanical and nano-electromechanical systems -consisting of one or more mechanical resonators coupled to an optical cavity, or an electric field, open up new possibilities in application and integration of devices. Starting from mass and force sensing in the yoctogram[1] and zeptonewton[2] range, over the detection of gravitational waves,[3] to all-integrated hybrid systems:[4–6] the concept of mechanical harmonic oscillators coupled to other degrees of freedom like optical modes gives rise to versatile applications and research topics. For instance, backaction evading[7,8] measurements have been performed by coupling two mechanical resonators inductively to a microwave resonator. Furthermore, a stable entanglement of mechanical resonators[9] was achieved with a system consisting of two mechanical drum resonators coupled through a superconducting microwave transmission-line resonator. Even the quantum shot-noise limit (zero-point fluctuations in the electromagnetic field limiting the resolution of optical interferometric devices) of optical cavities could be reached,[10] and yet, measurements go beyond this limit by injecting squeezed light into an optomechanical cavity,[11,12] enhancing the sensitivity of the optomechanical system. These might be steps towards quantum computing, which holds the possibility of faster information transport and processing, what in turn will be advantageous for sensing applications.

Besides this, optomechanical and electromechanical systems open the doors to micro and nano-

scale topological physics[13–15] and optomechanical signal transduction.[16,17] This allows for new ways of signal processing[18,19] in nano-electromechanical sensors, by realizing phonon lasing[20] as a means of signal conversion, or even phononic crystals that allow for phononic band-gap engineering[21–23] by utilizing electromechanical resonators. One could think of a whole array of such resonators which could be employed for signal filtering, transduction or even amplification.

This in turn, demands an implementable way to transfer signals from one resonator to another. One possibility to meet this requirement is to couple the resonators, or single modes of these resonators mechanically.

The coupling of mechanical modes has become an increasing research topic.[24–27] For example, parametric coupling[6,28–31] can be utilized to achieve strong mechanical mode coupling, and therefore enabling further investigations on the coupled system and mode dynamics. However, to realize parametric coupling usually additional tuning mechanisms have to be established in order to bring the system in the strong coupling regime.

Strong mechanical mode coupling can also be achieved by using linear strain-induced coupling and can be expanded from intra-resonator coupling within one single resonator[24,25,27,32] to a multi-resonator geometry[33–35] with inter-resonator mode coupling. In this way no additional tuning mechanisms are needed to bring the system in the strong coupling regime, as it is intrinsically strongly coupled. This may allow for the realization of whole resonator arrays, opening new ways of information transport and signal processing.

Another possibility to achieve mode coupling is to employ the inherent nonlinearities many mechanical resonator systems offer: nonlinear mode coupling can be achieved by taking advantage of internal resonances,[36–38] or the nonlinear system allows for dispersive mode coupling.[39,40]

In this work an accurate study of two parallel, mechanically coupled silicon nitride string resonators is presented. The high quality-factor resonators are doubly clamped and share one of these clamping points, the geometry of which is crucial to the mechanical coupling. A dielectric actuation technique[41] is applied to the resonators, which additionally allows for tuning the eigenfrequencies of the flexural modes of the resonators.

We start in chapter 1 with the basic assumptions of how to mathematically describe such string resonators, expanding the model of two coupled harmonic oscillator to a system of four coupled harmonic oscillators, giving rise to multi-mode avoided crossings, followed by an explanation on the working principle of strain-induced mode coupling. The resonators subject to this work also offer nonlinear dispersive mode coupling. A theoretical model is developed for this work in cooperation with Dr. Gianluca Rastelli, to describe the mode polarization dependent dispersive coupling and also the polarization dependence of the nonlinear Duffing resonator.

Subsequently geometrical considerations in terms of finite element simulations are made in chapter 2 to find the most suitable resonator geometry and dimensions for the upcoming exploration of the coupled mode system.

A brief introduction on sample fabrication is given in chapter 3, as all samples investigated throughout this work were explicitly fabricated for this purpose. Here, also the sample geometries conceived to meet the needs of the experimental observation of strong mechanical and dispersive mode coupling in a system of two adjacent string resonators are explained. Furthermore, this chapter gives a detailed description of the working principle of the actuation and

detection techniques, available through the elaborated sample design. This includes an explanation of the dielectric tuning behavior of the modes
The experimental investigation of strain-induced strong mode coupling of the two resonators is subject of chapter 4. It can be shown, that several of the fundamental flexural modes of the system can be brought in resonance, giving rise to two-mode and even three-mode resonances, including inter-string and intra-string mode coupling.
This is followed by a detailed study on the impact of static electrical fields on the frequency tuning behavior of the resonator modes in chapter 5. If an additional electric field is applied to the resonators, the tuning strength can be strongly enhanced, or even the tuning direction can be inverted, depending on the mode polarization.
We investigate the nonlinear behavior of the coupled modes in chapter 6, showing that the nonlinear Duffing curves of the modes' response, as well as the dispersive mode coupling strongly depend on the mode polarizations. The comparison of measured data with the theory elaborated in chapter 1 reveals a very god agreement for the polarization dependent Duffing nonlinearities of the modes.
Finally a summary of this work followed by an outlook on further investigations and possible applications is given in chapter 7. The system investigated in this work opens the opportunity to more possibilities on active manipulation of the system of coupled resonators, and thus brings us one step further to new ways of signal transduction and information processing.

Chapter 1

High-Q string resonators: the basics

This chapter gives a brief introduction to the fundamental background and basic assumptions made to theoretically describe the electromechanical system presented in this work. Starting from linear harmonic oscillators, we will extend the classical model of two strongly coupled harmonic oscillators to the case of four harmonic oscillators. In addition, the prominent coupling mechanisms of two silicon nitride string resonators will be explained, followed by a short discussion on nonlinear Duffing resonators. A theoretical model is evaluated to describe the mode polarization dependence of the Duffing nonlinearity and the nonlinear dispersive coupling.

1.1 Linear harmonic oscillators

Controlling NEMS implies controlling the interaction of a resonator with a thermal, electrical and/or mechanical environment. This interaction always means an exchange of energy between the resonator and the environment. As a measure for this energy transfer we take the Q factor -a dimensionless parameter- of the resonator in the linear regime. The Q factor is defined as the ratio of the energy stored in the movement of the resonator, to the dissipated energy per oscillation period:

$$Q = 2\pi \frac{\text{Stored energy}}{\text{Dissipated energy per oscillation period}}.$$

The system introduced in this work consists of two parallel silicon nitride string resonators fabricated on a silicon dioxide substrate. On account of the high-stress silicon nitride used in this work, which leads to a 1D stress of 1,46 GPa in the string resonator,[42] the Q factor of these resonators is in the range of 200 000. In the linear frequency response regime, the Q factor can be set in relation to the intrinsic resonance frequency ω_0^* (for more details see chapter 3.2.1) and the full width at half maximum $\Delta\omega$ of the resonator:

$$Q = \frac{\omega_0^*}{\Delta\omega}.$$

The intrinsic eigenfrequency of the fundamental flexural mode of a single, doubly clamped, freely suspended string resonator (as shown in Fig. 1.1) with length L and cross section A can be described in the framework of the elastic Euler-Bernoulli beam-theory:[43–45]

$$\omega_0^* = \frac{\pi^2}{L^2}\sqrt{\frac{(EI)}{(\rho A)}}\sqrt{1+\frac{(\sigma A)L^2}{(EI)\pi^2}}. \tag{1.1}$$

Here, E is the Young's modulus, I is the area momentum of inertia and ρ and σ are the mass density and the tensile-stress, respectively.

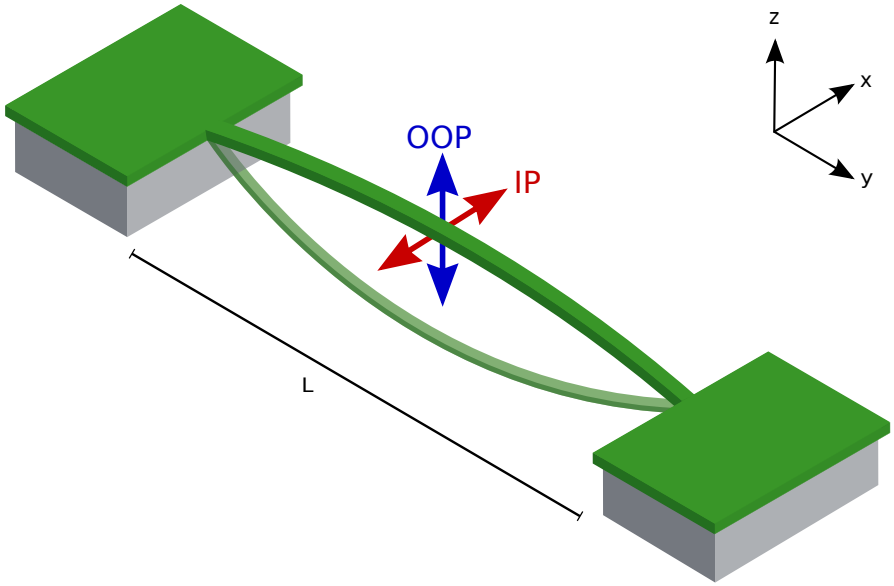

Figure 1.1: Sketch of a single, doubly clamped, freely suspended silicon nitride string resonator with length L. The arrows indicate the respective flexural mode: red shows the in-plane mode (IP), blue the out-of-plane mode (OOP).

If we assume one single silicon nitride string resonator with an in-plane (IP, in the direction of the surface of the chip) and out-of-plane (OOP, perpendicular to the surface of the chip) fundamental flexural mode, we can mathematically handle these modes as individual harmonic oscillators 1 and 2 with effective masses m_1 and m_2 and spring constants k_1 and k_2. Supposing there is a coupling between these resonators, we can write the equations of motion as[46]

$$\begin{aligned} m_1\ddot{u}_1(t) + k_1u_1(t) + \kappa(u_1(t) - u_2(t)) &= 0 \\ m_2\ddot{u}_2(t) + k_2u_2(t) + \kappa(u_2(t) - u_1(t)) &= 0, \end{aligned} \tag{1.2}$$

with u_1 (u_2) being the deflections of resonator 1 (2) and κ expressing a complex coupling spring constant. Here, we assume two undamped resonators.
The height and width of resonator 1 and 2 are approximately the same, and thus the effective masses of the in- and out-of-plane modes are assumed to be identical. Because of the high

tensile stress in the resonators, we can express the effective masses of resonator 1 and 2 in terms of the physical mass of the string resonator $m_1 = m_2 = m = 0.5\rho V$. By employing the common ansatz $u_i = u_i^0 \exp(-i\omega t)$ (with $i = 1, 2$) we can derive the angular eigenfrequencies $\omega_\pm$ of the coupled system[46]

$$\omega_\pm^2 = \frac{1}{2}\left[\omega_1^2 + \omega_2^2 \pm \sqrt{\left(\omega_1^2 - \omega_2^2\right)^2 + 4g^2\omega_1\omega_2}\right] \tag{1.3}$$

and relate the complex coupling constant κ to the so called coupling strength[46] g

$$g = \frac{\kappa}{\sqrt{\omega_1\omega_2 m_1 m_2}}, \tag{1.4}$$

where $\omega_i = \sqrt{(k_i + \kappa)/(m_i)}$ (with $i = 1, 2$) are the coupling dependent eigenfrequencies of resonators 1 and 2.
Supposing that the coupling κ is nonzero, there will be a frequency splitting (*avoided crossing*) between the modes. At the avoided crossing, we can assume $\omega_1^2 - \omega_2^2 \approx 0$. If the coupling strength g is much smaller than the eigenfrequencies of the system, $\omega_\pm$ can be expanded to

$$\omega_\pm = \omega_m\sqrt{1 \pm \frac{g}{\omega_m}} \tag{1.5}$$

$$\approx \omega_m(1 \pm \frac{1}{2}\frac{g}{\omega_m}) = \omega_m \pm \frac{g}{2}, \tag{1.6}$$

where $\omega_m = \sqrt{\omega_1\omega_2}$ is the mean frequency. The frequency splitting between the modes can then be written as

$$\omega_+ - \omega_- = (\omega_m + \frac{g}{2}) - (\omega_m - \frac{g}{2}) = g. \tag{1.7}$$

Hence, the width of the frequency splitting is given by g.
If we assume $k_1 = k_0$ and $k_2 = k_0 + \Delta k$, the effect of an actual mode coupling becomes more figurative: in the absence of coupling ($\kappa = 0$) the eigenfrequencies cross (see Fig. 1.2a), whereas an avoided crossing occurs for a nonzero coupling $\kappa = 0.1k_0$ (see Fig. 1.2b).

We supposed so far, that the two harmonic oscillators were undamped. Under real conditions this is indeed not valid, since we must take into account several intrinsic and extrinsic damping mechanisms[47,48] acting on the silicon nitride resonators. This gives us additional damping terms $\Gamma_1\dot{u}_1$ and $\Gamma_2\dot{u}_2$ -with Γ_1 and Γ_2 being the damping rates of the two modes- in Eq. (1.2), leading to an additional imaginary part of the eigenfrequency solution in Eq. (1.3). The damping rates Γ_1 and Γ_2 are given by the full width at half maximum $\Delta\omega_i = \Gamma_i$ of the modes. Thereby, they correspond to finite linewidths of the resonances and determine the condition under which strong mode coupling can be observed:

$$\frac{g}{\Gamma_1 + \Gamma_2} > 1. \tag{1.8}$$

In other words, if the linewidths of the two coupled modes are smaller than the frequency splitting g, we can observe an avoided crossing, which we will take as evidence for strong mode coupling.

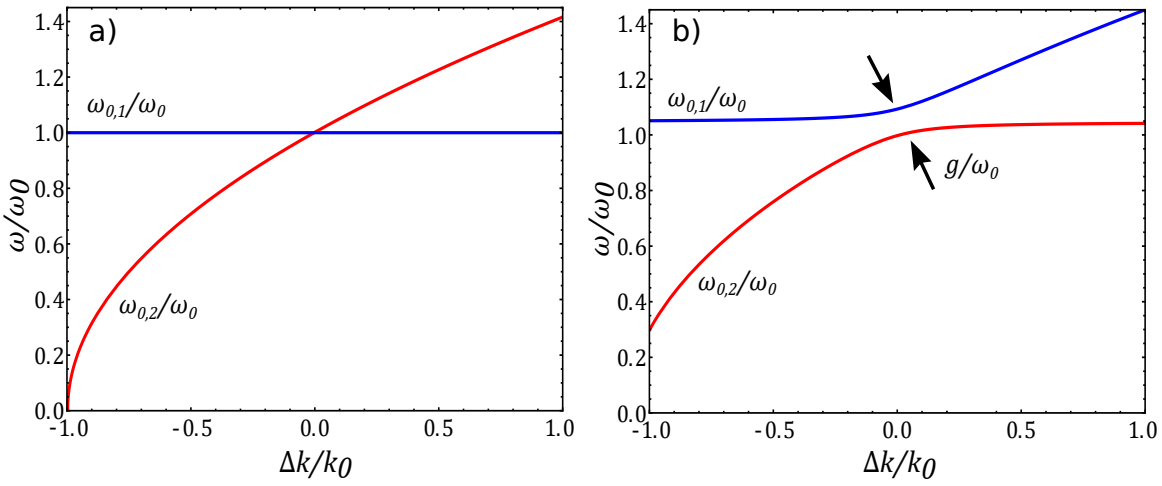

Figure 1.2: Eigenfrequencies of two harmonic oscillators depending on the relative spring constant $k_0 + \Delta k$ for (a) uncoupled resonators ($\kappa = 0$) and for (b) a finite coupling ($\kappa = 0.1k_0$). When $\kappa \neq 0$ (b) the frequencies show a characteristic splitting (*avoided crossing*) of width g.

1.2 Four coupled harmonic oscillators

In the scope of this work we investigate not only two modes of one single string resonator, but a system consisting of two nominally identical, parallel silicon nitride string resonators (see Fig. 1.3) with an in-plane and an out-of-plane fundamental flexural mode each. This yields a system of four coupled harmonic oscillators.

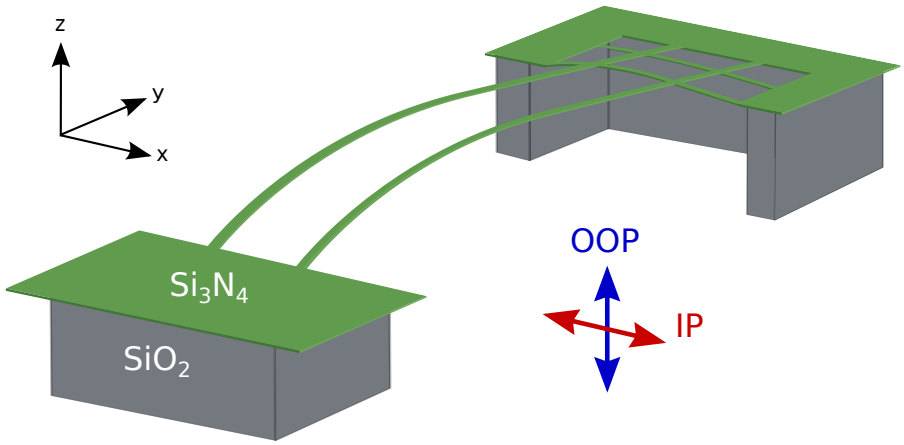

Figure 1.3: Sketch of a pair of parallel silicon nitride string resonators with shared clamping points with regular (lower left) and elaborated geometry (upper right). Both resonators are elongated in the out-of-plane direction. The red (blue) arrow indicates the in-plane (IP) (out-of-plane (OOP)) fundamental flexural modes.

Assuming that each mode i is coupled to every other mode j ($i, j = 1, 2, 3, 4$, where $i \neq j$ and

$ij = ji$), we can extend the above model (Eq. (1.2)) and write the equations of motion as

$$m_i\ddot{u}_i + k_i u_i + \sum_{i \neq j} \kappa_{ij} \left(u_i - u_j\right) = 0. \tag{1.9}$$

In analogy to the case of two coupled modes (see Eq. (1.4)), the complex coupling constants $\kappa_{i,j}$ can be related to the coupling strengths g_{ij}

$$g_{ij} = \frac{\kappa_{ij}}{\sqrt{\omega_i \omega_j m_i m_j}}. \tag{1.10}$$

As the two string resonators are nominally identical, the assumption of identical masses from chapter 1.1 is still valid and we obtain the angular eigenfrequencies ω_i of the coupled system

$$\omega_i^2 = \omega_{i0}^2 + \sqrt{\omega_i} \left(\sum_{i \neq j} g_{ij} \sqrt{\omega_j} \right). \tag{1.11}$$

In this case the eigenfrequencies ω_i of the coupled system are expressed in terms of the modes' uncoupled angular frequencies $\omega_{i0} = \sqrt{k_i/m}$.
Similar to the case of two coupled harmonic oscillators, we can observe an avoided crossing, if at least one κ_{ij} is nonzero. Furthermore, multiple avoided crossings can occur when more than one κ_{ij} are nonzero, since we assume every mode to be coupled to every other. And just like for the two harmonic oscillators, we again have to take into account that the actual resonator modes are affected by some damping terms $\Gamma_i m_i u_i$, which results in an imaginary part of the eigenfrequency solution in Eg. (1.11). Therefore, the above condition under which an avoided crossing and likewise strong mode coupling can be observed is still valid.
In the following, we will discuss strong dielectric intra-string mode coupling between the modes of one silicon nitride string resonator and strong mechanical inter-string mode coupling between the modes of two adjacent strings.

1.2.1 Electrical mode coupling

One possibility to achieve strong mode coupling between the modes of a single silicon nitride string is by dielectrical means: as silicon nitride is dielectric, exposing a string to a static inhomogeneous electrical gradient field leads to induction of dipoles (with dipole moment $\vec{p} = \alpha \vec{E}$) in the resonator. These dipoles are coupled to the gradient of the electric field and therefore this field-gradient exerts a force on the silicon nitride string[41,49]

$$\vec{F}_{el} = -\nabla(\vec{p}\vec{E}), \tag{1.12}$$

with α being the polarizability of the silicon nitride string resonator. If we now identify the flexural out-of-plane and in-plane modes of the string resonator with the z and x axes of the electrical field, we can write the force acting on the modes as

$$\begin{aligned} F_{el,x} &= -\frac{\partial(\alpha E^2)}{\partial x} \\ F_{el,z} &= -\frac{\partial(\alpha E^2)}{\partial z}. \end{aligned} \tag{1.13}$$

Here, we assigned the out-of-plane deflection from Eq. (1.2) with $u_1 = z$ and the in-plane deflection with $u_2 = x$. Additionally, the equations of motion for the two modes in the electric field can be written in analogy to Eq. (1.2), except that now there is an effective force acting on the modes:

$$\begin{aligned} F_x &= k_x x + \kappa_c(x - z) \\ F_z &= k_z z + \kappa_c(z - x). \end{aligned} \tag{1.14}$$

We therefore can relate the force of the electrical gradient field to the equations of motion of the two modes

$$\begin{aligned} F_{el,x} &= -\frac{\partial(\alpha E^2)}{\partial x} = k_x x + \kappa_c(x - z) \\ F_{el,z} &= -\frac{\partial(\alpha E^2)}{\partial z} = k_z z + \kappa_c(z - x). \end{aligned} \tag{1.15}$$

The cross derivative of the electrical field energy yields the nonlinear coupling constant[50,51] κ_c

$$\kappa_c = -\alpha \frac{\partial^2 E^2}{\partial x \partial z}, \tag{1.16}$$

implementing the intra-string coupling between the in-plane and out-of-plane mode within one single silicon nitride string resonator.
However, since the aim is to achieve strong inter-string coupling between the in- and out-of-plane modes of two adjacent string resonators, another coupling mechanism is needed.

1.2.2 Strain coupling

In addition to dielectric intra-string mode coupling, our system allows for strain-mediated mechanical inter-string mode coupling.
When a doubly clamped string resonators is elongated (either in the in-plane, or in the out-of-plane direction, see Fig. 1.3), vibrational energy dissipates through the clamping region.[52,53] This is caused by the geometry of the resonator and clamping and can be described by a finite mechanical impedance mismatch between the resonator and corresponding clamping point. This finite impedance mismatch determines the quantity of vibrational energy dissipated through the clamping: the higher the impedance mismatch, the less energy will be dissipated through the clamping.[54,55] The energy dissipation can be described in terms of an evanescent strain field spreading into the clamping region.[54,56] Strain-mediated mechanical coupling of two string resonators can be achieved by exploiting these evanescent strain fields. Figure 1.4 displays a finite element simulation of the squared normalized amplitude ϵ^2 of the vibrational strain field at the clamping point for the in-plane and out-of-plane fundamental flexural modes of two adjacent silicon nitride string resonators sharing one clamping point.
By engineering the clamping region, it is possible to increase the lateral expansion of each strain field and establish an overlap of these strain fields in order to enable the exchange of vibrational energy between the resonators, and hence strain-mediated mechanical inter-string coupling.

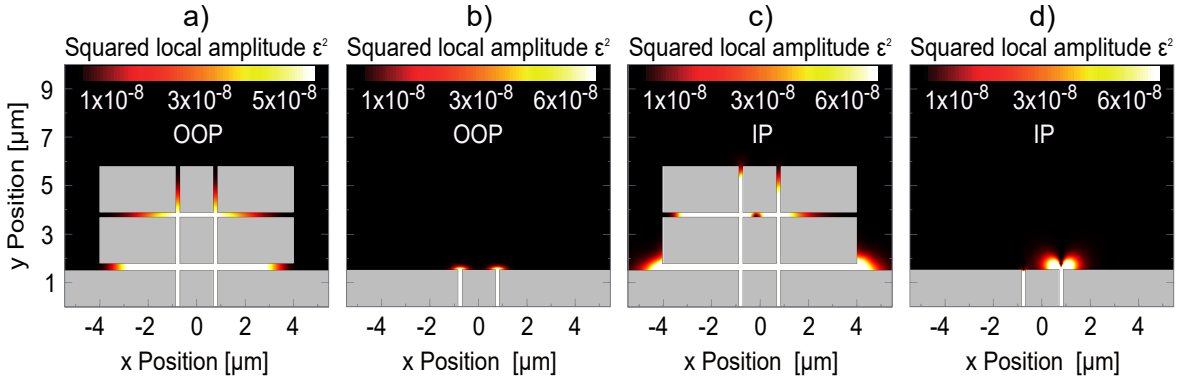

Figure 1.4: Finite element simulation of the squared normalized amplitude ϵ^2 (color scale) of the strain field in the clamping region for OOP and IP fundamental flexural modes. The coupling window layout (a and c) shows an enhanced strain field expansion into the clamping region compared to the layout without the window structure (b and d). Authorized reprint from Ref. [57].

The implementation of the so-called *window structure* (Fig. 1.4 a and c) strongly enhances the strain field expansion compared to the clamping region without the window (Fig. 1.4 b and d). That is at least one order of magnitude for the in-plane and two orders of magnitude for the out-of-plane mode. The size and dimensions of the window structure have non-trivial influence on the enhancement of the squared normalized amplitude ϵ^2, and thus on the coupling strength of the modes, which will be examined in chapter 2. The shared clamping point has dimensions of 16 µm $\times$ 16 µm with the window being 4 µm $\times$ 8 µm wide and high.

1.3 Duffing resonator

So far, the motion (in-plane and out-of-plane) of the string resonators was assumed to be linear and thereby each mode could be described by the linear harmonic oscillator. However, if the deflection u_i of the resonator becomes large, the resonator experiences a non-negligible stretching perpendicular to the direction of deflection (either in-plane or out-pf-plane direction, see Fig. 1.3), and hence the assumption of the linear harmonic oscillator does not hold anymore. This can be described as a geometric nonlinearity of the in-plane and out-of-plane modes of the string resonator. Therefore a first order correction to the equation of motion can be made by considering a nonlinear tensile stress[26] in the Euler-Bernoulli beam theory, and thus obtaining the Duffing equation

$$\ddot{u}_i + \Gamma_i \dot{u}_i + \omega_{i0}^2 u_i + \omega_{i0}^2 \gamma_{ii} u_i^3 = F_i. \tag{1.17}$$

Here the damping Γ_i was included, as well as some driving force F_i. The cubic correction term $\omega_{i0}^2 \gamma_{ii} u_i^3$ arises from the nonlinear tensile stress and corresponds to either a stiffening[44,45] of the mode (if $\gamma_{ii} > 0$), or a softening (if $\gamma_{ii} < 0$). Figure 1.5 illustrates the amplitude of a stiffening Duffing resonator as a function of the frequency detuning $\delta\omega_{i0}$.

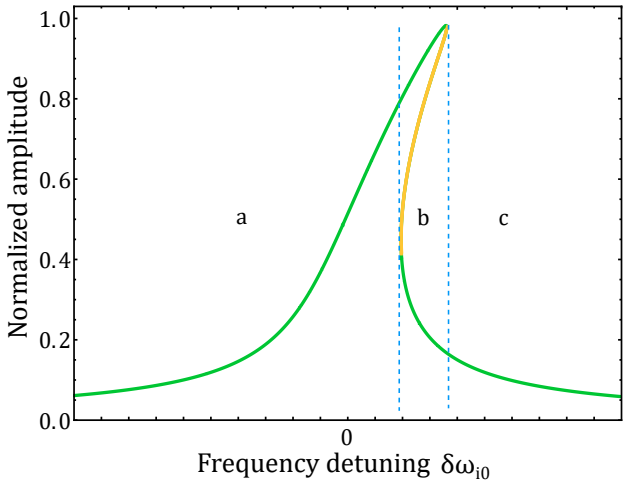

Figure 1.5: Normalized amplitude response of a stiffening ($\gamma_{ii} > 0$) Duffing resonator with the two stable areas a and c and the bi-stable region b. The yellow part in region b is instable.

The equation of motion of the Duffing resonator yields up to three possible solutions for the amplitude of the resonator, and hence offers areas of instability or bi-stability: one of the three solutions (marked with yellow color in region b (Fig. 1.5)) is instable and is not accessible in experimental measurements. Therefore region b is referred to as the bi-stable region. Depending in which direction the frequency is changed, the system response chooses the respective high amplitude (if the frequency is swept from left to right in Fig. 1.5) or low amplitude solution (if the frequency is swept from right to left in Fig. 1.5). The two blue dashed lines in Fig. 1.5 indicate the transition from the stable regions a and c to the bi-stable region b.
In a system of coupled resonators, the transition of one mode from the linear to the nonlinear regime can affect the respective coupled modes for example in terms of a frequency change.

1.4 Nonlinear coupled resonators

The following theoretical model was developed in cooperation with Dr. Gianluca Rastelli and is printed under his permission.

In the previous sections we described the classical linear harmonic oscillator, including linear coupled systems. As the underlying system consists of two string resonators with high Q factors, it also offers interesting physics in the nonlinear regime, for example, if the modes enter the nonlinear Duffing regime.
Assuming a system of damped coupled harmonic oscillators, the equation of motion (1.9) is written as

$$m\ddot{u}_i + m\Gamma_i\dot{u}_i + k_i u_i + \sum_{i\neq j} \kappa_{ij}\left(u_i - u_j\right) = 0, \tag{1.18}$$

with i and j being the respective mode index ($i, j = 1, 2, 3, 4$ and $ij = ji$, where $i \neq j$)). The equation of motion is sorted by u_i and u_j and is re-written as

$$m\ddot{u}_i + m\Gamma_i\dot{u}_i + u_i\left(k_i + \sum_{i\neq j}\kappa_{ij}\right) - \sum_{i\neq j}\kappa_{ij}u_j = 0. \tag{1.19}$$

For now, we considered u_i to be the deflection of the modes in units of meters. However, we can replace the deflection u_i by the amplitude v_i, which is in units of volts. A geometrical conversion factor η gives the relation between u_i and v_i as

$$v_i = \eta \cdot u_i. \tag{1.20}$$

If now the mass is considered to be $m = 1$ and an effective frequency $\bar{\omega}_{i0} = \sqrt{(k_i + \sum_{i\neq j}\kappa_{ij})}$ is introduced and $\Lambda_{ij} = \sqrt{\kappa_{ij}}$ is set, the coupled equations of motion can be written in the following from

$$\begin{pmatrix}\ddot{v}_1\\ \ddot{v}_2\\ \ddot{v}_3\\ \ddot{v}_4\end{pmatrix} = -\underbrace{\begin{bmatrix}\bar{\omega}_{10}^2 & -\Lambda_{12}^2 & -\Lambda_{13}^2 & -\Lambda_{14}^2\\ -\Lambda_{12}^2 & \bar{\omega}_{20}^2 & -\Lambda_{23}^2 & -\Lambda_{24}^2\\ -\Lambda_{13}^2 & -\Lambda_{23}^2 & \bar{\omega}_{30}^2 & -\Lambda_{34}^2\\ -\Lambda_{14}^2 & -\Lambda_{24}^2 & -\Lambda_{34}^2 & \bar{\omega}_{40}^2\end{bmatrix}}_{\Theta}\begin{pmatrix}v_1\\ v_2\\ v_3\\ v_4\end{pmatrix} - \underbrace{\begin{bmatrix}\Gamma_1 & 0 & 0 & 0\\ 0 & \Gamma_2 & 0 & 0\\ 0 & 0 & \Gamma_3 & 0\\ 0 & 0 & 0 & \Gamma_4\end{bmatrix}}_{\overline{\overline{\Gamma}}}\begin{pmatrix}\dot{v}_1\\ \dot{v}_2\\ \dot{v}_3\\ \dot{v}_4\end{pmatrix}, \tag{1.21}$$

with $\Lambda_{ij} = \Lambda_{ji}$. The eigenvalues Ω_i of Θ and the respective eigenvectors $\hat{e}_i$ can be written as

$$\Theta\hat{e}_i = \Omega_i^2\hat{e}_i, \tag{1.22}$$

with $\hat{e}_i\hat{e}_j = \delta_{ij}$ and $\hat{e}_i \times \hat{e}_i = \mathbb{1}$. The eigenvectors carry the information about the modes' polarization and hybridization and the eigenvalues give the frequency evolution of the coupled modes.
If the mode i is driven with a frequency ω_d, a driving force $F_i\cos(\omega_d t)$ has to be added to the equation of motion, yielding

$$\ddot{\vec{v}}_i = -\Theta\vec{v}_i - \overline{\overline{\Gamma}}\dot{\vec{v}}_i + \vec{F}_i\cos(\omega_d t). \tag{1.23}$$

In the case discussed here, only three modes participate in the nonlinear dispersive coupling and therefore the model is restricted to $i, j = 1, 2, 3$ for further considerations.
We can write a general nonlinear potential of fourth order for the system of three coupled harmonic oscillators:

$$\begin{aligned}\mathcal{V}_4 =& \frac{1}{4}\gamma_{11}v_1^4 + \frac{1}{4}\gamma_{22}v_2^4 + \frac{1}{4}\gamma_{33}v_3^4\\ &+\psi_{12}v_1^3v_2 + \psi_{13}v_1^3v_3 + \psi_{21}v_1v_2^3 + \psi_{31}v_1v_3^3 + \psi_{23}v_2^3v_3 + \psi_{23}v_2v_3^3\\ &+\frac{1}{2}\gamma_{12}v_1^2v_2^2 + \frac{1}{2}\gamma_{13}v_1^2v_3^2 + \frac{1}{2}\gamma_{23}v_2^2v_3^2\\ &+\phi_1v_1^2v_2v_3 + \phi_2v_1v_2^2v_3 + \phi_3v_1v_2v_3^2.\end{aligned} \tag{1.24}$$

Here γ_{ii} is the Duffing nonlinearity of the respective uncoupled mode and γ_{ij} is the nonlinear coupling coefficient between the modes. The terms with ψ_{ij} describe internal resonances, that is the frequency of one mode being commensurate with the frequency of a higher-order mode. All terms with ϕ_i belong to three-body interactions.
It is sufficient to focus on the nonlinear potential of fourth order, as the third order nonlinear potential contains only odd terms, that cause a symmetry breaking whose strength is expected to be small. Also the linear mode interaction (the linear mechanical and dielectric coupling) from Eq. (1.9) is assumed to be negligible for now.
The system is assumed to be driven on resonance with one particular mode i ($\omega_d \approx \bar{\omega}_{i0}$). We assume that no internal resonances are addressed by the system, and thus the third-order nonlinearities (all terms with ψ_{ij}) are negligible. Additionally, three-body interaction terms (all terms with ϕ_i) are not considered for now. With these assumptions a minimal nonlinear potential of fourth order can be written for the system as follows

$$\mathcal{V}_4 = \frac{1}{4}\gamma_{11}v_1^4 + \frac{1}{4}\gamma_{22}v_2^4 + \frac{1}{4}\gamma_{33}v_3^4 + \frac{1}{2}\gamma_{12}v_1^2v_2^2 + \frac{1}{2}\gamma_{13}v_1^2v_3^2 + \frac{1}{2}\gamma_{23}v_2^2v_3^2. \tag{1.25}$$

We now increase the linear interactions between the originally uncoupled modes. The amplitude v_i of the modes can be transformed by the eigenvectors e_i such that the new amplitude q_i reads as

$$v_i = \sum_{j=1}^{3} e_{ij}q_j. \tag{1.26}$$

Plugging this new amplitude q_i into the expression of the nonlinear potential $\mathcal{V}_4$ (Eq. (1.25)) and sorting the terms by q_i^4 and $q_i^2q_j^2$, it is possible to get the eigenvector- and hence polarization dependent expressions for the Duffing nonlinearities $\tilde{\gamma}_{ii}$ of the modes

$$\tilde{\gamma}_{ii} = \sum_j e_{ji}^4\gamma_{jj} + \sum_{jk} e_{ji}^2e_{ki}^2\gamma_{jk}, \tag{1.27}$$

with $j \neq k$ and the mode polarization dependent nonlinear dispersive coupling coefficients $\tilde{\gamma}_{ij}$

$$\tilde{\gamma}_{ij} = \sum_k 6\gamma_{kk}e_{ki}^2e_{kj}^2 + \sum_{km} \gamma_{km}(e_{ki}^2e_{mj}^2 + e_{kj}^2e_{mi}^2 + 4e_{ki}e_{mj},e_{kj}e_{mi}) \tag{1.28}$$

where $i, j, k, m = 1, 2, 3, k \neq m$ and $i \neq j$. In both expressions, $\tilde{\gamma}_{ii}$ and $\tilde{\gamma}_{ij}$, odd terms were neglected, as they pertain internal resonances, which are not addressed by the system. From the results of Eq. (1.27) and Eq. (1.28) it can be seen, that the Duffing nonlinearity $\tilde{\gamma}_{ii}$, as well as the nonlinear dispersive coupling $\tilde{\gamma}_{ij}$ depend on the hybridization of the modes. In particular, starting from the case in which $\gamma_{ij} \approx 0$ for $i \neq j$, strong nonlinear interaction of the modes can be obtained, if two or three modes are hybridized, for instance $\bar{\gamma}_{ii} \approx 6(\gamma_{11}e_{11}^2e_{12}^2 + \gamma_{22}e_{21}^2e_{22}^2 + \gamma_{33}e_{31}^2e_{32}^2)$. In this way we find that we can achieve the dispersive coupling to be of the same order of magnitude as the Duffing nonlinearity of a single mode.

Chapter 2

Sizing the window structure

As described in section 1.2.2, engineering a window structure in the clamping region can enhance the extension of the strain field of a resonator mode in the clamping point. In order to maximize the expansion, and thus the overlap of the strain fields of the two string resonators, the size and geometry of the modified clamping have to be chosen carefully. Therefore, finite element simulations were made, showing the influence of the dimensions of individual parts of the window structure on the mechanical coupling strength between the two OOP modes of the system. The coupling strength was obtained by varying the frequency of one of the out-of-plane modes, leading to an OOP-OOP avoided crossing, if the modes are in resonance.

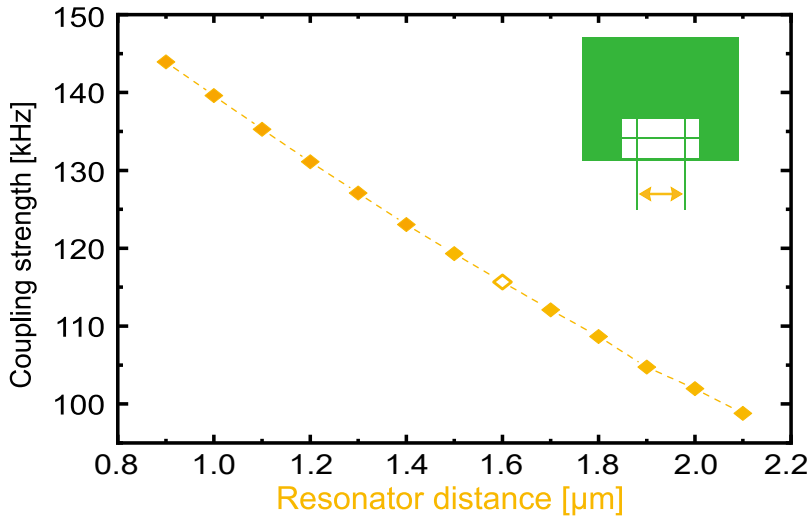

Figure 2.1: Finite element simulation of the OOP-OOP coupling strength depending on the resonator distance from 0.9 µm to 2.2 µm, which is measured from the right edge of the left resonator to the left edge of the right resonator as depicted by the orange arrow in the inset. The hollow marker (resonator distance of 1.6 µm) indicates the resonator distance chosen for the geometry under investigation. The window ledge width is 300 nm and the coupling beam width is 200 nm.

Figure 2.1 shows a decrease of the OOP-OOP coupling strength with increasing resonator distance. This is consistent with the decreasing overlap of the strain fields in the clamping region induced by resonators of increasing distance. The orange arrow in the inset indicates the distance of the right edge of the left resonator to the left edge of the right resonator. This distance was varied from 0.9 µm to 2.2 µm in steps of 0.1 µm. For the system investigated in this work, a resonator distance of 1.6 µm was chosen (hollow marker) to secure a good mechanical coupling at one hand, but also allowing for fabrication of an electrode of sufficient size between the resonators on the other hand. If the electrode is too small, or the gap between resonator and electrode is too narrow this will cause several difficulties during fabrication (see chapter 3.1). For a resonator distance of 1.6 µm a coupling strength of 115 kHz is predicted by the simulation. Besides the resonator distance, structural elements of the window such as the so called *window ledge* (see inset of Fig. 2.2) and *coupling beam* (see inset of Fig. 2.3) significantly influence the OOP-OOP coupling strength. A variation of the window ledge width from 100 nm to 600 nm

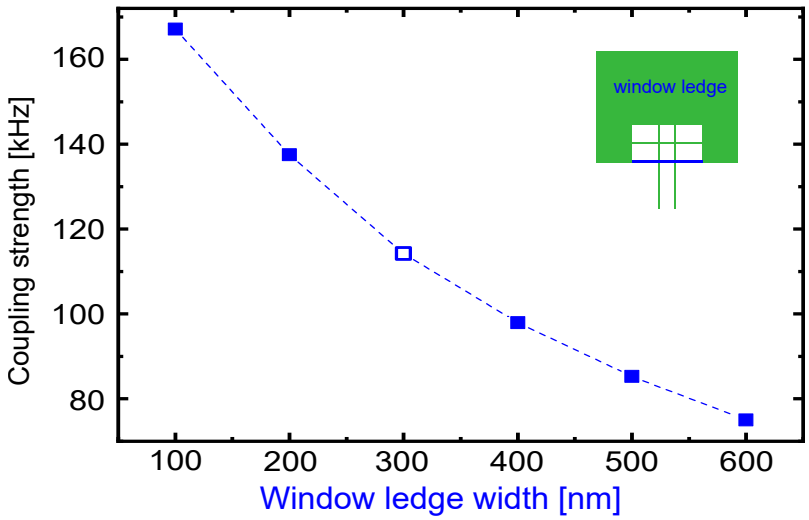

Figure 2.2: Finite element simulation of the OOP-OOP coupling strength depending on the window ledge width, which is varied from 100 to 600 nm. The hollow marker (at 300 nm) indicates the window ledge width chosen for the geometry under investigation and predicts a coupling strength of 115 kHz. The coupling beam width is 200 nm and the resonator distance is 1.6 µm. Adapted from Ref. [57].

leads to a pronounced drop of the OOP-OOP coupling strength from over 160 kHz to below 80 kHz, as shown by the finite element simulation in Fig. 2.2. According to the simulation, a window ledge width of 300 nm (hollow marker) corresponds to a coupling strength of 115 kHz. This window ledge width was chosen for the window geometry investigated in this work.
Also, the increase of the coupling beam width causes a decrease in coupling strength, as can be seen in Fig. 2.3. Here the coupling beam width was varied from 0 nm to 600 nm and it shows a decrease in coupling strength from 125 kHz to 100 kHz. The coupling beam width for the investigated structure was chosen to be 200 nm (hollow marker), corresponding to a calculated coupling strength of 115 kHz. If we choose a coupling beam width of 200 nm, a window ledge

width of 300 nm and a resonator distance of 1.6 µm, we expect the OOP-OOP coupling to be in the range of 115 kHz. The simulations were made for 180 nm wide, 100 nm thick and 55 µm long resonators, and hence match the dimensions of the system investigated in this work.

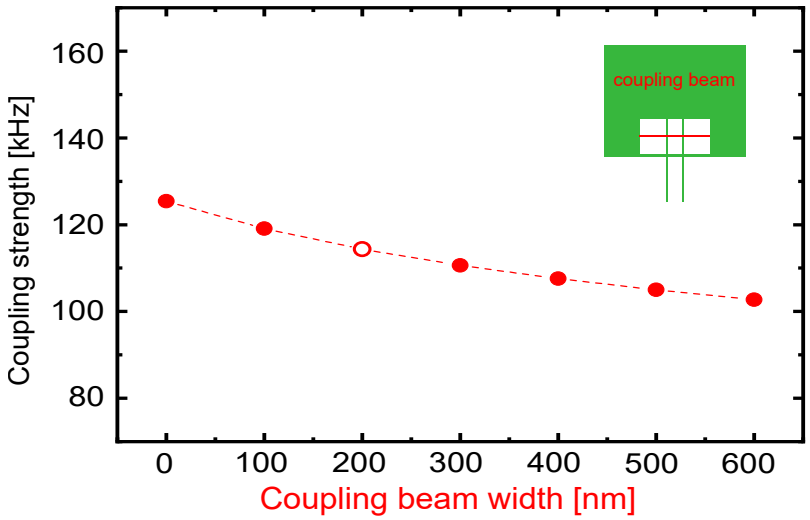

Figure 2.3: Finite element simulation of the coupling beam with depend OOP-OOP coupling strength for coupling beam widths varied from 0 to 600 nm. The hollow marker (at 200 nm) predicts a coupling strength of 115 kHz, and corresponds to the coupling beam width chosen for the geometry under investigation. The window ledge width is 300 nm and the resonator distance is 1.6 µm. Adapted from Ref. [57].

The coupling beam- and window ledge widths were only varied to a maximum value of 600 nm, because structures wider than this will no longer be freely suspended on account of our last fabrication step. This last step is an HF wet etch leading to an *undercut* of the structures of about 300 nm (for more details see chapter 3.1). If the coupling beam and/or the window ledge are wider than this undercut, they will not be freely suspended, what will in turn decrease the coupling strength to near zero, and thus make the implementation of the window structure obsolete.

2.1 Eigenfrequency study

Besides the OOP-OOP coupling strength, the size of the window structure also affects the resonance frequencies of the modes, as shown in Fig. 2.4. This could be a consequence of the enhancement of the effective resonator length as a result of the implementation of the window structure into the clamping region. Additionally, the strain decreases with increasing resonator length, what also causes a shift of the eigenfrequencies of the modes.
The width of the coupling beam directly affects the eigenfrequencies of the modes. Finite element simulations show an increase in frequency of the out-of-plane mode of about 17 kHz for a coupling beam width of 800 nm compared to a 200 nm wide coupling beam. For the in-plane mode we expect an increase of only 150 Hz in frequency. As we have a statistical

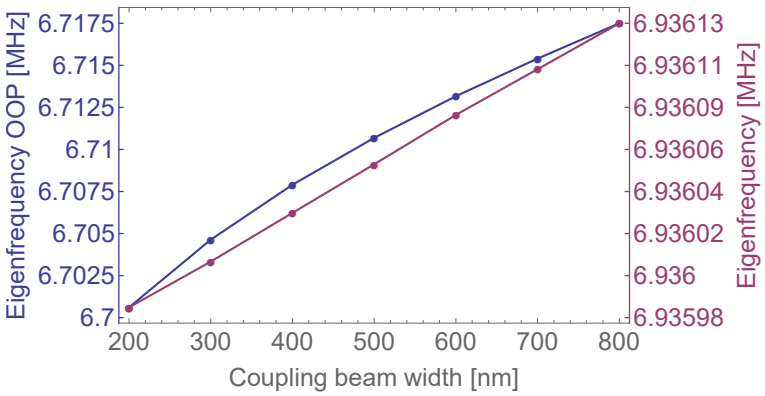

Figure 2.4: Finite element simulation of the eigenfrequency dependence of IP an OOP mode on the coupling beam width. The coupling beam width was varied from 200 to 800 nm, showing an increase in frequency of 17 kHz for the OOP mode and 150 Hz for the IP mode.

frequency deviation of 1% - 2% for fabricational reasons, we cannot confirm these findings quantitatively with our experiments. Nontheless, we find a qualitative tendency of the eigenfrequency to increase with increasing coupling beam width, as can be seen from the data in Fig. 2.5. The experimental data shows an increase in frequency of about 100 kHz for a coupling beam of 800 nm width compared to a width of 200 nm. Calculating the frequency as a function of the coupling beam width for 400 nm wide and 35 µm long resonators, a theoretical rise in frequency of about 64 kHz is expected as shown in the inset of Fig. 2.5.

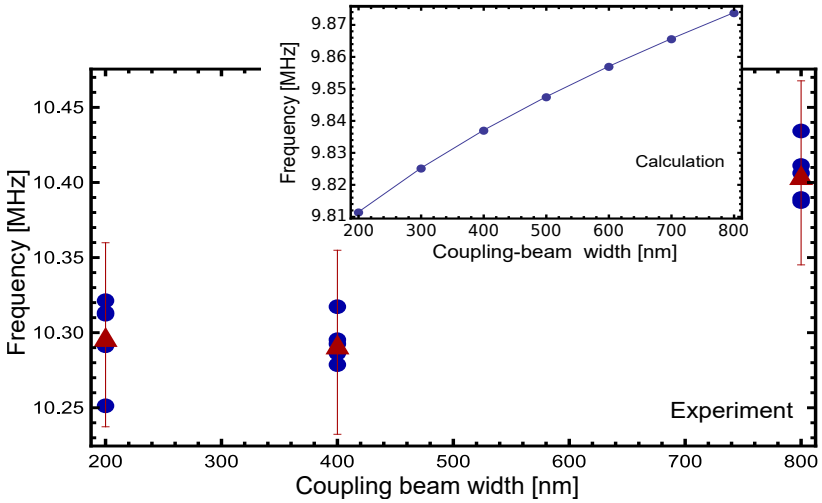

Figure 2.5: Measured OOP eigenfrequency dependence on the coupling beam width (blue dots) for 400 nm wide and 35 µm long resonators with mean frequency and statistical frequency deviation (red triangles with error bars). The inset shows the calculated OOP eigenfrequencys dependence for the same resonator dimensions.

Figure 2.5 shows that we can see a tendency for higher coupling beam widths to cause an

increase of the eigenfrequency, but the mathematically predicted increase of the eigenfrequency (inset of Fig. 2.5) cannot be reproduced experimentally. In the scope of this work, some statistics were made on the mean frequency fluctuation of silicon nitride string resonators, showing that imperfections during fabrication lead to a statistical deviation of 1% - 2% of the eigenfrequency. For eigenfrequencies of about 10 MHz this corresponds to a frequency deviation of 100 kHz to 200 kHz (depicted by the red error bars in Fig. 2.5), which does not allow to resolve the much smaller theoretical frequency increase of 64 kHz caused by the coupling beam width. Furthermore, the effective frequency offset of 1% - 2% can be higher than the frequency tuning range provided by the applied DC-actuation technique (see chapter 3.2), and thus does not allow to bring several modes of the two-resonator system in resonance in order to observe strong mode coupling.

Chapter 3

Layouts, Actuation and Detection schemes

This chapter gives detailed information about the utilized sample design, including resonator- and multi-electrode geometries. Additionally, a brief overview of the sample fabrication is given. For a detailed step-by-step instruction on sample fabrication and process parameters, please see Appendix A. Furthermore, the applied actuation and detection techniques are explained. The sample layout allows for piezo-driven and dielectric actuation. A laser-interferometric- as well as microwave cavity enhanced frequency readout are available.

3.1 Introducing the sample layouts

The simulations in chapter 2 offer a variety of geometric possibilities to adjust the mechanical coupling strength. However, deciding on coupling strength and sample performance is a trade-off between dimensional requirements (as shown in chapter 2.1) and fabricational challenges.
We choose a window ledge of 300 nm, a coupling beam width of 200 nm, and a resonator distance of 1.6 µm (as illustrated in chapter 2). The resonators are nominally 180 nm wide and their length is varied from 55 µm to 50 µm. With these dimensions we expect an OOP-OOP coupling strength of 115 kHz.
The samples investigated in this work are fabricated in a top down approach (for detailed fabrication see appendix A) from a $(5 \times 5)\,\mathrm{mm}^2$ big and 500 µm thick silicon dioxide chip, with a strongly pre-stressed silicon nitride layer on top. On one chip, we fabricate four so called *write-fields*. Each of these write-fields consists of six resonator pairs. The fabrication includes two-step electron beam lithography, inductive coupled plasma reactive ion etching and an HF wet-etch to release the resonators. This step gives an initial *undercut* of the clamping points, electrodes and bond pads of 300 nm. Figure 3.1 shows a SEM picture of the shared clamping point with the window structure. The under-etched area on the rim of the clamping point appears brighter than the rest of the clamping point because of different contrast properties compared to the non-undercut area. For the gold electrodes we don't see this difference in contrast. The blue arrows indicate the undercut of the clamping and the electrodes.
The width of the resonators determines the minimum etching time needed to under-etch the res-

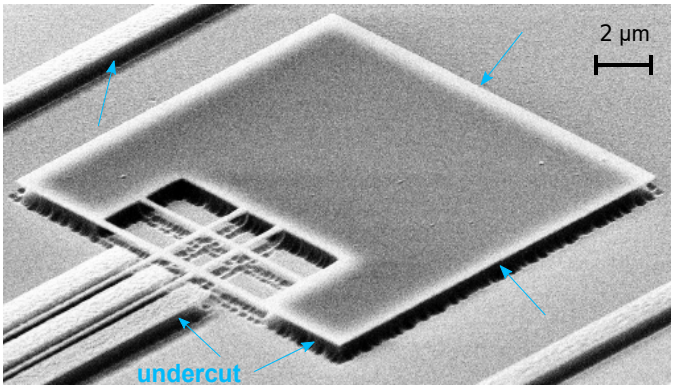

Figure 3.1: SEM picture of the shared clamping point, showing a clear undercut on the edge of the clamping point and the electrodes, as indicated by the blue arrows.

onator completely, whereas by altering the etching time we can adjust the depth of the undercut. We could increase this undercut, but for the price of increasing the resonator distance, and thus decreasing the coupling strength, because an increased undercut requires wider electrodes between the resonators in order to secure a pedestal underneath the electrodes.
Additionally, we are also limited by the gap between the resonator and the respective electrode. As mentioned above, the sample fabrication includes a two-step electron beam lithography. A structure alignment procedure has to be done during the lithography process. Even though electron beam lithography is precise, there still is an offset between the aligned structures which may be tens of nanometers. Therefore a resonator distance of 1.6 µm was chosen to secure a sufficient electrode width of 1 µm and a resonator-to-electrode distance of 300 nm.
Overall, the yield of suitable resonator pairs is significantly smaller than for single resonators, since not only two random resonators out of an array of resonators, but a functioning pair of resonators, have to be the result of the fabrication process. Besides this, the resonator pair has to meet several requirements in order to be considered for further experiments: the eigenfrequencies of the in- and out-of-plane modes have to be sufficiently close (frequency offset must be smaller than the dielectric tuning range) and the modes need to couple to the electrodes in order to be tuned in and out of resonance by the dielectric tuning mechanism. Therefore, a lot of fabrication is needed to gain a considerable amount of resonator pairs meeting these conditions.
Throughout this work several sample layouts were used, differing in the number and geometry of electrodes surrounding the resonators. In the following, three geometries will be introduced, which were designed and employed during this work.

3.1.1 2-Electrode geometry

The very first measurements on coupled silicon nitride string resonators presented in this work were made on the so called 2-electrode-geometry. As the name implies, this layout has only two electrodes, namely one on the left side of resonator 1 and one between the resonators, as depicted in Fig. 3.2.

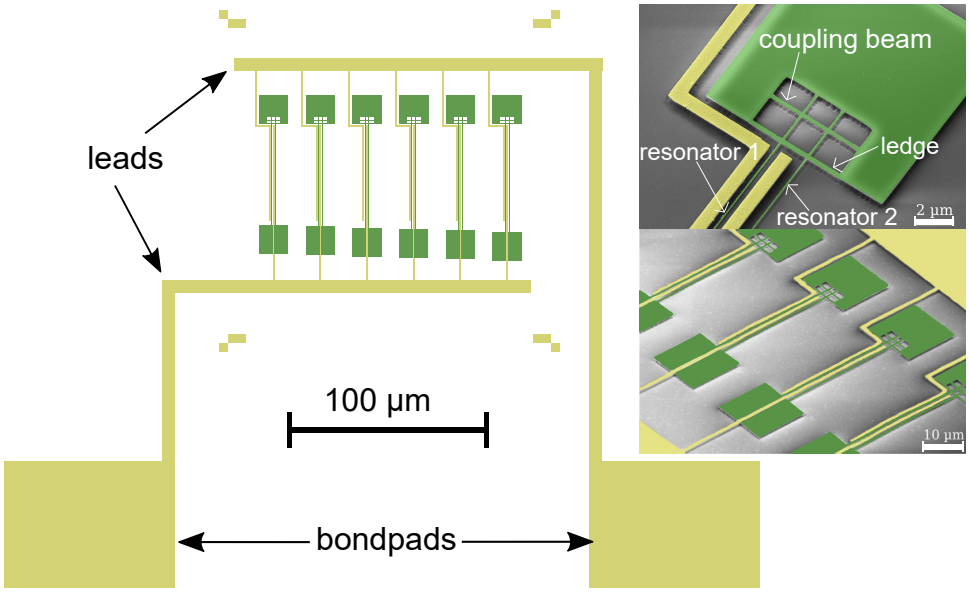

Figure 3.2: Left: sketch of the sample layout for the 2-electrode geometry with 6 pairs of resonators, leads and bondpads. Right: SEM false-color picture of the 2-electrode geometry including a zoom in of the shared clamping point of one resonator pair with window structure. Authorized reprint from Ref. [57].

This allows for addressing up to six resonator pairs by only connecting two *bondpads*. These pads are connected via wire bonding to the electrical components on the sample-holder. Since for this layout only one resonator (resonator 1) is surrounded by electrodes, only this resonator is electrically accessible (see sections 3.2 and 3.3); resonator 2 in contrast has no electrodes.

3.1.2 3-Electrode geometry

Going one step further in versatility, a third electrode was added to the system, so both resonators can be addressed separately. The implementation of the third electrode requires a rearrangement of leads and bondpads. More than two bondpads are needed in order to avoid crossings of the leads and therefore insulating layers and additional lithography steps.
However, if some resonators share their leads and bondpads, we can reduce the number of necessary bondpads to 8 instead of 12. With this, we achieve separate actuation of each resonator if the outer electrodes of a resonator pair are connected to the dielectric actuation (see chapter 3.2) and the middle electrode is grounded. Also the 3-electrode geometry enables separate detection

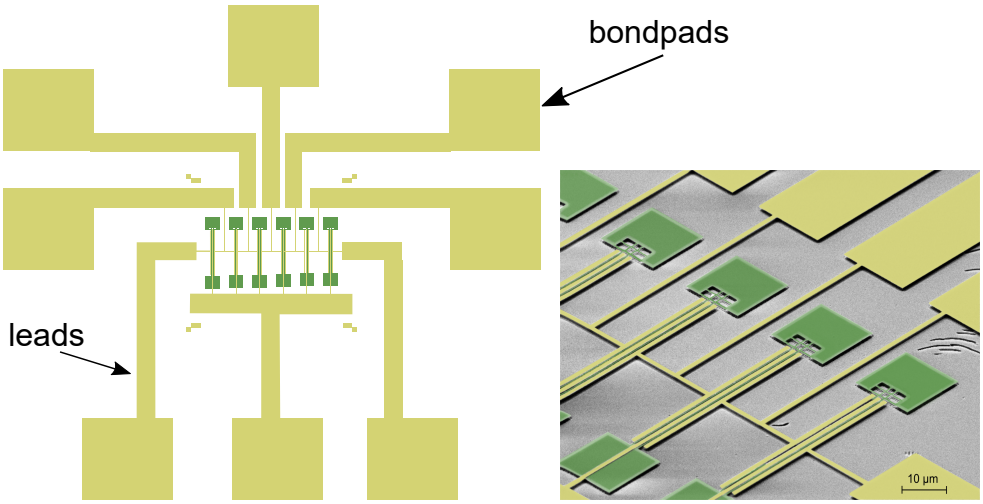

Figure 3.3: Left: 3-electrode layout with 6 pairs of resonators, leads and bondpads. Right: SEM false-color picture of the 3-electrode geometry.

of each resonator, if the middle electrode is connected to the dielectric actuation and the outer electrodes are connected to the microwave readout (see chapter 3.3).

3.1.3 5-Electrode geometry

A more advanced version of a layout allowing for simultaneous actuation and detection of both resonators separately is the 5-Electrode geometry. Here each resonator pair is surrounded by 5 electrodes (see Fig.3.4). This enables not only the separate actuation of each resonator, but we can simultaneously append a separate microwave cavity (see chapter 3.3).

In order to realize 5 electrodes per pair of resonators, the outer electrodes of each pair are split in a way that there are four outer electrodes and one electrode in between the resonators. This allows for individual actuation and readout of each resonator at once. The middle electrode is grounded to the sample holder. Furthermore, the window structure is alternated between the clamping points, so a crossing of the leads can be avoided. Additionally, the outer electrodes are shared by two neighboring resonator pairs, thus decreasing the number of bond pads to 20.

3.2 Actuation

In the scope of this work, two different actuation techniques were employed. The simplest way to excite the resonators is to glue the whole chip on a piezoelectric crystal and actuate it with a white noise signal in the frequency range of the eigenfrequencies of the resonators. This technique is used to get a quick overview of the eigenfrequencies of the modes. However, it

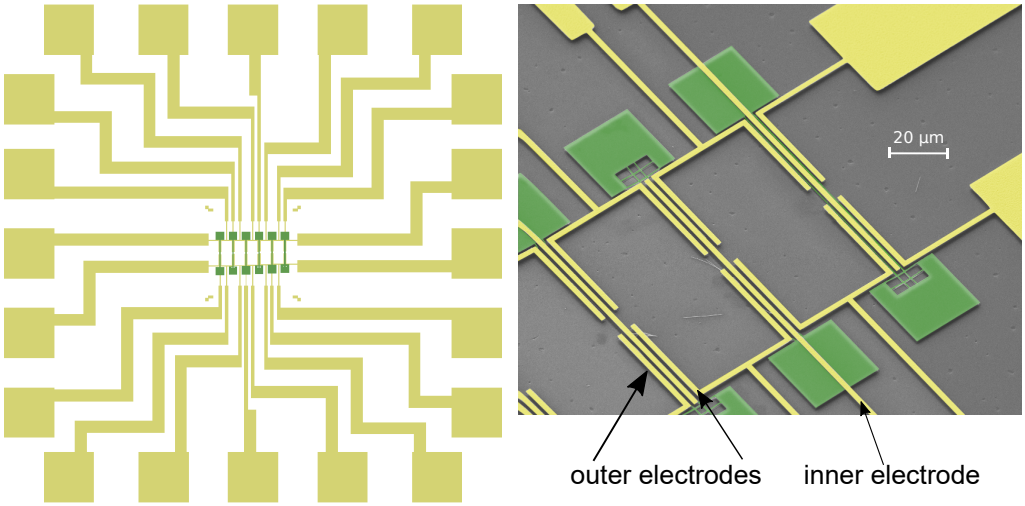

Figure 3.4: Left: 5-electrode layout with 6 pairs of resonators, with 5 electrodes each and 20 bond-pads in total. Right: SEM false-color picture of the 5-electrode layout, with window position alternation between clamping points.

does not allow for detuning of the eigenfrequencies, which is essential to investigations on their coupling behavior. Therefore, we employ a dielectric actuation[41] and tuning[58] technique.

3.2.1 Dielectric actuation and detuning

Immersing the silicon nitride string into an electrical gradient field induces a charge distribution in the silicon nitride which can be described by the dipole approximation.[41] This can be done by applying a constant voltage U_{dc} with an additional RF voltage component U_{rf} between two electrodes surrounding the resonator. As both, the electric field and the resulting dipole moment are proportional to $U_{tot} = U_{dc} + U_{rf}$ and the RF voltage is modulated rather weakly, the force acting on the resonator (see eq 1.12) can be written as

$$F[U_{dc} + U_{rf}] = C_1(U_{dc} + U_{rf})^2 \approx C_1 U_{dc}^2 + 2C_1 U_{dc} U_{rf}, \tag{3.1}$$

where C_1 is a constant. Hence the U_{rf} component actuates the resonator and U_{dc} can tune the eigenfrequency of the resonators' modes. The negative force gradient (to a variable coordinate $\zeta = x, z$) of the electrical field F_{el} determines an electrical spring constant[58] k_e

$$k_e = -\frac{\partial F_{el}}{\partial \zeta}, \tag{3.2}$$

which leads to a shift in the angular eigenfrequency ω_{i0} (see chapter 1.2) of the resonators' modes

$$\omega_{i0} = 2\pi\sqrt{\frac{k_0 + k_e}{m}} \approx \omega_{i0}^* + 2\pi c_i U_{dc}^2, \tag{3.3}$$

with the intrinsic angular eigenfrequency in absence of electrical tuning and mode coupling ω_{i0}^* and the quadratic tuning factor c_i. The eigenfrequencies show a quadratic U_{dc} dependence, as depicted in Fig. 3.5. The curvature of this tuning parabola is either positive (stiffening) for the OOP mode, or negative (softening) for the IP mode for the chosen electrode configuration.

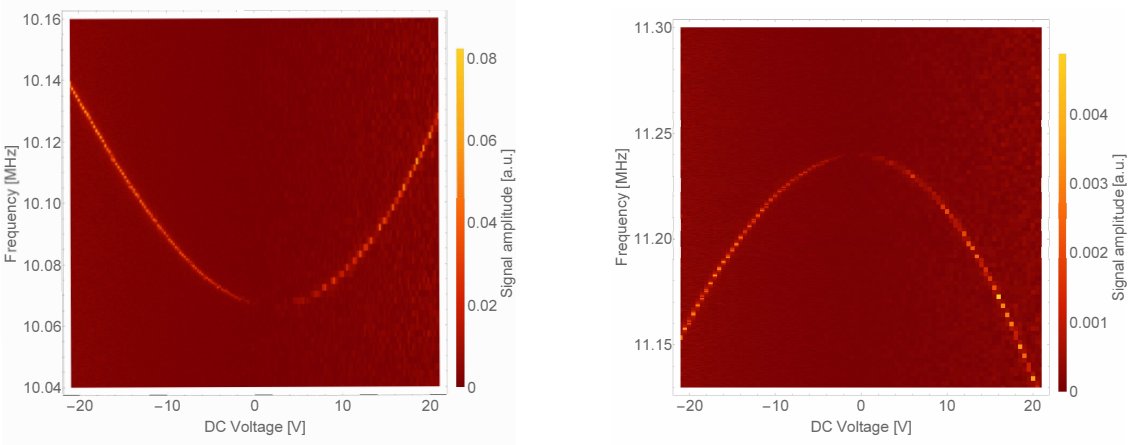

Figure 3.5: Left: Tuning parabola with positive curvature (stiffening) of an OOP mode for a U_{dc} range of -21 V to $+21$ V. Right: IP-mode tuning parabola with negative curvature (softening).

A static (pre-)polarization of the resonator may lead to a shift of the vertex of the tuning parabola by U_0. Taking this into account, and including a cubic correction d_i of the parabola, the angular eigenfrequency reads as

$$\omega_{i0} = \omega_{i0}^* + 2\pi(c_i(U_{dc} - U_{i0})^2 + d_i(U_{dc} - U_{i0})^3). \tag{3.4}$$

The index i (with $i = 1, 2, 3, 4$) refers to the respective mode number.

3.3 Detection

The experimental setup utilized in the scope of this work combines a Fabry-Perot interferometer with a microwave cavity enhanced readout[42,58] technique. Depending on the type of measurement performed, it is more convenient to employ one or the other technique. The interferometric option allows for a rather "simple" frequency detection and classification of the modes, whereas the readout via a microwave cavity enables integrated electrical detection of the modes. A detailed description of the interferometric setup, as well as the electronics used for the microwave cavity readout can be found in Appendix C.

3.3.1 Interferometric readout

A very convenient way to measure the resonances of silicon nitride string resonators is by laser-interferometric means (for a detailed picture and description of all components, please see

Appendix C.1). If the diameter of the laser spot is bigger than the width of the resonator pair a part of the laser beam will be reflected by the surface of the resonators and the other part is reflected by the substrate. The resulting interference is detected by a photo diode and the signal is fed to either a vector network analyzer, or a spectrum analyzer. The sample is glued to a piezo crystal positioned on a sample holder, which in turn is mounted on top of a piezoelectric positioner stack. This allows for precise positioning of the sample underneath the laser spot, so we can detect all four modes of the system at once. An additional camera enables the visual classification of the resonator pair under investigation and also simplifies the assignment of the modes. The interferometric readout provides a sensitivity[59] of $1.47\,\mathrm{pm}\sqrt{\mathrm{Hz}}^{-1}$, enabling the detection of the thermal motion of the resonators. For the laser utilized here, we have a wavelength of 640 nm and a power of 40 mW, leading to additional heating effects in the silicon nitride strings. This heating manifests itself in a frequency shift of the modes. Even if the laser power is attenuated to 10 mW we still see a frequency shift up to several kHz, if the laser is turned on and off.

3.3.2 Microwave cavity enhanced readout

Beyond the optical readout technique, we can access the resonators' modes dielectrically by coupling a $\lambda/4$ microstrip cavity to one of the electrodes surrounding the resonators[42] via wire bonding. A DC bias and RF drive are applied to one of the two gold electrodes alongside the resonator to actuate the resonator and detune its eigenfrequendy (right side of Fig. 3.6). Therefore, we have an oscillating dielectric between the two electrodes. In this sense, the electrodes flanking the resonator act as a capacitor, the capacitance of which is modulated by the oscillation of the dielectric silicon nitride resonator. The modulation of the capacitance of the gold electrodes in turn modulates the eigenfrequency of the microwave cavity. If the microwave cavity is pumped on resonance, this modulation causes two sidebands in the microwave signal. In an in-phase quadrature mixer (which is fed with the microwave pumpfrequency) the modulated transmission signal is demodulated.[42] The sideband signal is then sent to a low-pass filter and an amplifier, such that the mechanical frequency spectra of the silicon nitride strings can be displayed by either a vector network analyzer, or a spectrum analyzer. It is also possible to drive the microwave cavity slightly frequency-detuned, which leads to optomechanical heating, or cooling of the silicon nitride resonator modes.[42] In order to avoid these backaction effects, the microwave cavity has to be driven at exactly its eigenfrequency. Because the microwave cavities utilized here have Q factors between 60 to 80, the frequency response of the microwave cavity is broad, thus making it difficult to find the exact eigenfrequency. But, we can take advantage of the backaction effect: by varying the microwave pumpfrequency, we can measure the frequency shift of the mechanical resonator. The pumpfrequency corresponding to the maximum of the mechanical eigenfrequency is the exact eigenfrequency of the microwave cavity. For a better understanding of the working principle of the microwave cavity enhanced readout, a schematic of the components is shown in Fig. 3.6 for the 2-electrode layout (see chapter 3.2). For this geometry only one resonator is electrically accessible, and hence only one resonator can be coupled to a microwave cavity. As the schematic shows, the outer electrode is coupled to

the dielectric actuation components, while the middle electrode is connected to the microwave cavity. An additional single layer capacitor on the sample holder can be used as a bypass for the microwave cavity and simultaneously allows for the electrical accessibility of the gold electrodes for the RF drive and the DC bias.

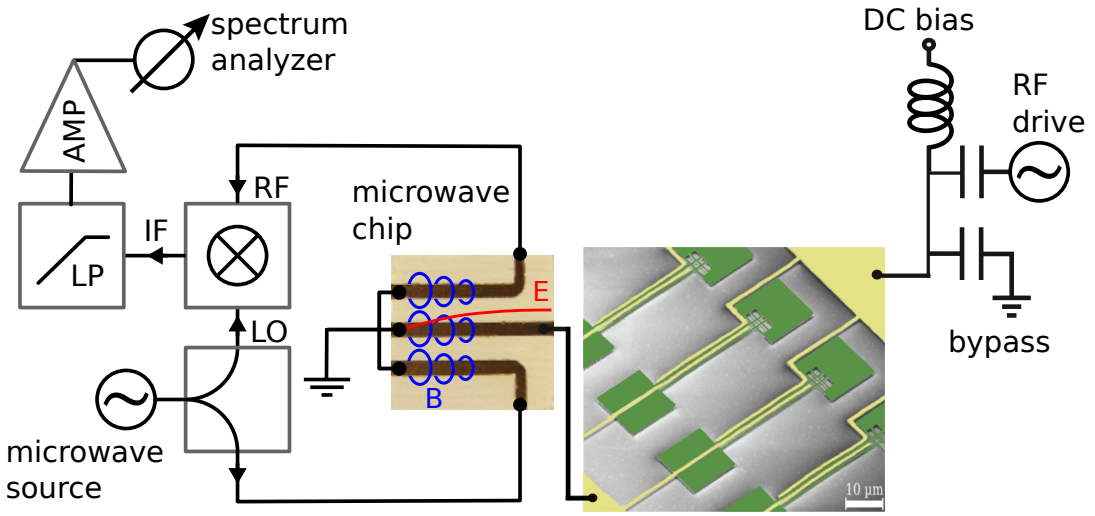

Figure 3.6: Schematic of the microwave cavity enhanced readout technique including a SEM false color picture of a 2-electrode geometry sample (see chapter 3.2) and the coupled $\lambda/4$ microwave cavity chip. The red line on the microwave chip shows the electric field line, the blue circles show the magnetic field lines, respectively. RF drive tone and DC bias are applied to one electrode, driving and tuning the resonator modes. The oscillation of the resonator modulates the capacitance between the gold electrodes, and thus the microwave cavity signal. This modulated signal (RF) is sent to the in-phase quadrature mixer along with a reference signal (LO). The demodulated signal (IF) is then filtered by a low-pass filter (LP) and amplified (AMP). Finally, this signal is displayed by a spectrum analyzer.

Depending on the employed sample geometry, the dielectric actuation and detection scheme has to be modified in order to meet the requirements of driving and detecting the modes of both silicon nitride resonators separately.
For the 3-electrode layout (see chapter 3.3) the above schematic has to be extended by either a second actuation part, or a second set of the microwave cavity readout components, depending on the purpose of the experiment. Figure 3.7 shows the case of separate resonator actuation with one microwave cavity coupled to the middle electrode of a resonator pair. The outer electrodes of the respective resonator pair are electrically connected to a source meter (DC bias) and a waveform generator (RF drive). This enables separate actuation and moreover frequency tuning of both resonators.

In Fig. 3.8 the extended actuation and readout version for the 5-electrode geometry is presented. Here the outer electrodes are split to secure the individual actuation and microwave cavity readout of each resonator. The middle electrode is grounded.

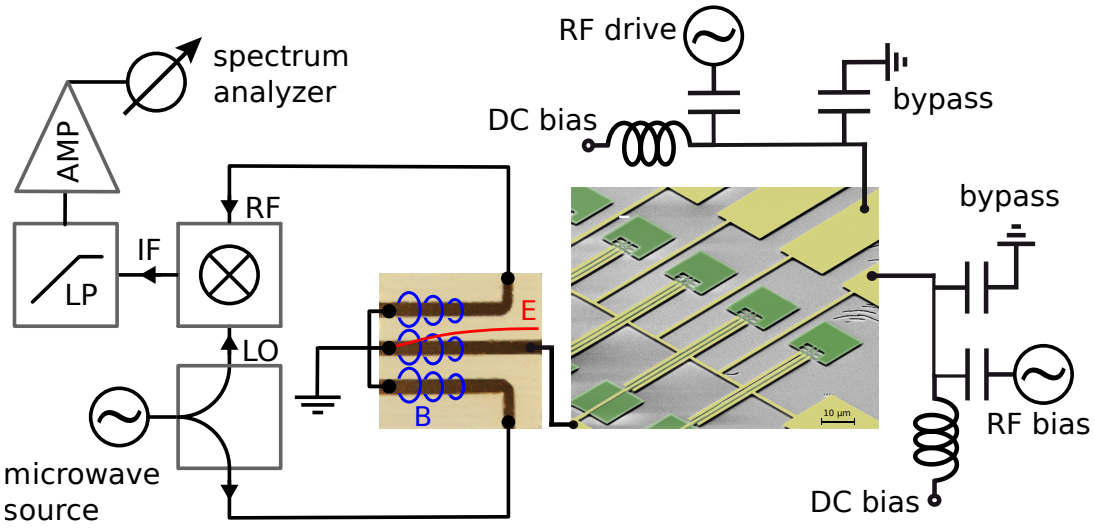

Figure 3.7: Schematic of the microwave cavity enhanced readout technique for the 3-electrode layout with separate actuation of the respective resonators. The microwave cavity is coupled to the middle electrode, and hence enables the readout of one resonator, respectively.

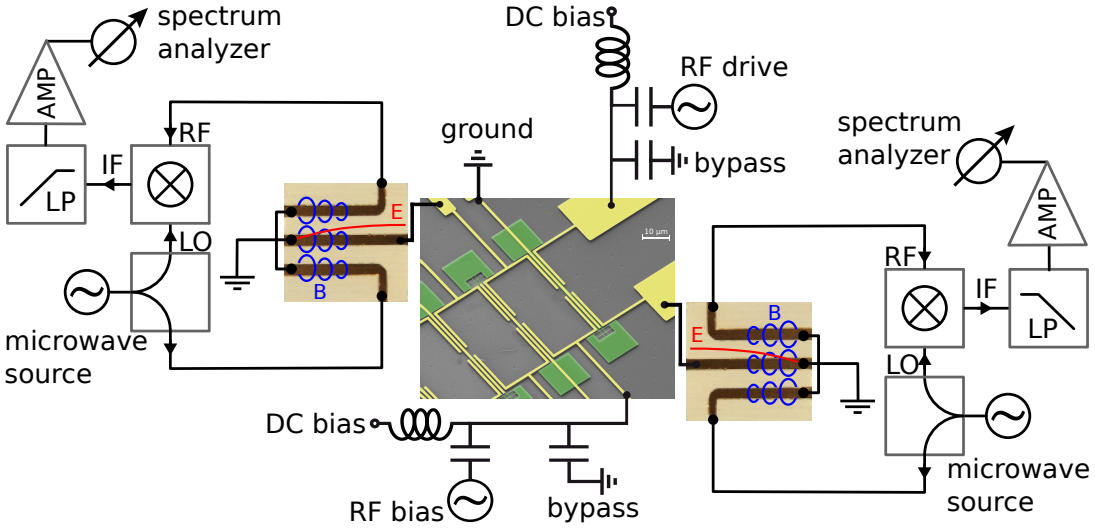

Figure 3.8: Schematic of the microwave cavity enhanced readout technique for the 5-electrode layout with separate actuation and detection of the respective resonators. The outer electrodes are split to make each resonator accessible to dielectric actuation and microwave cavity readout. The middle electrode is grounded.

The silicon nitride sample, along with the microwave cavity and dielectric circuit boards, are situated on a sample holder, which satisfies the requirements that arise by the respective sample layout. The sample holder shown in Fig. 3.9 offers the possibility to employ two microwave cavities, two separate electric circuit boards for dielectric access and a piezoelectric actuation

all within one device.

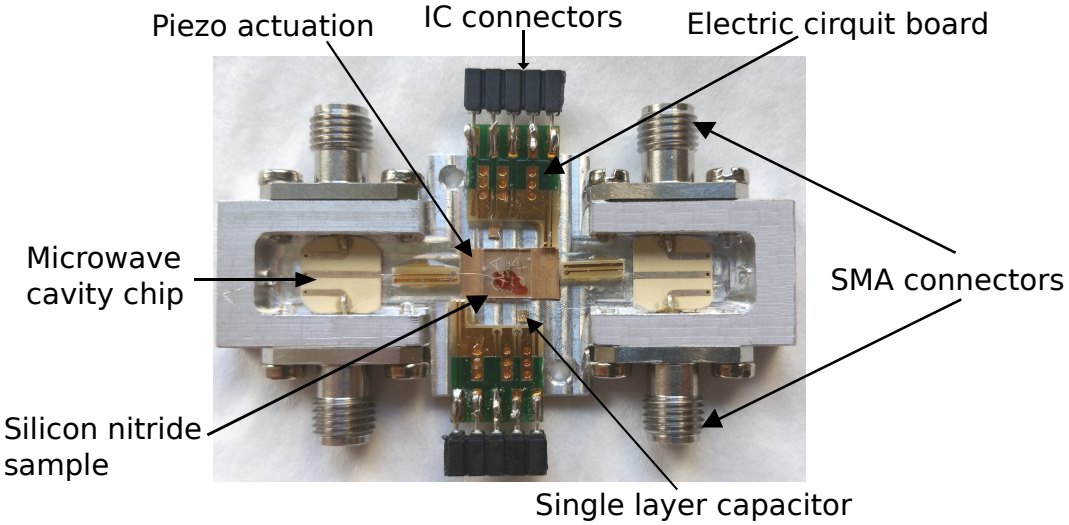

Figure 3.9: Photograph of the sample holder containing two microwave cavities with SMA connectors, two electric circuit boards for dielectric actuation, two single layer capacitors, a piezo crystal and the silicon nitride sample, which is glued on top of the piezo with a red photo resist.

The sample holder is mounted on a piezoelectric positioner stack in a vacuum chamber to provide the positioning of the sample with respect to the laser beam for interferometric readout. Furthermore, all measurements presented in this work were done at room temperature.

Chapter 4

Strong 4-mode coupling

The following section is based on the publication

- K. Gajo, S Schüz and E. M. Weig. Strong 4-mode coupling of nanomechanical string resonators.
  Applied Physics Letters 2017 111:13. Reference [57]

As the publication is original work and has explicitly been written by the author, the following section contains reprinted figures under permission of the journal and indicated as such. The co-authors contributed to this publication in terms of sample fabrication, measurements and discussion of the experimental results. All results of this section are printed under permission of all authors.

In this chapter mechanical mode coupling between the four fundamental flexural modes of a silicon nitride resonator pair will be investigated. The underlying sample geometry is the 2-electrode layout, where only one resonator (referred to as resonator 1) is flanked by two adjacent electrodes for dielectric actuation (see Fig. 4.1, for more details, see section 3.1.1).

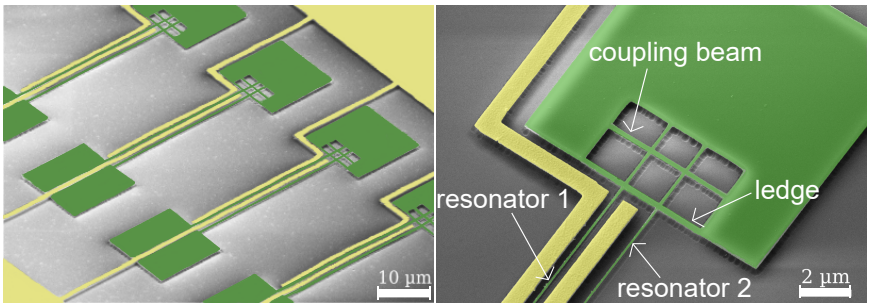

Figure 4.1: SEM false color picture of the 2-electrode-layout (left) with a zoom-in on the shared clamping point with window structure of a resonator pair (Authorized reprint from Ref. [57]).

Resonator 2 has no electrodes and is therefore not electrically accessible neither for dielectric actuation, nor for microwave cavity enhanced readout. The resonators are 100 nm high, 180 nm wide and 55 µm long with a coupling beam width of 200 nm and a window ledge of 300 nm. With these dimensions the resonators match the dimensions selected in chapter 2.
We find the eigenfrequencies of the fundamental flexural modes of resonator 1 and 2 at $\omega_{1O}/2\pi = 6.37\,\text{MHz}$, $\omega_{1I}/2\pi = 6.62\,\text{MHz}$, $\omega_{2O}/2\pi = 6.5\,\text{MHz}$ and $\omega_{2I}/2\pi = 6.75\,\text{MHz}$. Here, O corresponds to the OOP mode and I to the IP mode of the respective resonators. The IP modes are slightly higher in frequency than the OOP modes. This is caused by the fabricational undercut (see chapter 3.1) of the silicon nitride layer at the clamping point. This undercut allows for a slight increase of flexibility of the clamping point in the vicinity of the resonator in OOP direction, corresponding to a minimal increase of the effective resonator length in OOP direction. In IP direction, this is not the case because of the width of the clamping point. Additionally the aspect-ratio of the OOP mode is different as for the IP mode, because the silicon nitride strings are wider than high. This also affects the eigenfrequencies of the IP and OOP modes.
Comparing the OOP frequencies with the eigenfrequency study shown in chapter 2.1, the OOP modes from our experiment match the calculated OOP frequencies very well, with a deviation of about 5%-6%. The frequencies of all four modes are probed simultaneously by the laser interferometric readout and the Q factor of the modes is about 200 000.

4.1 2-mode resonance

To start out, we use the dielectric actuation and tuning technique (chapter 3.2) by applying a DC and RF voltage to the outer electrode of resonator 1 (left electrode in Fig. 4.1) to bring two of the vibrational modes of the system in resonance. The frequency response of the modes as a function of the applied DC voltage from 10 V to 21 V is shown in Fig. 4.2.

The frequency spectrum was obtained via a spectrum analyzer and the resonator was driven with a drive power of $-10\,\text{dBm}$. Two of the modes show a quadratic frequency dependence on the applied DC voltage, and thus can be assigned to the flexural modes of resonator 1. The softening/stiffening of these frequency branches allows for identification of the IP and OOP mode.[58]
As resonator 2 is not electrically accessible, it is actuated only indirectly by strain-induced coupling to the motion of resonator 1. Reference measurements have shown, that the force of the stray electrical gradient field of the electrodes of resonator 1 on resonator 2 is too small[59] to actuate resonator 2. This finding is confirmed by numerical calculations of the electrical force per unit length of the electrical stray field, which yields 10^{-5} N/m (10^{-5} N/m) for the OOP (IP) mode of resonator 1 and only 10^{-8} N/m for OOP and IP of resonator 2 (for more details see chapter 5).
Figure 4.2 reveals an avoided crossing at 17.2 V between the IP mode of resonator 1 (1I) and the OOP mode of resonator 2 (2O). A genetic algorithm[60–62] is used to fit the model of four coupled resonators (chapter 1.2) to the measurement data (see dashed blue lines in Fig. 4.2): The idea

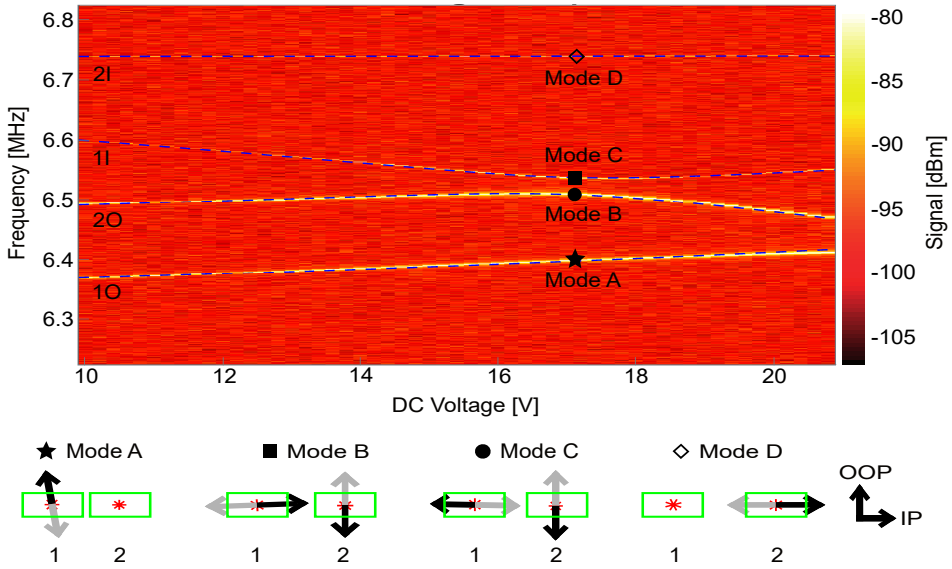

Figure 4.2: Frequency response to a DC voltage sweep of resonator 1 shows an avoided crossing between 2O (OOP mode of resonator 2) and 1I (IP mode of resonator 1) at a voltage of 17.2 V. The two mode resonance of mode 2O and 1I leads to the hybridized modes B and C. The other modes (1O and 2I) remain largely unaffected as mode A and D. The blue dashed lines show the fit of the analytic model, yielding a coupling strength of $g_{2O,1I}/2\pi = 29.7\,\text{kHz}$. The black arrows show the mode polarization (↕: OOP, ↔: IP) of modes A, B, C and D, respectively, at 17.2 V; grey arrows show the inverse to illustrate the vibration of the resonators. Authorized reprint from Ref. [57].

of a genetic algorithm is to mimic an evolutionary process including so called *generations* and *populations*. It starts with the first generation, where a population of several individuals is created and one individual corresponds to one parameter set, which is randomly generated from start parameters and a corresponding given parameter range. Then a *fitness-test* is made for each individual of the population. This fitness-test is the sum of squared deviations between the model's results and the start parameters. If the fitness value is small, the individual is "fit". From each generation, those individuals who are the fittest will be selected as "elite" and passed on to the next generation. Hence, the next generation consist of those fittest individuals and additionally the population will be filled up with individuals which are created from mutations and cross-overs of the individuals of the former generation, which were considered not the fittest, but fit-enough to pass some of their genes. One gene corresponds to one parameter. This procedure is repeated until the maximum number of generations is reached, or a user defined tolerance is exceeded.
As this algorithm includes randomness functions to create new individuals, the results of the genetic fit are never 100% identical. However, if the fit is set up carefully and the relevant start and fit parameters are chosen, the result is well reproducible. Our genetic algorithm requires the intrinsic angular eigenfrequencies in absence of coupling ω_{i0}^*, the quadratic tuning factors c_i with the cubic corrections d_i, as well as the offset of the tuning parabolas U_{i0} and the coupling

strengths g_{ij} as start parameters. The indices i (and j) are assigned to the flexural modes of the resonators as: $i = 1$: 1O, $i = 2$: 2O, $i = 3$: 1I, and $i = 4$: 2I.
The genetic fit reproducibly describes the frequency response of the modes and yields a coupling strength of $g_{2O,1I}/2\pi = 29.7\,\text{kHz}$ between mode 2O and 1I. This value lies well above (more than two orders of magnitude) the linewidths of the modes, which are in the range of 70-80 Hz, and therefore verifies that the system is deeply within the strong coupling regime. Moreover, the coupling between mode 2O and 1I is of pure mechanical nature, since resonator 2 is only slightly affected by the electrical gradient field. As it is an inter-string coupling, it confirms the impact of the window structure on the enhancement of strain mediated mode coupling (see chapter 1.2.2).
In the area of the avoided crossing, the 2O and 1I modes are in resonance, and thus hybridize to hybrid normal modes, equal to the symmetric and antisymmetric normal modes of two coupled resonators.[6] By solving the eigenvalues from Eq. (1.11) we can calculate the eigenvectors $\vec{n}_i$ of the corresponding modes:

$$\vec{u}_i(t) = \sum_{i \neq j} \vec{n}_i(t) \varepsilon \cos(\omega_j t + + \vartheta_j). \tag{4.1}$$

The parameters ε and ϑ_j are determined by initial conditions. These eigenvectors can be understood as the polarization vectors of the mode (black arrows in Fig. 4.2; grey arrows show the inverse direction to emphasize the motion of the mode), and hence as the mode polarization itself. The solution of the eigenvalue problem represents the contributions of the respective resonators 1 and 2 to the resulting polarization vector. For resonant modes, we can distinguish between an in-phase and an out-of-phase hybridized normal mode. In-phase corresponds to the case when both polarization vectors point in either the positive, or the negative direction of the I-O axis (as defined in Fig. 4.2). Out-of-phase means one polarization vector pointing in the positive direction and the other pointing in the negative I-O axis direction. With Eq. (4.1) we can calculate the mode polarization of all four modes for each DC voltage applied to the system, and thus retrace the hybridization of the modes. In the area of the avoided crossing (at 17.2 V), where the modes are hybridized, we can no longer just identify the frequency branches with the flexural IP an OOP modes of the system, but with the hybrid modes A, B, C and D (see Fig. 4.2). For mode 2I we find no contribution to the avoided crossing, and thereby its' polarization vector shows a clear in-plane polarization over the whole voltage range, and therefore mode D can be directly identified as mode 2I. Mode 1O shows a clear out-of-plane polarization until a voltage near 21 V where it starts hybridizing with 2O, hence mode A can be identified with 1O. However, according to the polarization vectors in the avoided crossing, mode C is a hybrid in-phase mode and mode B is a hybrid out-of-phase mode. This is another evidence of strain mediated strong inter-string coupling, as modes of both strings hybridize to normal modes of the coupled system.
By exposing the resonators to a large DC voltage over a long time period (> 24 h) it is possible to support the buildup of static dipoles in the silicon nitride of the driven resonator (resonator 1). This can be reversed by venting the vacuum chamber. The induction of static dipoles results in a shift of the vertices U_{10} and U_{30}, and thus in a shift of the tuning curves of mode 1O and

1I. Therefore, it is possible to go beyond the 2-mode resonance and bring even 3 modes of the system in resonance; all with the same set of resonators.

4.2 3-mode resonance

To obtain a power spectrum of the 3-mode resonance, a voltage sweep is performed from -21 V to 21 V and the frequency response of the mode is recorded by a vector network analyzer while the drive power is fixed to -10 dBm. Figure 4.3 shows the frequency response of the modes in dependence of the applied DC voltage, revealing multiple avoided crossings. In fact, we find a 3-mode resonance, as three avoided crossings appear almost simultaneously and interfere.

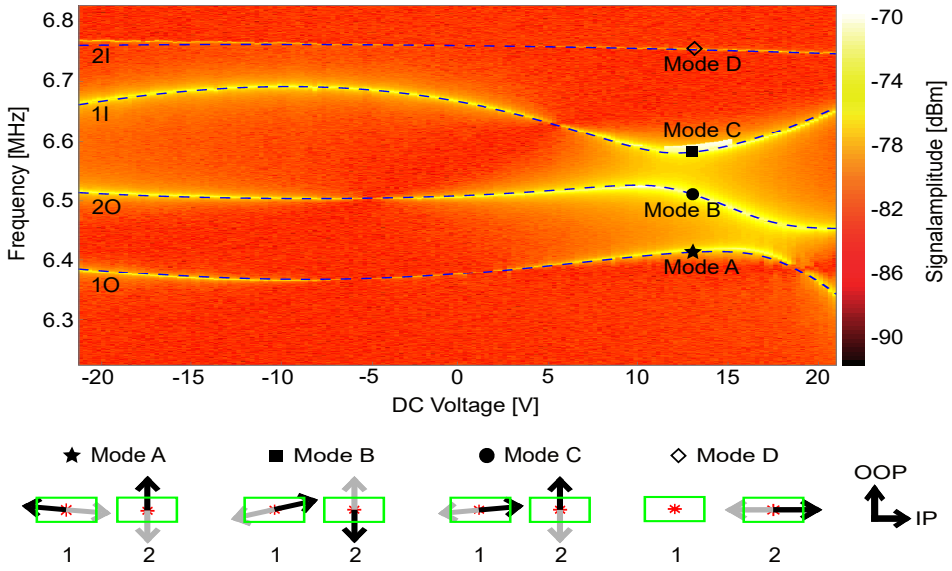

Figure 4.3: Frequency response to a DC voltage sweep of resonator 1 shows 3-mode resonance: multiple avoided crossing between 1O, 2O and 1I. The 3-mode resonance leads to the hybridized modes A, B and C. Mode 2I remains unaffected by the hybridization (mode D). The blue dashed lines show the fit of the analytic model, yielding coupling strengths of $g_{1O,2O}/2\pi = 130$ kHz, $g_{2O,1I}/2\pi = 60$ kHz, and $g_{1O,1I}/2\pi = 50$ kHz. The black arrows show the mode polarization ($\updownarrow$: OOP, $\leftrightarrow$: IP) of modes A, B, C and D at 13.4 V; grey arrows show the inverse to illustrate the vibration of the resonators. The logarithmic color scale shows the signal amplitude. Authorized Reprint from Reference [57].

Avoided crossings can be found at about 11 V between modes 2O and 1I, between 11 V and 16 V between modes 1O and 1I and at about 16 V between modes 1O and 2O. For the 3-mode resonance, the coupling strengths cannot be set equal to the frequency splitting of the modes, as the avoided crossings overlap each other. Especially, the avoided crossing between modes 1O and 1I and the respective coupling strength cannot be estimated from the spectrum in Fig. 4.3. Therefore we apply the genetic algorithm (dashed blue lines), which yields coupling strengths of $g_{1O,2O}/2\pi = 130$ kHz, $g_{2O,1I}/2\pi = 60$ kHz, and $g_{1O,1I}/2\pi = 50$ kHz. Again, the coupled modes are deep within the strong coupling regime and just like for the 2-mode resonance, mode

2I remains unaffected by the avoided crossings. Furthermore Fig. 4.3 reveals an asymmetry in the intensity profiles of the modes, indicating that they become highly nonlinear in the area of resonance. Figure 4.4 shows a linecut of Fig. 4.3 at 13.4 V. The amplitude responses of modes A, B and C are clearly nonlinear. As mode D is not participating in the multi-mode avoided crossing, its amplitude response remains linear.

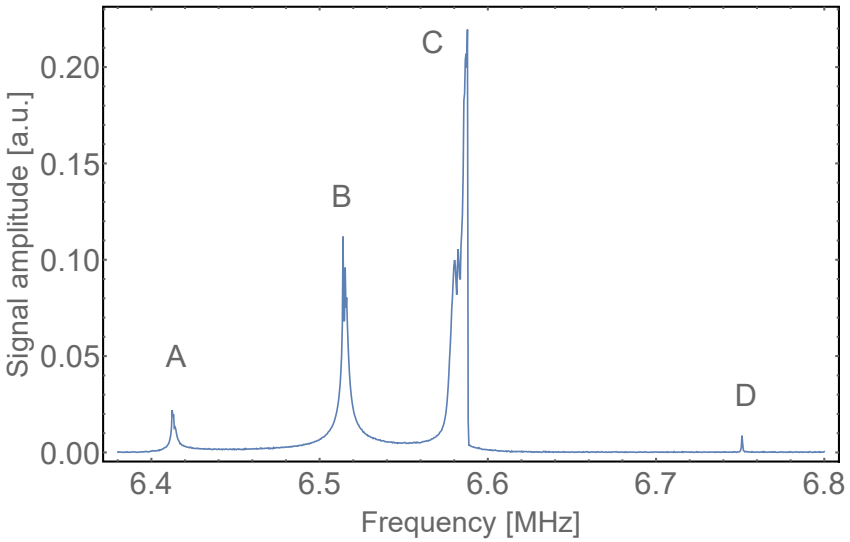

Figure 4.4: Linecut of Fig. 4.3 at 13.4 V shows that the amplitude response of the hybrid modes A, B and C is nonlinear. Mode D is not affected by the avoided crossings, and thus still is linear.

Different from the 2-mode resonance, the 3-mode resonance reveals not only mechanical inter-string coupling, but combines mechanical inter-string (between modes 1O and 2O and between modes 2O and 1I) and dielectrical intra-string coupling (between modes 1O and 1I).
If, however, a coupling strength of $g_{1O,1I}/2\pi \approx 0\,\text{kHz}$ is assumed, the prediction of the modes' behavior done by the genetic algorithm does not at all fit the actual measurement data. Only if a start parameter in the range of $g_{1O,1I}/2\pi \approx 30$ -60 kHz is plugged into the algorithm it yields a good estimation of the mode's behavior. This assures the assumption that for the 3-mode resonance, we have a combination of mechanical and dielectrical coupling.
The calculated polarization vectors of the modes give more insight in how the modes hybridize in the region of resonance, i.e. at a voltage of 13.4 V (see Fig. 4.3). Mode A and B belong to out-of-phase hybrid modes, with an opposing relative phase, whereas mode C belongs to an in-phase hybrid mode. Looking at the overall polarization of the modes throughout the whole voltage sweep, we find that the lowest mode branch starts out as a pure out-of-plane mode (1O) at -21 V, then hybridizes into mode A and finally transforms into an in-plane mode (1I) at 21 V. The second branch starts as well as pure out-of-plane (2O at -21 V), then hybridizes with mode 1I into hybrid mode B, and as such, hybridizes with mode 1O and in the end turns back into an out-of-plane mode (2O) at 21 V. For the third mode branch, we find the inverse behavior of the first mode branch: starting as a pure in-plane mode (1I) at -21 V, it hybridizes into mode C and finally ends up as an out-of-plane mode (1O) at 21 V. As mode 2I stays largely unaffected by

the electrical field, and hence can not be tuned in resonance with the other modes, mode D can be identified as 2I.
So far, the spectra have been measured employing the laser interferometric readout. In a next step, we are interested in whether the microwave cavity enhanced readout allows for detection of multi-mode resonances.

4.3 Microwave cavity readout

As for the 2-electrode sample geometry only one resonator can couple to the microwave cavity, it is only the motion of this resonator, that modulates the signal in the microwave cavity, and thus only this resonator can be detected directly via the microwave cavity.

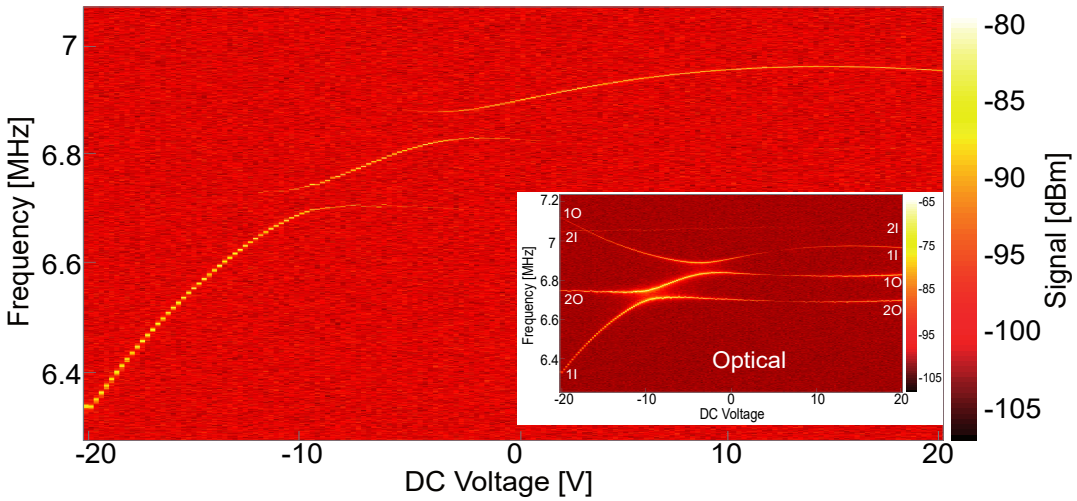

Figure 4.5: DC voltage sweep of resonator 1 over a voltage range from -21 V to 21 V measured with the microwave cavity readout technique, revealing an avoided crossing at about -10 V and one at -2.5 V. Inset shows the respective voltage sweep, measured via the laser interferometric readout, showing the same avoided crossings.

Therefore, it is not self-evident, that any motion of the second resonator can be detected, or that the avoided crossings, where modes of the second resonator are involved, can be measured by this technique.
For further investigation on this topic, a $\lambda/4$ microwave cavity is inductively coupled to resonator 1 in such a way, that the outer electrode of the system can be used for dielectric actuation and the electrode in the middle between the resonators is coupled to the microwave cavity (see Fig. 3.6 in chapter 3). Please note, that the dimensions and geometry of the sample introduced here is identical to the system employed in sections 4.1 and 4.2 but the sample is a different one. Therefore, the eigenfrequencies, as well as their tuning strength slightly differs from the modes shown in chapters 4.1 and 4.2.
The microwave cavity is resonantly driven by a signal generator at $\omega_{\lambda/4} = 3.417\,\text{GHz}$ with a drive power of $+15\,\text{dBm}$. A power spectrum measured with the microwave cavity enhanced

readout is shown in Fig. 4.5. The voltage was swept from − 21 V to 21 V and the drive power of the applied white noise was −10 dBm. Two avoided crossings are apparent at about −10 V and −2.5 V. Obviously, only one mode is tracked over the whole voltage range, whereas other modes are only visible in the vicinity of the avoided crossings. For clarification of the modes' identities, the inset of Fig. 4.5 shows a power spectrum of the same resonator pair measured via the laser interferometric readout, where all four modes can be well identified apart from the avoided crossings.
Taking a closer look at the area of the avoided crossing, that is, repeating the voltage sweep for a smaller voltage range (−17 V to 17 V) and detecting a smaller frequency range with the microwave cavity, reveals that the microwave cavity indeed is sensitive to inter-string and intra-string resonances. This can be seen in Fig. 4.6.

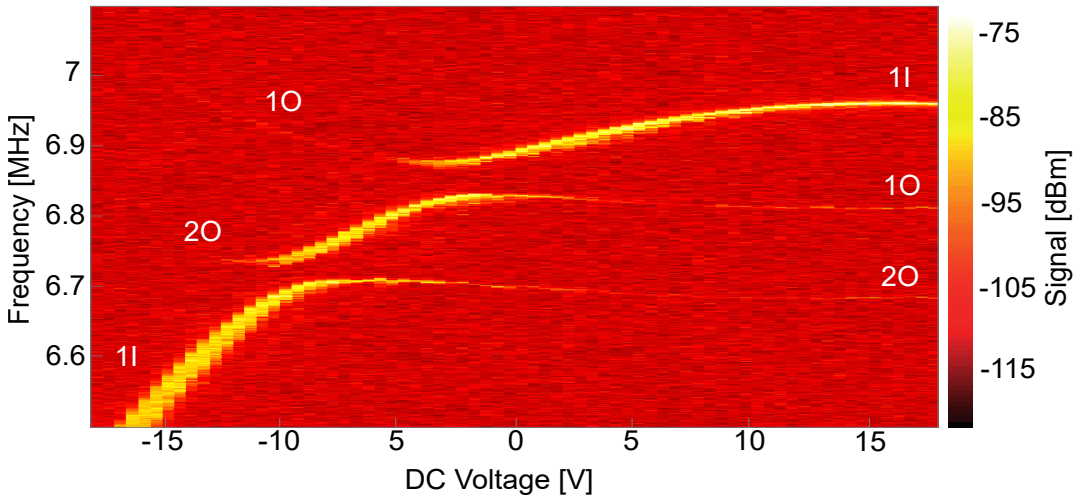

Figure 4.6: DC voltage sweep of resonator 1 over a voltage range from −17 to 17 V measured with the microwave cavity readout technique. Two pronounced avoided crossings are visible, with modes of both resonators being involved. According to the spectrum detected via the laser interferometer, the modes of the resonators can be identified apart from the avoided crossings, showing that the 2O mode of resonator 2 can be detected by the microwave cavity in the vicinity of the avoided crossing.

The spectrum shows, that the 2O mode can be detected by the microwave cavity, as it starts to hybridize with mode 1I and even beyond the avoided crossing. As mode 2O and 1I hybridize to a hybrid normal mode that "lives" on both resonators 1 and 2, it is not exceptional, that a microwave cavity coupled to one resonator is also sensitive to modes of the other in the proximity of an avoided crossing. Therefore, these measurements confirm the strain-mediated inter-string coupling of the silicon nitride resonators and assure the sensitivity of the microwave cavity enhanced readout to inter-string coupling.
The signal of 1O is way weaker than mode 1I. This may arise out of the absolute position of resonator 1 between the adjacent gold electrodes. Since the electrical gradient field surrounding resonator 1 is highly nonlinear, the absolute position of the resonator has major impact on the

tuning strength of the modes as well as on the sensitivity of the microwave cavity enhanced readout.

For all measurements shown here, only 2- and 3-mode resonances are present, but no 4-mode resonance could be observed. The IP mode of resonator 2 is the mode with the highest frequency at 0 V and usually has the biggest frequency difference to all other modes. As it is not affected by the dielectric tuning mechanism, it is difficult to bring other modes in resonance with mode 2I. However, by increasing the available DC voltage range, it might be possible to access avoided crossings between 2I and 1O.

Chapter 5

Static electrical fields

The inhomogeneous electric gradient field of the electrodes surrounding the resonators has a non-trivial influence on the frequency response of the silicon nitride resonators.[41,58]
To this extent it is necessary to investigate not only on the impact of the RF and DC field component, which is used for dielectric actuation and tuning of the modes, but also on the effect of additional electrical fields, with regard to the 3- and 5-electrode geometry, where 2 inhomogeneous electrical gradient fields interact. Measurements reveal a nontrivial dependency of the frequency tuning behavior of the resonators' modes on additional static electrical fields applied to the electrodes.

5.1 Electrical force

Depending on the position of the silicon nitride resonator with respect to the gold electrodes, the electrical force acting on the resonator differs massively. This holds not only for the resonator next to an electrically addressed electrode (for example resonator 1 in chapter 4), but also for the resonator which is subject to the electrical field leaking over the middle electrode (for example resonator 2 in chapter 4).
A calculation of the electric force per unit length yields 10^{-5} N/m for the OOP mode and 10^{-6} N/m for the IP mode of the actively driven resonator, but 10^{-8} N/m for the OOP and IP mode of the passive resonator (6^{-8} N/m for OOP, 1^{-8} N/m for IP). These results show, that the force acting on the actively driven resonator is at least two orders of magnitude higher than for the indirectly exposed resonator. Figure 5.1 underlines these results. It shows the simulated electrical potential caused by a voltage of -5 V applied to the outer left electrode (electrode A) for the 3-electrode geometry. The other electrodes B and C are grounded. All electrodes and resonators are shown in a cross-sectional view for a better understanding of the spatial dispersion of the electric potential.
As Fig. 5.1 shows, resonator 1 is surrounded by the inhomogeneous electrical gradient field, while resonator 2 sees an almost constant electric potential. This emphasizes the findings from chapter 4 and additional reference measurements which have shown, that the resonator subject

to the electric field leaking over the middle electrode (resonator 2) is not driven by the electric field applied to electrode 1, but is indirectly actuated by the motion of resonator 1.

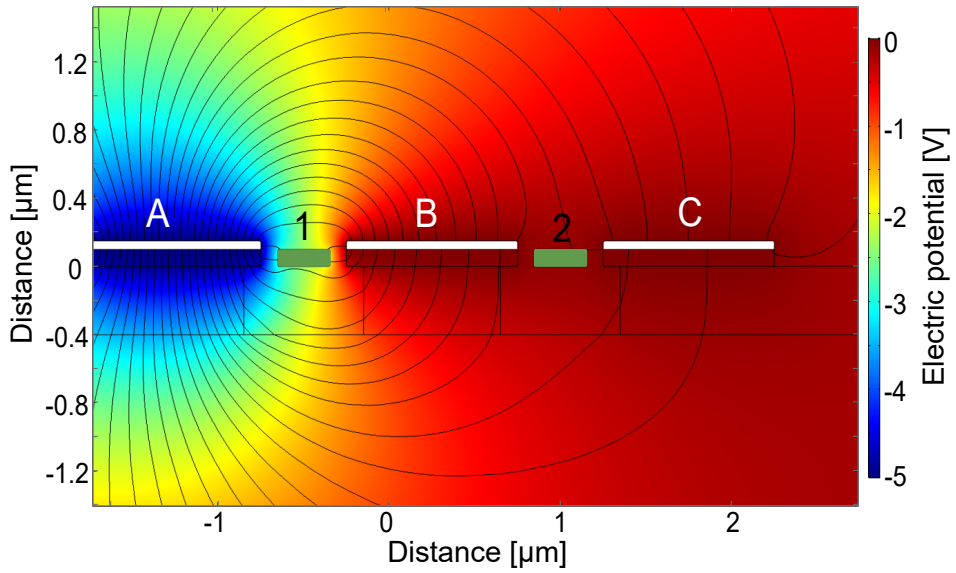

Figure 5.1: Finite element simulation of the electrical potential for a voltage of $-5\,\mathrm{V}$ applied to electrode A on the left of resonator 1. While resonator 1 is well within the inhomogeneous electrical field, resonator 2 sees an almost static electrical potential leaking through electrode B. Electrodes B and C are grounded; color scale shows electric potential.

Nevertheless, resonator 2 is exposed to a static electric potential higher than 0 V, and thus can be influenced by electric fields originating from electrode A. The same holds for resonator 1 with respect to electrical potentials applied to electrode C: if an electrical potential is applied to electrode C, resonator 1 is exposed to an electrical field, with an electrical force acting on the resonator (compare the calculated electric force per unit length above).

5.2 Amplification of frequency tuning

The following section is based on data acquired in the scope of the Master's Thesis

- Martin Schill: Dielektrische Kontrolle gekoppelter nanomechanischer Resonatoren (University of Konstanz). Reference [63]

As the Master's Thesis was organized and supervised by the author, the following section contains re- and further evaluated data that was measured in the scope of the Master's Thesis. The author contributed to the acquirement of the data in terms of sample fabrication, measurements, evaluation and discussion.

If a DC and RF voltage is applied to electrode A and an additional DC is applied to electrode C (see Fig. 5.1), the DC on electroce C will change the frequency tuning behavior of resonators 1 and 2 caused by the DC on electrode A. To investigate on the relation between changes in frequency tuning and the strength of an additional DC bias, a RF white noise is applied to electrode A and C on a 3-electrode layout sample (see chapter 3.1.2) to dielectrically actuate both resonators 1 and 2. A DC voltage is applied to electrode C, to which we will refer to as U_C. Additionally a DC bias is applied to electrode A (U_A), which is varied from -32 V to 32 V. For every U_A applied on electrode A, a DC voltage sweep is performed by varying U_C from -21 V to 21 V, so we end up with a set of 65 measurements, for 65 different voltages U_A. As these measurements show, the frequency tuning behavior of the resonators modes in dependence of U_A strongly depends on the mode shape.
Figure 5.2 shows the frequency response of the modes as a function of the DC voltage U_C for two different voltages U_A of -32 V (left) and 32 V (right).
Because of the tuning behavior with respect U_C and the softening and stiffening of the modes we can identify the 1O, 1I, 2O and 2I modes of the resonator system. Both spectra show the same order of the modes, that is 2I being the one with the highest frequency, 2O above 1I and 1O being the lowest frequency branch.

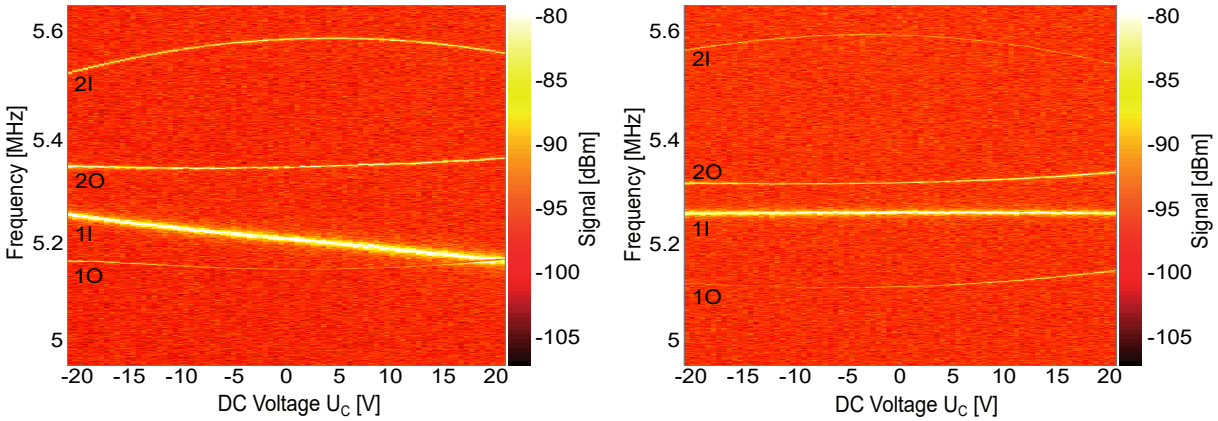

Figure 5.2: U_C voltage sweeps of resonator 2 for two different voltages U_A applied to electrode A. The left spectrum was obtained at a voltage U_A of -32 V, the right spectrum for 32 V. While the left spectrum shows an interstring avoided crossing between modes 1O and 1I, the right spectrum does not show this avoided crossing, as the frequency separation of the modes is too big. Mode 1I shows a linear DC tuning behavior and even changes the DC tuning direction with the static potential.

We find that the absolute positions of the frequency branches changes with U_A. As the left spectrum of Fig. 5.2 shows an avoided crossing between modes 1O and 1I (interstring resonance) at a DC voltage of $U_C \approx 18$ V, we can not see this behavior in the right spectrum, because here, the frequency offset between the modes is too big. Consequently, the application of additional DC voltages allows for tuning modes in and out of resonance in an arbitrary fashion. Furthermore, the tuning behavior of the modes changes dramatically with the static potential

U_S depending on the mode, as can be seen on modes 1I and 2O. We also find a shift of the DC tuning-parabola vertex of mode 2I from 4 V at $U_A = -32$ V to -5 V at $U_A = 32$ V. To gain a deeper understanding on this relation, all four modes are examined on their frequency shift and change of frequency tuning.

5.2.1 1O (Out-of-plane mode of resonator 1)

Mode 1O shows a rather weak, but still quadratic tuning with U_C. However, mode branch 1O experiences a frequency shift when U_A is changed. For a DC voltage of $U_C = 0$ V the eigenfrequency of the mode changes from 5.05 MHz to above 5.13 MHz (see Fig. 5.3), when U_A is varied from -32 V to 32 V. This is a frequency shift of more than 90 kHz. The eigenfrequency was extracted from all 65 voltage sweeps of U_A, at $U_C = 0$ V respectively. As some modes go through avoided crossings when U_A is changed, it was not possible to extract the undisturbed eigenfrequencies at lower voltages U_C for all modes. Therefore a DC voltage of $U_C = 0$ V was chosen, being far enough from all avoided crossings, and hence allowing for extraction of the undisturbed frequencies of all modes for all applied voltages U_A. Figure 5.3 shows the frequency of mode 1O (blue dots). It depends quadratically on U_A.

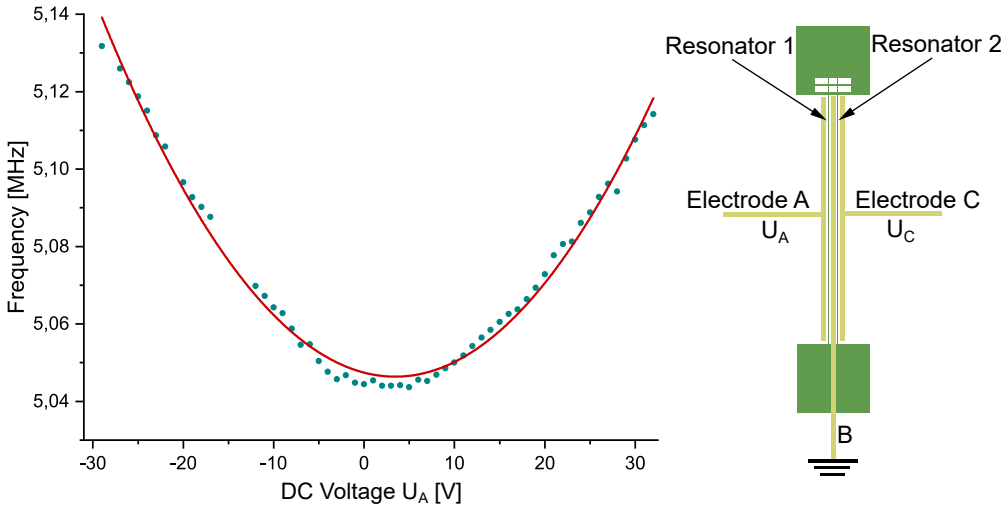

Figure 5.3: Extracted eigenfrequencies of mode 1O at a DC voltage of $U_C = 0$ V (applied to electrode C) for voltages U_A between -32 V and 32 V (applied to electrode A), showing a frequency shift of more than 90 kHz depending quadratically on U_A. Blue dots are measured data points, red curve is a quadratic fit to the data. Inset shows a schematic of the sample with respective electrodes.

According to Eq. (3.3), a quadratic fit (red line) was made to obtain the quadratic tuning coefficient c_t with U_A

$$\omega_{1O}(U_A) = \omega_{10}^* + 2\pi b U_A + 2\pi c_t U_A^2 \tag{5.1}$$

$$\omega_{1O}(U_A) = 2\pi \cdot 5.047 \cdot 10^6\,\text{Hz} - 2\pi \cdot 606\,\frac{\text{Hz}}{\text{V}} \cdot U_A + 2\pi \cdot 88\,\frac{\text{Hz}}{\text{V}^2} \cdot U_A^2. \tag{5.2}$$

The quadratic fit yields a quadratic tuning of $c_t = 88\,\text{Hz/V}^2$, which is higher than the tuning strength of $22\,\text{Hz/V}^2$ with U_C in absence of the additional DC bias U_A. Equation (5.3) also contains a linear correction term with a linear tuning coefficient b. The fact, that mode 1O is affected more by U_A than by U_C becomes more clear, if one visualizes, that the U_A is applied to electrode A, flanking resonator 1 and U_C is applied to electrode C, flanking resonator 2.
Besides a shift in frequency, U_A causes a change in the U_C dependent tuning factor c_{1O} (see Eq. (3.3). We find an additional stiffening of the 1O mode, that is an increase in the quadratic U_C dependent tuning, when U_A is changed. By extracting the 1O frequency branch from every measured spectrum, it is possible to extract the U_C dependent tuning factor c_{1O} for each U_A. Figure 5.4 shows the quadratic tuning factor c_{1O} as a function of U_A, revealing a quadratic dependence.

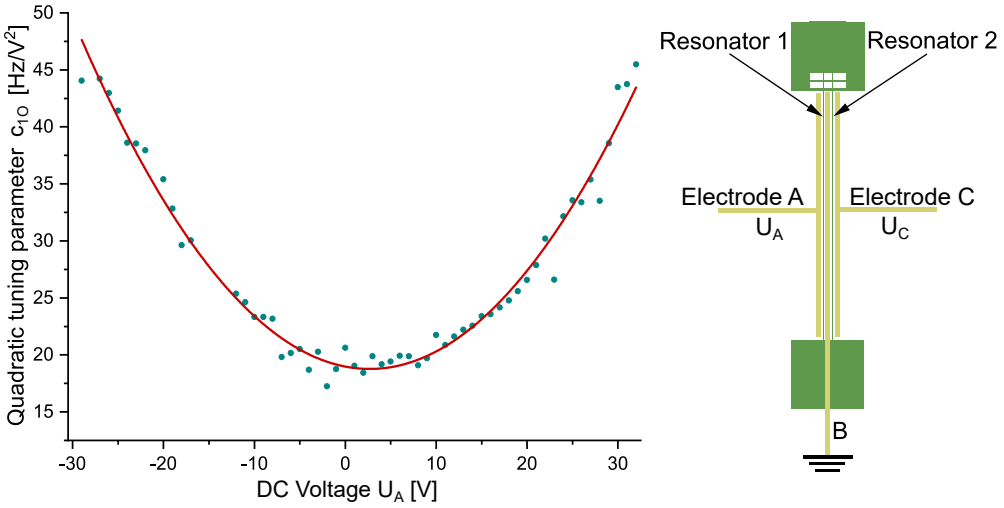

Figure 5.4: Extracted quadratic U_C tuning factor c_{1O} of mode 1O as a function of U_A, showing a quadratic dependence on U_A in turn. Blue dots are measured data points, red curve is a quadratic fit to the data. Inset shows a schematic of the sample with respective electrodes.

We find a maximum increase in the U_C tuning strength from $16\,\text{Hz/V}^2$ to more than $45\,\text{Hz/V}^2$, corresponding to an amplification of the tuning by more than 180%.
By applying a quadratic fit (red line) to the data, we can obtain the quadratic stiffening coefficient ξ_{1O} of the quadratic U_C tuning c_{1O}:

$$c_{1O}(U_A) = c_{1O}(U_A = 0) + \xi_{1O} U_A^2 \tag{5.3}$$

$$c_{1O}(U_A) = 20.681\,\frac{\text{Hz}}{\text{V}^2} + 0.0287\,\frac{\text{Hz}}{\text{V}^4} \cdot U_A^2. \tag{5.4}$$

Equation (5.4) gives a stiffening coefficient of about 0.0287 Hz/V^4, allowing to enhance the tuning factor c_{1O}, over a range of 30 Hz/V^2.
Figure 5.5 displays the frequency dependence on the DC voltage and the static potential, in order to visualize the double-quadratic relation.

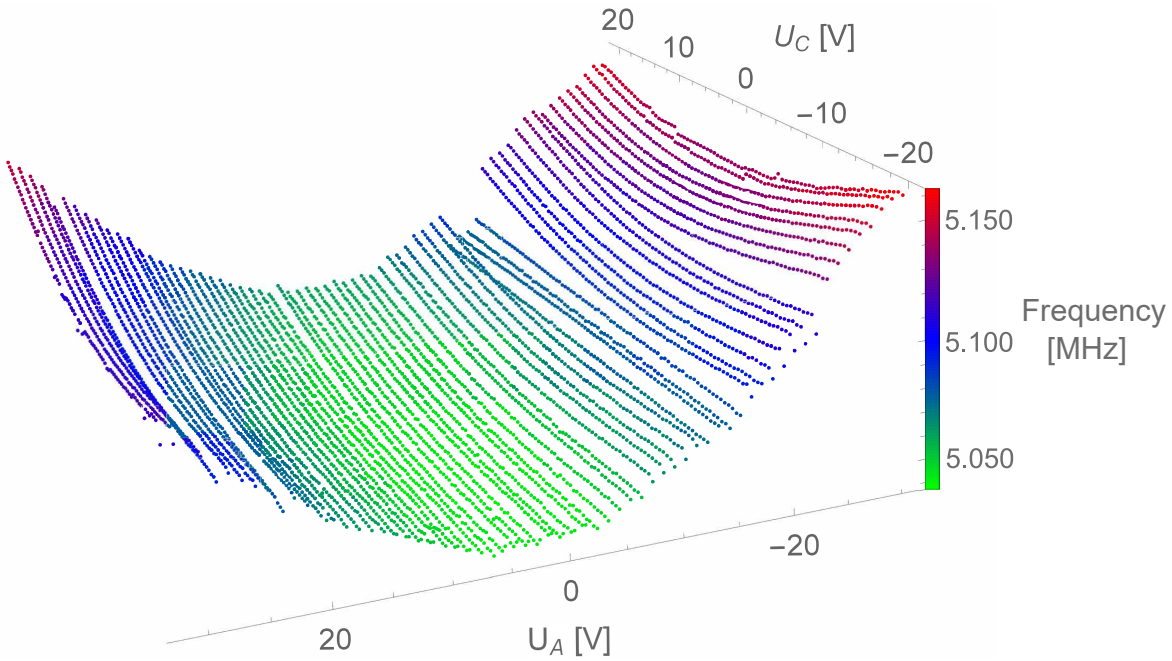

Figure 5.5: Frequency of mode 1O as a function of U_C and U_A, showing a quadratic tuning of the frequency with both, U_C and U_A. The additional DC bias U_A has a strong impact on the quadratic U_C dependence of the frequency.

For some voltages U_A between -10 V and -14 V the typical U_C tuning parabolas become flattened out, while for U_A higher than 20 V and lower than 20 V bending of the parabolas is increased. Furthermore, the vertexes of the U_C tuning parabolas are overall shifted from $U_C = -13$ V up to 3 V.
The quadratic frequency tuning of mode 1O with U_A applied to electrode A was to be expected, as resonator 1 is dielectrically coupled to the electric field centered at its adjacent electrode A. Concerning the increased tuning ratio with the U_A compared to the tuning with the U_C, this is based on the position of the resonator: electrode A is adjacent to resonator 1 (with a nominal distance of 300 nm), while electrode C is nominally more than 2 µm apart, what results in a strong coupling to electrode A and a rather weak, but non-negligible coupling to electrode C.

5.2.2 1I (In-plane mode of resonator 1)

For mode 1I, we find that its eigenfrequency depends in a linear fashion on the U_C applied to electrode C (see Fig. 5.2), although, in the dipole approximation, the eigenfrequency is estimated to show a quadratic DC voltage dependence (see Eq. (3.3)). However, the resonators

here experience an electrical gradient field, which is composed of two electrical potentials: the DC bias at electrode C and the additional DC voltage at electrode A. The force acting on the resonators, thus depends on an effective electrical field E_{eff} and can be written similar to Eq. (1.12):

$$\vec{F}_{el} = -\nabla(\alpha \vec{E}_{eff}^2), \tag{5.5}$$

with the dipole momentum $\vec{p} = \alpha \vec{E}_{eff}$ and complex scalar polarizability[58] $\alpha = \alpha' + i\alpha''$.
We can consider the electrical gradient field in dependence of a variable coordinate[58] ζ (with ζ =x,z) as $E_{eff}(\zeta) = E_0 + E_1(\zeta)$ and obtain the energy W

$$W_{stored} = \alpha'(E_0 + E_1\zeta)^2 \tag{5.6}$$
$$W_{loss} = \alpha''(E_0 + E_1\zeta)^2. \tag{5.7}$$

And just like in Eq. (3.2) the electrical spring constant k_e can be derived and thereby the angular eigenfrequency in dependence of the electrical field is

$$\omega_{i0} = 2\pi\sqrt{\frac{k_0 + k_e}{m}} \approx \omega_{i0}^* + 2\pi\frac{\alpha' E_1^2}{2m\omega_{i0}^*}. \tag{5.8}$$

Here, both, the DC bias U_C and the additional DC bias U_A add up to the electrical field $E = E_A + E_C$ seen by the resonator. The proportionality of electrical field and electrical potential allows to write the eigenfrequency in terms of the DC bias U_C and the additional DC bias U_A with proportionality factors β and χ

$$\omega_{i0} \approx \omega_{i0}^* + 2\pi\frac{\alpha'(\beta U_A + \chi U_C)^2}{2m\omega_{i0}^*}. \tag{5.9}$$

As U_A is constant within one U_C voltage sweep measurement, the term quadratic in U_A gives an additional static offset $\delta\omega_{i0}^*$ of the eigenfrequency

$$\omega_{i0} \approx \omega_{i0}^* + \delta\omega_{i0}^* + 2\pi\frac{2\alpha'\beta U_A\chi U_C}{2m\omega_{i0}^*} + 2\pi\frac{\alpha'\chi^2 U_C^2}{2m\omega_{i0}^*}. \tag{5.10}$$

Since the coupling of resonator 1 is much stronger to U_A on electrode A, than to the electrical field caused by the DC bias U_C at electrode C, because of the spacial distances between resonator 1 and electrode A (nominally 300 nm) and C (nominally 2,08 µm), we can assume $\beta >> \chi$ for mode 1I. If additionally the geometric proportionality between the applied DC bias U_C (U_A) and the resulting electrical field seen by mode 1O E_C (E_C) is small, we find the the proportionality factors $\chi < 1$ and $\beta < 1$. For these reasons ($\beta >> \chi$ and $\chi, \beta < 1$) the term proportional in U_C^2 in Eq. (5.10) becomes negligible compared to the term proportional to $U_A \cdot U_C$. Thus, resonator 1 has a linear component in the electrical field dependence of the eigenfrequency of mode 1I

$$\omega_{1I} \approx \omega_{1I}^* + \delta\omega_{1I}^* + 2\pi b U_C, \tag{5.11}$$

with a linear tuning factor b.
The linear tuning behavior of mode 1I, changes immensely with the applied additional DC bias U_A. Figure 5.6 shows the linear tuning factor b of mode 1I with U_C, as a function of U_A. The linear tuning strength of mode 1I decreases from -2.2 kHz/V to slightly above 0 kHz/V, showing an inversion of the actual U_C tuning behavior from strong negative to even weak positive tuning.
However, the linear U_C tuning of mode 1I can not be extracted for all U_A, as it becomes resonant with mode 2O in the range of $U_A = -25$ V to -13 V and from 25 V to 30 V. Therefore, these datasets are not considered here.

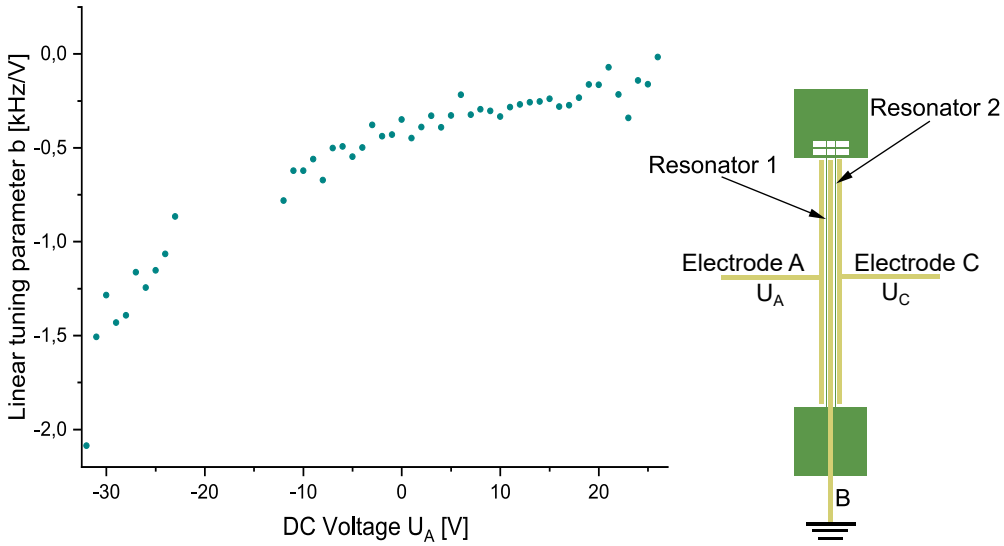

Figure 5.6: Extracted linear U_C tuning factor b of mode 1I as a function of U_A (applied to electrode A), showing an unsteady but still linear dependence on the static potential in turn. Blue dots are measured data points. Inset shows a schematic of the sample with respective electrodes.

Looking at the frequency tuning of mode 1I depending on U_A we find the quadratic tuning behavior expected from Eq. (3.3). The eigenfrequency of mode 1I at a DC voltage of $U_C = 0$ V was extracted from the power spectra obtained for different U_A from -32 V to 32 V and is shown in Fig. 5.7. By adjusting U_A, the 1I-eigenfrequency can be tuned from 5.15 MHz to over 5.42 MHz, corresponding to a frequency increase of more than 250 kHz, giving rise to a tuning range of about 5% of the eigenfrequency.
The red curve shows the quadratic fit to the data (blue dots) in order to obtain the quadratic tuning factor c_t

$$\begin{aligned} \omega_{1I}(U_A) &= \omega_{1I}^{*} + 2\pi b U_A + 2\pi c_t U_A^2 \\ \omega_{1I}(U_A) &= 2\pi \cdot 5.413 \cdot 10^6\,\text{Hz} - 2\pi \cdot 864\,\frac{\text{Hz}}{\text{V}} \cdot U_A - 2\pi \cdot 173\,\frac{\text{Hz}}{\text{V}^2} \cdot U_A^2. \end{aligned} \tag{5.12}$$

Apparently, with a quadratic tuning of -173 Hz/V^2 the 1I mode shows a much higher frequency tuning with U_A than mode 1O, which tunes with 88 Hz/V^2, and hence almost half as strong as mode 1I.

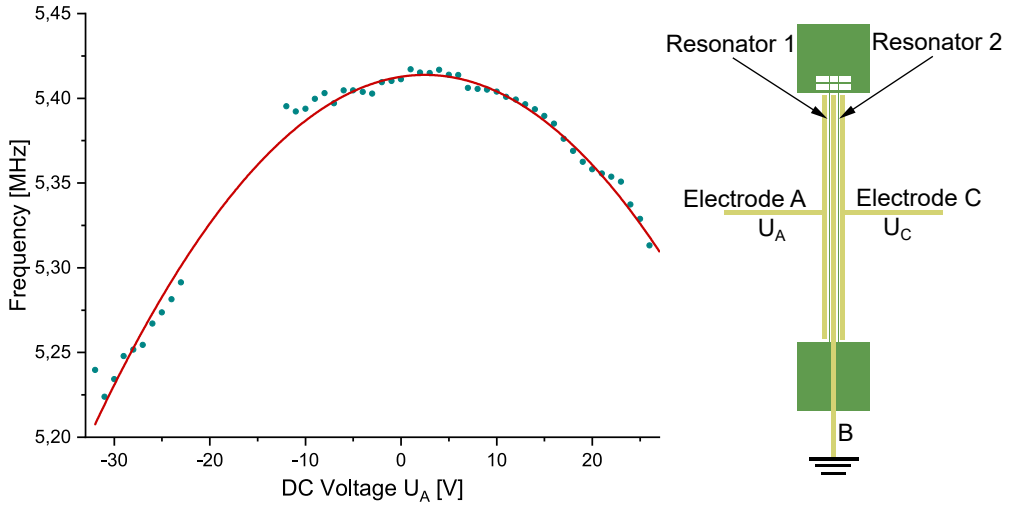

Figure 5.7: Extracted eigenfrequencies of mode 1I at a DC voltage of $U_C = 0\,\mathrm{V}$ (applied to electrode C) for different U_A between $-32\,\mathrm{V}$ and $32\,\mathrm{V}$ (applied to electrode A) show a quadratic dependence on U_A. The frequency can be shifted by more than 250 kHz. Blue dots are measured data points, red curve is a quadratic fit to the data. Inset shows a schematic of the sample with respective electrodes.

5.2.3 2O (Out-of-plane mode of resonator 2)

The frequency of the out-of-plane mode of resonator 2 tunes quadratically with the applied DC voltage U_C at electrode C (see Fig. 5.2). Applying an additional DC bias U_A to electrode A changes the eigenfrequency and tuning behavior of the mode. Figure 5.8 shows the eigenfrequency of mode 2O for a DC voltage of $U_C = 0\,\mathrm{V}$ in dependence of U_A.

The frequency shows a quadratic tuning with U_A and can be varied in a range of about 100 kHz. A quadratic fit (red line) gives the quadratic tuning parameter $c_t = 49\,\mathrm{Hz/V^2}$

$$\begin{aligned} \omega_{2O}(U_A) &= \omega^*_{20} + 2\pi b U_A + 2\pi c_t U_A^2 \\ \omega_{2O}(U_A) &= 2\pi \cdot 5.249 \cdot 10^6\,\mathrm{Hz} - 2\pi \cdot 390\,\frac{\mathrm{Hz}}{\mathrm{V}} \cdot U_A + 2\pi \cdot 49\,\frac{\mathrm{Hz}}{\mathrm{V^2}} \cdot U_A^2. \end{aligned} \tag{5.13}$$

Mode 2O was not accessible for voltages between $U_A = 21\,\mathrm{V}$ and $24\,\mathrm{V}$, as the signal was below noise level.
For DC voltages U_A in the range of $-25\,\mathrm{V}$ to $-13\,\mathrm{V}$ and $25\,\mathrm{V}$ to $30\,\mathrm{V}$, the 1I and 2O mode become resonant, showing an interstring avoided crossing. Therefore, these data-sets are not considered here. However, this is clear evidence, that the additional DC bias U_A allows for tuning modes in and out of resonance by adjusting the applied voltage.
Besides tuning the frequency of mode 2O, U_A also allows for controlling the U_C tuning strength of the mode.

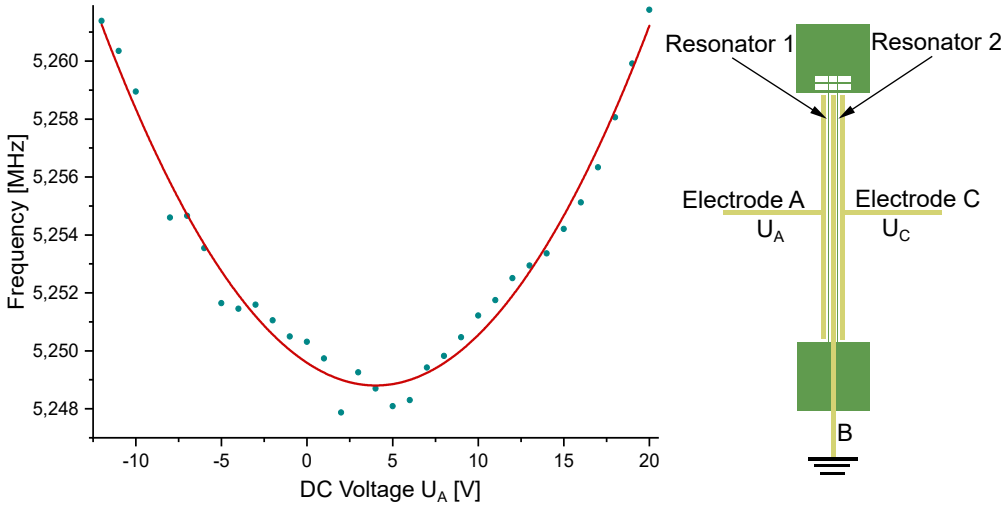

Figure 5.8: Extracted eigenfrequencies of mode 2O at a DC voltage of $U_C = 0\,\mathrm{V}$ (applied to electrode C) for different voltages U_A between $-12\,\mathrm{V}$ and $20\,\mathrm{V}$ (applied to electrode A) depending quadratically on U_A. The frequency can be shifted by more than 100 kHz. Blue dots are measured data points, red curve is a quadratic fit to the data. Inset shows a schematic of the sample with respective electrodes.

The quadratic U_C tuning coefficients c_{2O} were extracted and plotted as a function of U_A (see Fig. 5.9).

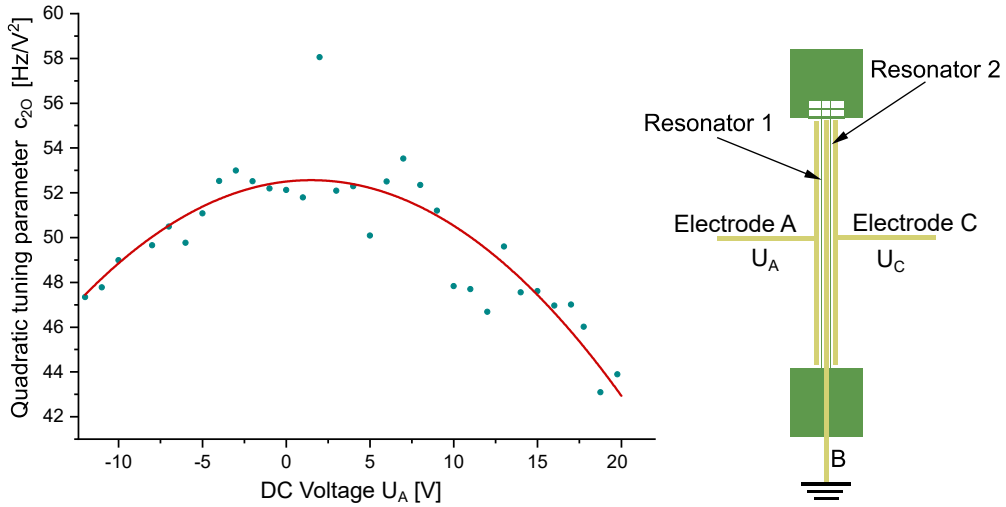

Figure 5.9: Extracted quadratic U_C tuning factor c_{2O} of mode 2O as a function of U_A (applied to electrode A) showing a quadratic dependence on U_A in turn. Blue dots are measured data points and the red curve is a quadratic fit to the data. Inset shows a schematic of the sample with respective electrodes.

We find a quadratic dependence of the U_C tuning parabolas on U_A, but instead of a stiffening (that is an increased bending of the U_C tuning parabola) with increased U_A -like it was the case for the 1O mode- a change in U_A leads to a softening (decreased bending of the U_C tuning parabola) of the U_c tuning parabolas of mode 2O. By applying a quadratic fit to the data we obtain the quadratic softening coefficient ξ_{2O}

$$c_{2O}(U_A) = c_{2O}(U_A = 0) + \xi_{2O} U_A^2 \tag{5.14}$$

$$c_{2O}(U_A) = 52.50 \frac{\text{Hz}}{\text{V}^2} - 0.0281 \frac{\text{Hz}}{\text{V}^4} \cdot U_A^2. \tag{5.15}$$

The quadratic softening parameter $\xi_{2O} = -0.0281\,\text{Hz/V}^4$ is of the same order as the stiffening parameter $\xi_{1O} = 0.0287\,\text{Hz/V}^4$ of mode 1O, that is the U_C tuning of mode 1O is increased in the same ways, as the U_C tuning of mode 2O is decreased, when U_A is changed.
Besides the frequency tuning and a U_A dependent softening, mode 2O shows a linear shift of the U_C tuning parabolas vertexes $U_{2O,0}$, as can be seen in Fig. 5.10.

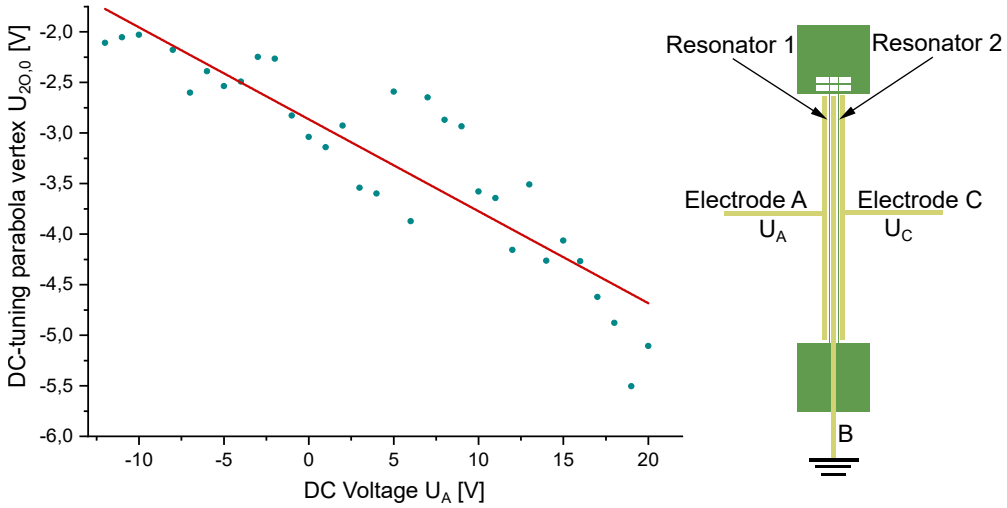

Figure 5.10: U_C tuning parabola vertex ($U_{2O,0}$) of mode 2O as a function of U_A, showing a linear dependence. Blue dots are measured data points and the red curve is a linear fit to the data. Inset shows a schematic of the sample with respective electrodes.

In fact, the U_C tuning parabola shifts with about $-0.09\,\text{V/V}$, as the linear plot (red line) to the data reveals

$$U_{2O,0}(U_A) = -2.864\,\text{V} - 0.09049 \frac{\text{V}}{\text{V}} \cdot U_A. \tag{5.16}$$

5.2.4 2I (In-plane mode of resonator 2)

The last of the four modes, the 2I mode, shows a quadratic frequency tuning with the applied DC voltage U_C at electrode C (see Fig. 5.2), just as we expect it from Eq. (3.3). The presence

of a DC bias U_A on electrode A leads to an additional frequency shift. In Fig. 5.11 the extracted eigenfrequency of mode 2I is plotted as a function of the U_A. The eigenfrequencies were extracted from the U_C tuning spectra at a DC voltage of $U_C = 0\,\mathrm{V}$.

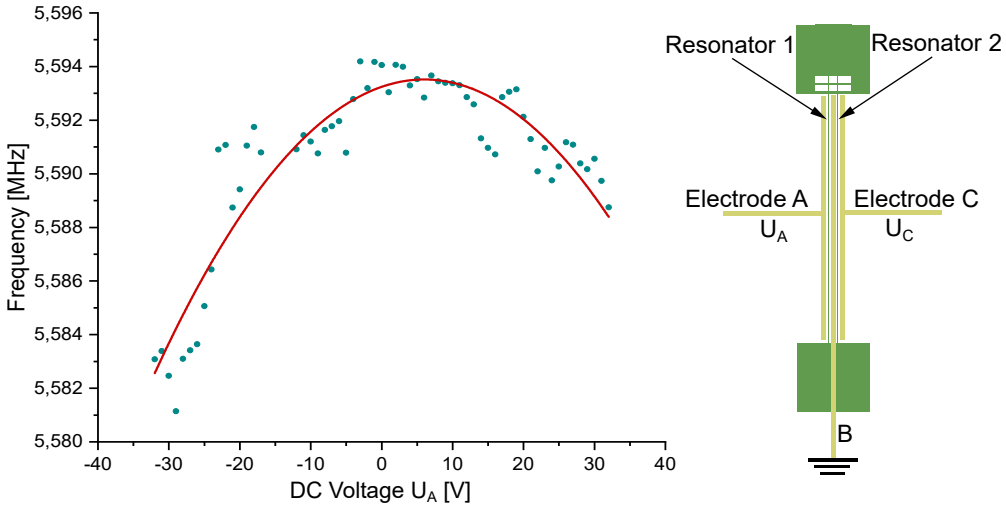

Figure 5.11: Extracted eigenfrequencies of mode 2I at a DC bias of $U_C = 0\,\mathrm{V}$ (applied to electrode C) for different U_A between $-32\,\mathrm{V}$ and $-35\,\mathrm{V}$ (applied to electrode A) show a quadratic dependence on U_A. Blue dots are measured data points, red curve is a quadratic fit to the data. Inset shows a schematic of the sample with respective electrodes.

Figure 5.11 shows the in-plane tuning parabola with U_A and the red line shows a polynomial fit to the data, which gives us the quadratic tuning strength of mode 2I with U_A

$$\begin{aligned} \omega_{2I}(U_A) &= \omega_{2I}^{*} + 2\pi b U_A + 2\pi c_t U_A^2 \\ \omega_{2I}(U_A) &= 2\pi \cdot 5.593 \cdot 10^6\,\mathrm{Hz} + 2\pi \cdot 91.155\,\frac{\mathrm{Hz}}{\mathrm{V}} \cdot U_A - 7.585\pi \cdot 49\,\frac{\mathrm{Hz}}{\mathrm{V}^2} \cdot U_A^2. \end{aligned} \quad (5.17)$$

The quadratic tuning coefficient $c_t = -7.585\,\mathrm{Hz/V^2}$ shows, that mode 2I tunes rather weak with U_A. In fact, the tuning strength of mode 2I is approximately one order of magnitude lower, than the tuning strengths of all other modes. In addition, we can not find a U_A dependent stiffening, or softening of the mode: the U_C tuning strength of mode 2I fluctuates between $-103\,\mathrm{Hz/V^2}$ and $-110\,\mathrm{Hz/V^2}$ without showing any tendencies. But just like for mode 2O, the vertex of the U_C tuning parabola shifts with the applied additional DC bias U_A. In Fig. 5.12 the vertex $U_{2I,0}$ of the 2I U_C tuning parabolas is shown as a function of U_A.

The vertex of the tuning parabolas shows an unsteady, but still linear dependence on U_A and a linear fit (red line) allows for obtaining the strength of the vertex shift

$$U_{2I,0}(U_A) = -0.3975\,\mathrm{V} - 0.105\,\frac{\mathrm{V}}{\mathrm{V}} \cdot U_A. \quad (5.18)$$

Hence we find, that the U_C tuning parabola vertexes of mode 2I and 2O, both get shifted toward negative voltages for increasing positive U_A. For increasing negative U_A, the vertexes of booth

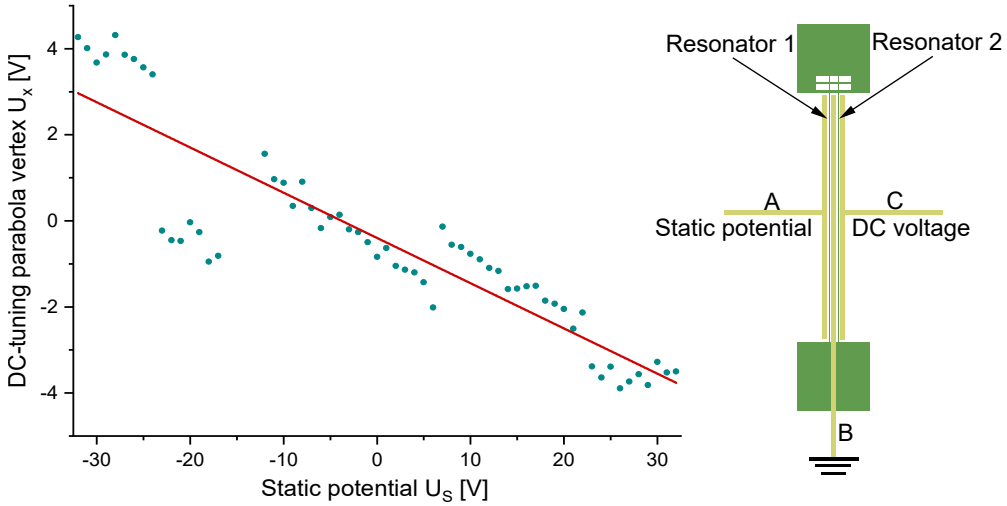

Figure 5.12: 2I U_C tuning parabola vertex ($U_{2I,0}$) as a function of U_A, showing a linear dependence. Blue dots are measured data points and the red curve is a linear fit to the data. Inset shows a schematic of the sample with respective electrodes.

modes get shifted towards positive voltages, whereas mode 2I shifts slightly stronger than mode 2O. For mode 1O and 1I in contrary, we can not find this shift of the U_C tuning vertex.
Overall the frequency tuning strengths of the modes with U_C and the additionally applied U_A differ depending on whether it is an in-plane, or an out-of-plane mode. For example, mode 2I couples twice as strongly to U_C as mode 2O, whereas mode 2O couples 7-times stronger to U_A than mode 2I. For mode 1I we find that its coupling strength to U_A is more than twice as big as the coupling strength of mode 1O. But we find a quadratic tuning of mode 1O with the DC voltage U_C and a linear tuning of mode 1I. This once again emphasizes the significance of the proportionality factors β and χ in Eq. (5.9), since they contain information of the exact electric field seen by the modes. In principle it is possible to simulate these proportionality factors if the exact geometry of the resonators and the surrounding electrodes. On the other hand, they may be obtained by precise studies of the DC tuning behavior of the modes.

5.3 Inverse electrode configuration

If the electric field constellation of electrode A and C is reversed, (the DC bias U_A is applied at electrode A and an additional DC U_C bias at electrode C), we find a symmetric reversed behavior of the modes. Figure 5.13 shows the U_A voltage sweeps for an additional DC bias U_C of -32 V (left) and 31 V (right) applied to electrode C. In comparison with Fig. 5.2, we now find that mode 2I tunes linearly with U_A, while in Fig. 5.2 the 1I mode tunes linearly. We also find that the U_A tuning strength and direction of mode 2O changes with U_C. The left picture of Fig. 5.13 ($U_C = -32$ V) shows two interstring avoided crossings between mode 1I and 2I at voltages of about $U_A = -14$ V and $U_A = 7$ V. In the right picture of Fig. 5.13 (U_C =31 V) an interstring avoided crossing of modes 1I and 2O is apparent. As the linewidths of these modes

are in the range of 200 Hz to 600 Hz (depending on the DC voltage and the static potential) it is possible, that the linewidths are wider than the coupling strength, and hence an avoided crossing of the modes can not be clearly resolved.

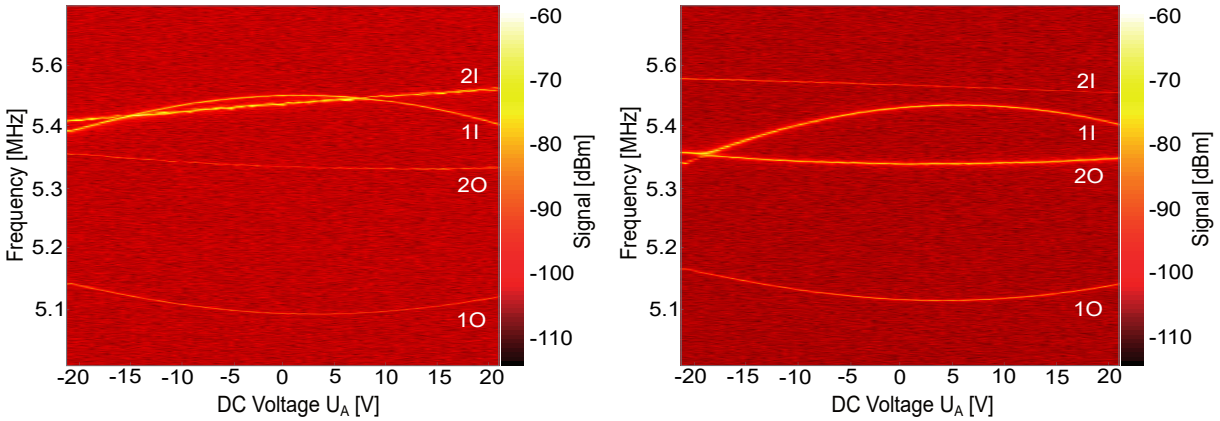

Figure 5.13: U_A voltage sweeps of resonator 1 for two different DC voltages U_C applied to electrode C. The left spectrum was obtained for $U_C = -32\,\mathrm{V}$, the right spectrum for $U_C = 31\,\mathrm{V}$. Left spectrum shows two interstring avoided crossing of modes 2I and 1I. On the right spectrum an interstring avoided crossing between mode 1I and 2O can be seen. Mode 2I shows a linear U_A tuning and changes the tuning direction with respect to U_C.

Just like for the above case, we will quantitatively analyze the influence of the additional DC bias U_C on the eigenfrequencies, as well as on the U_A tuning behavior of all four modes.

5.3.1 1O (Out-of-plane mode of resonator 1)

For mode 1O we find a quadratic eigenfrequency tuning (see Fig. 5.14) with respect to U_C with a tuning strength of $c_t = 37\,\mathrm{Hz/V^2}$, which can be obtained by performing a quadratic fit (red line) of the form

$$\begin{aligned} \omega_{1O}(U_C) &= \omega_{10}^* + 2\pi b U_C + 2\pi c_t U_C^2 \\ \omega_{1O}(U_C) &= 2\pi \cdot 5.065 \cdot 10^6\,\mathrm{Hz} - 2\pi \cdot 374\,\frac{\mathrm{Hz}}{\mathrm{V}} \cdot U_C + 2\pi \cdot 37\,\frac{\mathrm{Hz}}{\mathrm{V}^2} \cdot U_C^2 \end{aligned} \tag{5.19}$$

to the extracted eigenfrequencies (blue dots) at a DC voltage of $U_A = 0\,\mathrm{V}$ for different U_C from $-32\,\mathrm{V}$ to $32\,\mathrm{V}$. Here the data sets from $-8\,\mathrm{V}$ to $5\,\mathrm{V}$ were excluded, as for these static potentials avoided crossings appear, and thus the pure in-and out-of-plane modes can no longer be observed.
The inset of Fig. 5.14 shows the quadratic U_A tuning parameter c_{1O} as a function of U_C. The quadratic fit (red line, inset)

$$c_{1O}(U_C) = c_{1O}(U_C = 0) + \xi_{1O} U_C^2 \tag{5.20}$$

$$c_{1O}(U_C) = 58.43\,\frac{\mathrm{Hz}}{\mathrm{V}^2} 0.0326\,\frac{\mathrm{Hz}}{\mathrm{V}^4} \cdot U_C^2 \tag{5.21}$$

to the data (blue dots, inset) yields the quadratic stiffening coefficient $\xi_{1O} = 0.0326\,\mathrm{Hz/V^4}$, corresponding to an effective gain of the U_A tuning strength of over 42 % from 58 $\mathrm{Hz/V^2}$ to over 98 $\mathrm{Hz/V^2}$.

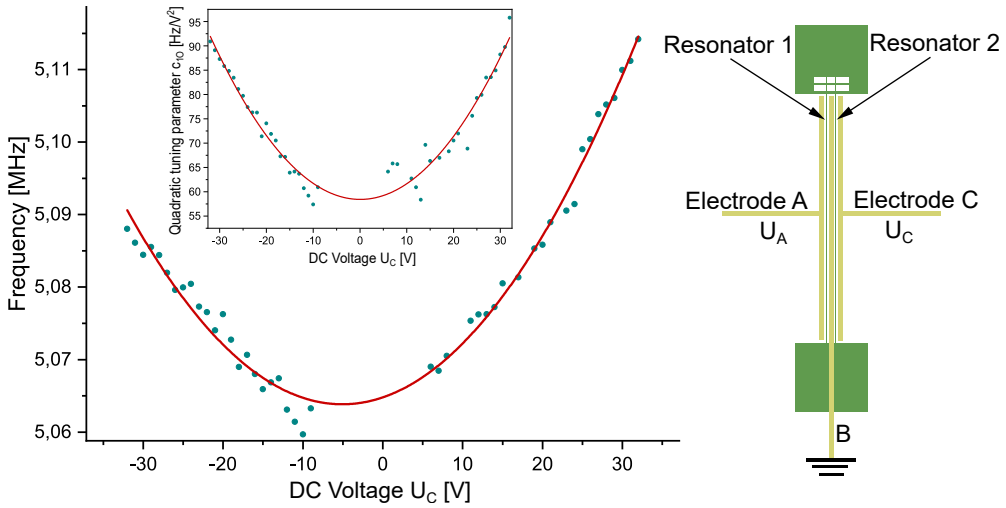

Figure 5.14: Eigenfrequency of mode 1O as a function of the additional DC bias U_C. The eigenfrequencies were extracted from the power spectra at a DC voltage of $U_A = 0\,\mathrm{V}$ (applied to electrode A) for different voltages U_C between $-32\,\mathrm{V}$ and $32\,\mathrm{V}$ (applied to electrode C). Inset shows extracted quadratic U_A tuning factor c_{1O} of mode 1O as a function of U_C, showing a quadratic dependence. Blue dots are measured data points and the red curves are quadratic fits to the data. Right side shows a schematic of the sample with respective electrodes.

5.3.2 1I (In-plane mode of resonator 1)

The frequency of mode 1I tunes quadratic with U_A (see Fig. 5.13), but shows a linear dependence on U_C as shown in Fig. 5.15, where the extracted eigenfrequencies (at $U_A = 0\,\mathrm{V}$) and the respective linear fit (red line) are shown

$$\begin{aligned} \omega_{1I}(U_C) &= \omega_{1I}^{*} + 2\pi b U_C \\ \omega_{1I}(U_C) &= 2\pi \cdot 5.442 \cdot 10^6\,\mathrm{Hz} - 2\pi \cdot 2.98 \cdot 10^4\,\frac{\mathrm{Hz}}{\mathrm{V}} \cdot U_C. \end{aligned} \tag{5.22}$$

The fit yields a linear tuning parameter b $= -2.98\,\mathrm{kHz/V}$. Similar to the case, when the DC voltage U_C is applied to electrode C and the additional DC bias U_A to electrode A (see chapter 5.2) mode 1I is coupled linearly to the electrical potential applied to electrode C (U_C) and in both cases the tuning constant is in the range of kHz (see Fig. 5.6).
Besides this fact, we also find that the additional DC bias U_C on electrode C shifts the vertex of the U_A tuning parabola of mode 1I. The inset of Fig. 5.15 shows the linear dependence of

the vertex $U_{1I,0}$ on U_C along with a linear fit, which gives the strength of this vertex shift as 0.04 V/V

$$U_{1I,0}(U_C) \quad = \quad -2.22\,\mathrm{V} + 0.04\,\frac{\mathrm{V}}{\mathrm{V}} \cdot U_C. \tag{5.23}$$

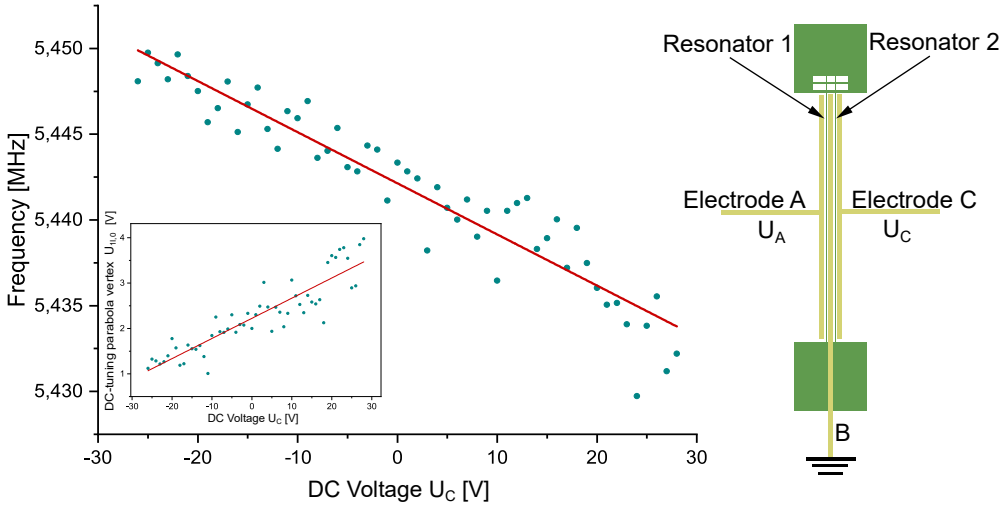

Figure 5.15: Eigenfrequency of mode 1I as a function of U_C (blue dots: data points, red line: linear fit). The eigenfrequencies were extracted from the power 0spectra at a DC voltage of $U_A = 0\,\mathrm{V}$ (applied to electrode A) for different U_C between $-27\,\mathrm{V}$ and 27 V (applied to electrode C). Inset shows the shift of the U_A tuning parabola vertex depending linearly on U_C (blue dots: data points, red line: linear fit). Right side shows a schematic of the sample with respective electrodes.

For the evaluation of mode 1I, only power spectra for DC voltages between $U_C = -27\,\mathrm{V}$ and $U_C = 27\,\mathrm{V}$ were taken into account, as for U_C higher (lower) than 27 V ($-27\,\mathrm{V}$) an avoided crossing between modes 1I and 2O, as well as avoided crossings between modes 1I and 2I were observed and it is therefore not possible to observe the pure 1I mode.

5.3.3 2O (Out-of-plane mode of resonator 2)

Mode 2O tunes quadratically with U_A, and as Fig. 5.16 shows, also with the additional DC bias U_C. A quadratic fit (red line) to the data (blue dots) allows for determination of the tuning strength of mode 2O with U_C applied to electrode C:

$$\begin{aligned} \omega_{2O}(U_C) &= \omega_{20}^* + 2\pi b U_C + 2\pi c_t U_C^2 \\ \omega_{2O}(U_C) &= 2\pi \cdot 5.252 \cdot 10^6\,\mathrm{Hz} + 2\pi \cdot 237\,\frac{\mathrm{Hz}}{\mathrm{V}} \cdot U_C + 2\pi 77\,\frac{\mathrm{Hz}}{\mathrm{V}^2} \cdot U_C^2. \end{aligned} \tag{5.24}$$

Thus the eigenfrequency of 2O tunes with $c_t = 77\,\mathrm{Hz/V^2}$.

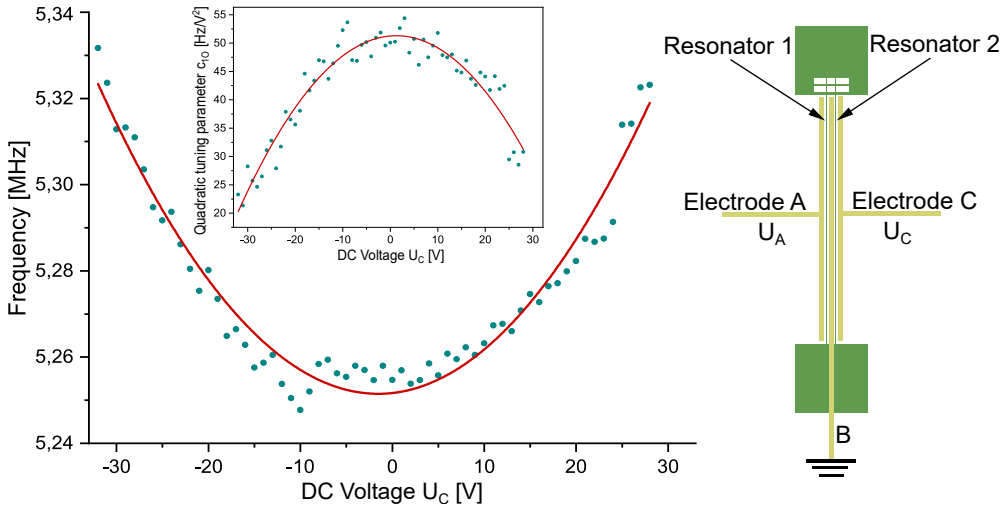

Figure 5.16: Quadratic tuning of the eigenfrequency of mode 2O with U_C (blue dots: data points, red line: quadratic fit). The eigenfrequencies were extracted from the power-spectra at a DC voltage of U_A =0 V (applied to electrode A) for different U_C between -32 V and 32 V (applied to electrode C). The inset shows the quadratic U_A tuning strength c_{2O} as a function of U_C (blue dots: data points, red line: quadratic fit). Right side shows a schematic of the sample with respective electrodes.

On the inset of Fig. 5.16, the U_A tuning strength of mode 2O is shown a function of U_C, revealing a quadratic softening of the U_A tuning strength. The quadratic fit (red line in inset) to the data

$$c_{2O}(U_C) = c_{2O}(U_C = 0) + \xi_{2O} U_C^2 \tag{5.25}$$

$$c_{2O}(U_C) = -0.07\,\frac{\text{Hz}}{\text{V}^2} - 0.02\,\frac{\text{Hz}}{\text{V}^4} \cdot U_C^2 \tag{5.26}$$

yields the quadratic softening parameter $\xi_{2O} = -0.02\,\text{Hz/V}^4$. The adjustment of the additional DC bias U_C enables the enhancement of the U_A tuning strength from 21 Hz/V^2 to more than 53 Hz/V^2.
Furthermore, a change in U_C leads to a shift of the U_C tuning parabola vertex $U_{2O,0}$ of mode 2O, as can be seen in Fig. 5.17. The vertex depends exponentially on U_C and can be shifted from over 14 V to 0.6 V.
An exponential fit (red line) of the form

$$U_{2O,0} = 0.66^{(U_C/11.1)} + 2.16\,V \tag{5.27}$$

reproduces the shift of the U_A tuning parabola vertex very well, showing that for voltages U_C higher than 0 V the vertex tends to scatter at around 2 V (see Fig. 5.17).

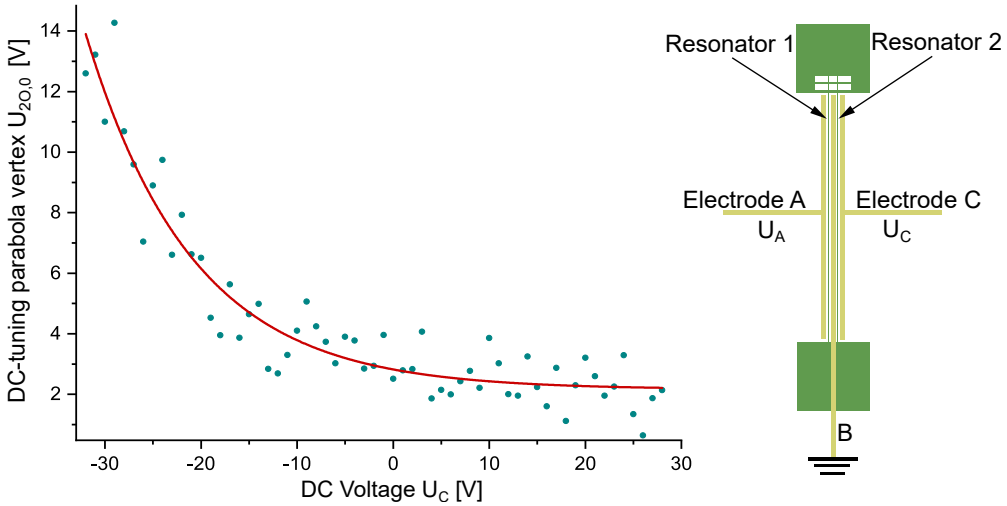

Figure 5.17: Vertex of the 2O U_A tuning parabolas shifting with U_C (blue dots: data points, red line: exponential fit). For DC voltages $U_C > 0$ V, the vertex scatters around 2 V. Right side shows a schematic of the sample with respective electrodes.

5.3.4 2I (In-plane mode of resonator 2)

Mode 2I tunes quadratic with U_C applied to electrode C as can be seen in Fig. 5.15. Fitting a quadratic function (red line) to the data (blue dots)

$$\begin{aligned} \omega_{2I}(U_C) &= \omega_{2I}^* + 2\pi b U_C + 2\pi c_t U_C^2 \\ \omega_{2I}(U_C) &= 2\pi \cdot 5.568 \cdot 10^6\,\text{Hz} + 2\pi \cdot 719\,\frac{\text{Hz}}{\text{V}} \cdot U_C - 2\pi \cdot 128\,\frac{\text{Hz}}{\text{V}^2} \cdot U_C^2 \end{aligned} \tag{5.28}$$

yields a quadratic U_C tuning strength of the eigenfrequency of mode 2I of $c_t = -128\,\text{Hz/V}^2$. For mode 2I we find that the eigenfrequency tunes linear with U_A applied to electrode A (see Fig. 5.13). Similar to the case of mode 1I in chapter 5.2.2, when a DC voltage U_C is applied to electrode C and an additional DC bias U_A to electrode A, the linear U_A tuning strength of mode 2I can be varied by adjusting U_C. As the inset of Fig. 5.15 shows, the linear U_A tuning strength b can be changed from over 1.3 kHz/V to -0.64 kHz/V, and hence even the direction of the U_A tuning of mode 2I can be reversed.
Furthermore, the U_A tuning strength depends linearly on U_C and by applying a linear fit (red line in inset) to the data (blue dots in inset), the coupling strength of the linear tuning factor b to the static potential can be obtained

$$b_{2I}(U_C) = -2\pi \cdot 25.3\,\frac{\text{Hz}}{\text{V}^2} \cdot U_C + 2\pi \cdot 234\,\frac{\text{Hz}}{\text{V}}, \tag{5.29}$$

showing that the linear U_A tuning of mode 2I can be changed by $-25.3\,\text{Hz/V}^2$ by varying U_C. Taking a look at the overall influence of the additional DC bias on the modes, we find that it enables not only additional frequency tuning of the modes, but also allows for adjustment of the DC-tuning strength by up to 180% of the initial tuning strength. Therefore, the utilization of the

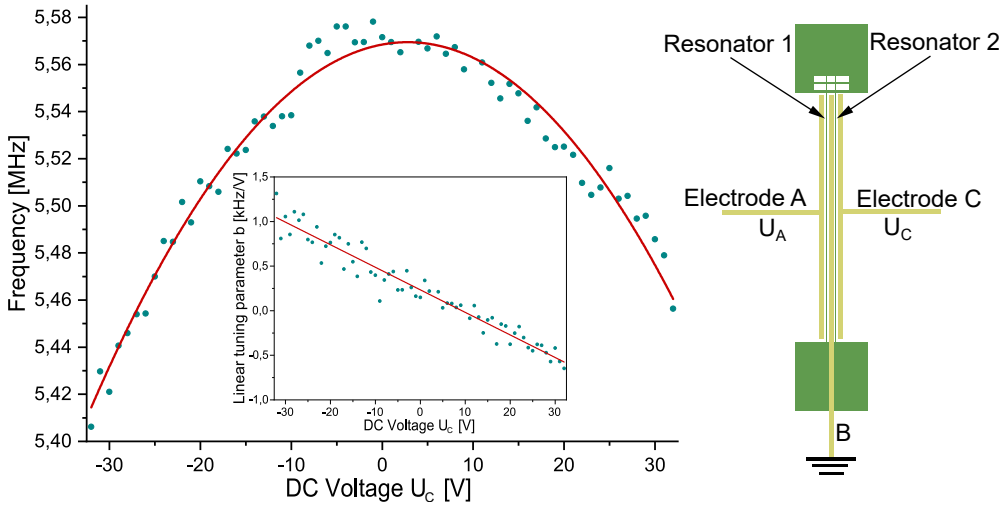

Figure 5.18: Extracted eigenfrequencies of mode 1O as a function of U_C (blue dots: data points, red line: quadratic fit). The eigenfrequencies were extracted from the power-spectra at a DC voltage of $U_A = 0\,\mathrm{V}$ (applied to electrode A) for different U_C between $-32\,\mathrm{V}$ and $32\,\mathrm{V}$ (applied to electrode C). The inset shows the linear U_A tuning strength b changing linearly with U_C (blue dots: data points, red line: linear fit). Right side shows a schematic of the sample with respective electrodes.

3-electrode (or more) geometry opens up an additional tool box for arbitrary mode adjustment, which is necessary for the realization of whole resonator arrays. It is also beneficial for meeting the requirements of coupling the mechanical modes of the resonators (or arrays of resonators) to other degrees of freedom like optical modes[64] or cold atoms.[65,66]
However, before the system can be integrated into opto-mechanical circuits, or other applications it is essential to examine all its mechanical aspects including nonlinear behavior.
All measurements presented in this chapter were acquired using the laser interferometer. As mentioned in chapter 3.3.1, the laser adds additional heating to the resonators, thus leading to an additional frequency shift of the modes. This also causes slight fluctuations of the eigenfrequencies of the modes. For future experiments, the microwave cavity enhanced readout could be an option to avoid this uncertainty.

Chapter 6

The nonlinear system

As the underlying system consists of high Q resonators, it also offers a broad spectrum of nonlinear effects, like nonlinear mode coupling or even the chaotic regime (for some examples see Appendix D). In a first attempt to investigate the system in the nonlinear regime we take a closer look at the effect that a change in amplitude of one mode causes on the eigenfrequencies of the respective other modes, revealing that the system shows nonlinear dispersive coupling. Furthermore, this coupling depends in a nontrivial way on the polarization of the individual modes.

6.1 Pre-characterization

Before measurements on the nonlinear mechanics of the system can be done, it is necessary to characterize the sample, e.g. the mode evolution as a function of the DC voltage and the linear coupling strengths g_{ij} between the modes. The system investigated here is based on the 2-electrode geometry (see section 3.1.1), with one resonator being flanked by two adjacent gold electrodes for dielectric actuation and detection. Additionally, a microwave cavity is inductively coupled to this resonator for readout. In order to keep deviations and measurement-instabilities as low as possible we desisted from using the interferometric laser readout, as this adds heat to the system, which in turn can result in an additional frequency-shift, that fluctuates with e.g. the room temperature. However, the microwave cavity is coupled only to one resonator, and hence the non-directly driven resonator is available for detection only in the vicinity of an avoided crossing between modes of both resonators. Figure 6.1 shows the power spectrum of the system measured with the microwave cavity. Here mode 1 corresponds to the mode with the lowest frequency, mode 2 to the medium frequency and mode 3 to the highest frequency. This nomenclature is independent of the mode polarization and holds for the whole voltage sweep. Mode 4, which has an even higher frequency than mode 3, can be assigned to the in-plane mode of the non-directly driven resonator. It can not be resolved by the detection technique, since the microwave cavity enhanced readout is less sensitive on in-plane modes and additionally mode 4 and does not participate in any avoided crossing. Thus, it will not be considered any further.

The assignment of the other modes to an in-plane or out-of-plane polarization is given in chapter 6.3 and is not of interest for now.

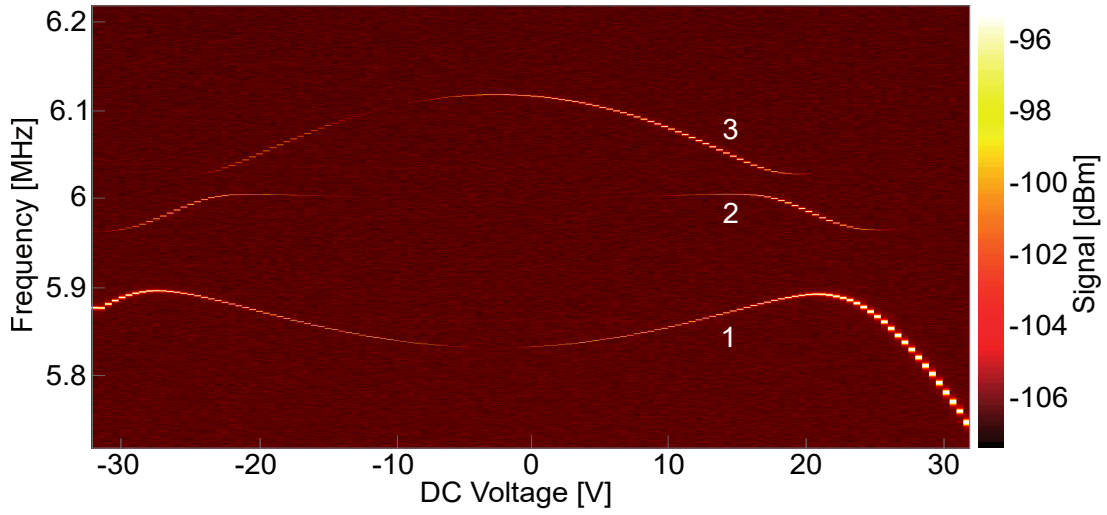

Figure 6.1: Frequency response to a DC voltage sweep from -32 to 32 V of the directly driven resonator. Throughout the voltage sweep, mode 1 corresponds to the mode with the lowest eigenfrequency, mode 2 to the mode with intermediate frequency and mode 3 corresponds to the highest frequency, independent of being an in- or out-of plane mode.

Also mode 2 can -as explained above- only be accessed near an avoided crossing, where the modes already start to hybridize, because it also is a mode of the non-directly driven resonator. The frequency response shows two multi-mode avoided crossings between -30 V and -20 V and between 15 V and 25 V, respectively. In both cases the avoided crossings between modes 2 and 3 and 2 and 1 overlap with an avoided crossing between mode 1 and 3 (for detailed information on 3-mode resonance see chapter 4.2). The genetic fitting algorithm described in chapter 4.1 was performed, yielding coupling strengths of $g_{12}/2\pi = 101.5$ kHz between mode 1 and 2 at a voltage of about 23 V, $g_{13}/2\pi = 59.41$ kHz between mode 1 and 3 at a voltage of about 20 V and $g_{23}/2\pi = 43.21$ kHz between mode 2 and 3 at 18 V. For the avoided crossings at negative voltages, we get the same values, respectively.

6.2 Nonlinear dispersive mode coupling

Now that the frequency evolution of the three linearly coupled modes is known, the voltage can be fixed to access either the unperturbed modes, or any stage of the 3-mode resonance, and thus the hybridized modes. Either of the modes can be actuated by applying a fixed sinusoidal drive tone near the eigenfrequency $\omega_d \approx \omega_{i0}$ of the respective mode. Note, that the resonator which is not in-between the gold electrodes can only be driven indirectly. If the drive power of the sinusoidal drive tone is increased, the amplitude of the driven resonator increases. In Fig. 6.2 such a drive power sweep for mode 2 at a drive frequency $\omega_d/2\pi = 5.9595$ MHz is shown. The

voltage was fixed at 6 V and the drive power was varied from −10 dBm to 20 dBm.
However, the microwave cavity enhanced readout technique adds dielectric damping on the resonators and it is necessary to add a white noise signal to the drive tone for some DC voltages. This wide-band white noise acts as an effective heating of the resonators and has to be adjusted carefully, so that the non-driven modes are well in the linear response regime.

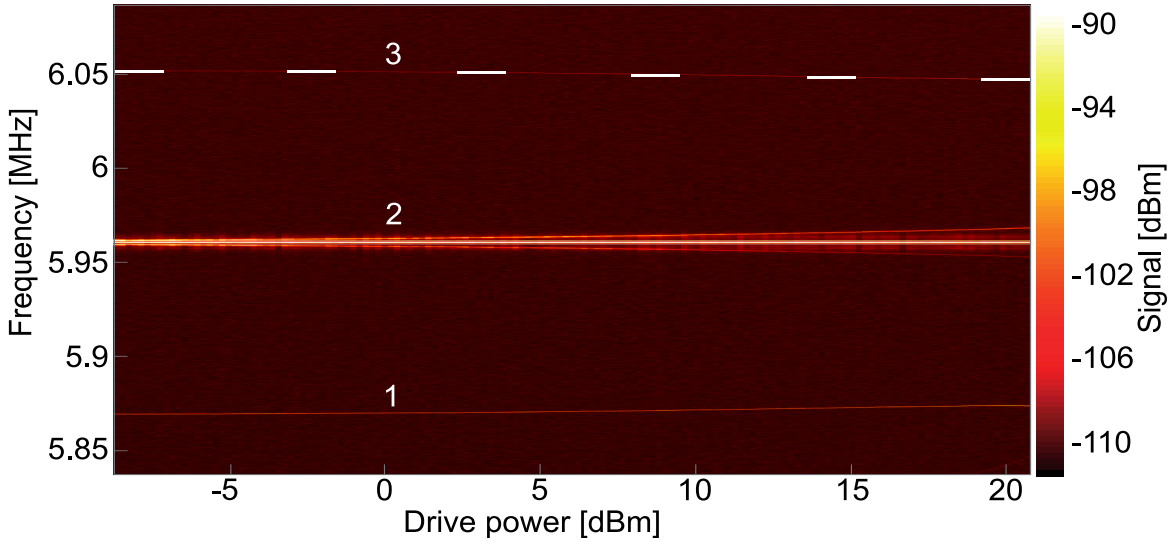

Figure 6.2: Drive power sweep of mode 2 at 6 V for a fixed drive frequency $\omega_d/2\pi = 5.9595$ MHz. The drive power was varied from −10 dBm to 20 dBm. As the drive power, and hence the amplitude of mode 2 is increased, modes 1 and 3 experience a shift in eigenfrequency. Additionally two satellite peaks around ω_d arise, caused by thermal noise. The white dashed line is a guide to the eye for mode 3.

Figure 6.2 shows that an increase in drive power, and thus an increase in amplitude of mode 2 results in a frequency-shift of modes 1 and 3: both frequencies get "pulled" towards mode 2, showing that the change in amplitude of one mode affects the eigenfrequencies of the others. This is a clear confirmation of nonlinear dispersive mode coupling. The white dashed line at mode 3 is a guide to the eye.
Besides the frequency shift of the respective coupled modes, two satellite peaks with different intesity appear besides the drive frequency ω_d. These sidebands are caused by thermal fluctuations.[67,68] The spectrum was manually brightened up by cutting off the maximum signal at −95 dBm in order to make modes 1 and 3 visible.
The area between the driving-peak at ω_{20} and the satellites appears brighter than the regular background noise floor in Fig. 6.2. Here we find an enhancement of the noise floor between the driven mode 2 and the respective satellite peaks. As modes 1 and 3 are not driven, the spectrum in Fig. 6.2 shows the thermal motion of these modes.
These power sweep measurements can be performed for any of the three modes, and for different DC voltages, showing similar behavior, provided that the modes can be resolved by the measurement technique. For very high drive powers (> 15 dBm) the system can enter chaos as

shown in appendix D and thereby making measurements on the dispersive coupling challenging. Therefore, it is reasonable to use a kind of measurement that offers less instability and avoids chaotic states.
The dispersive mode coupling not only manifests itself in the drive power sweep, but can also be detected in a drive-frequency sweep, where the drive power can be fixed in a range where the system does not approach chaos. For these measurements the voltage is again fixed. Now the drive frequency ω_d is varied such that the drive starts way off resonance $\omega_d << \omega_{i0}$ and then slowly is increased until $\omega_d >> \omega_{i0}$. Figure 6.3 shows an exemplary frequency sweep around mode 2 for a fixed DC voltage of 15 V and a drive power of -20 dBm. The white line is a guide to the eye for the drive frequency ω_d as this peak is very narrow. The maximum signal was cut-off at -85 dBm to enhance the visibility of modes 1, 2 and 3 in the spectrum.

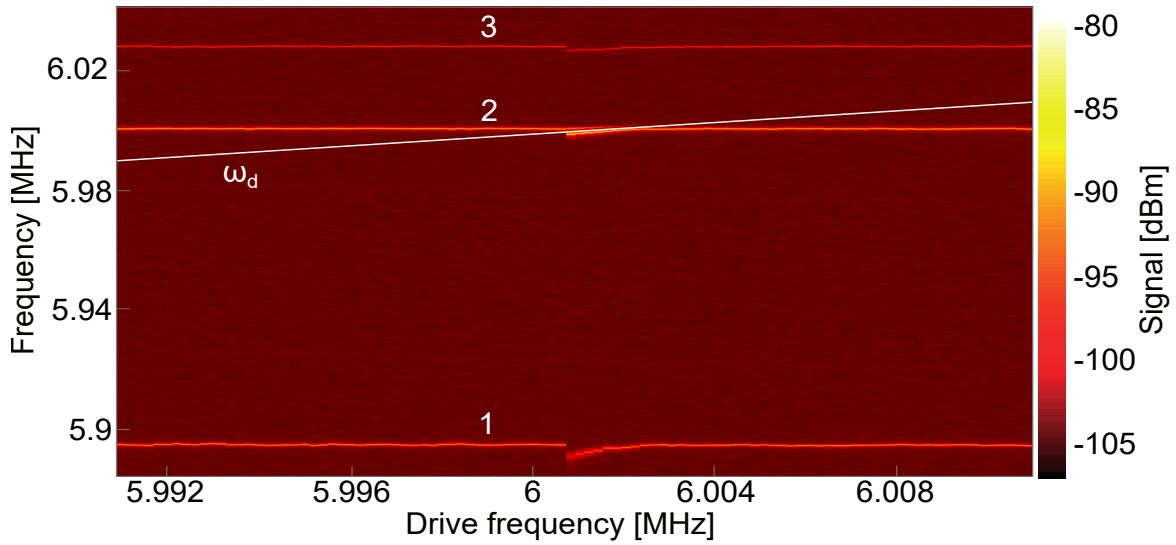

Figure 6.3: Frequency sweep of mode 2 at 15 V for a fixed drive power of -20 dBm. The drive frequency ω_d was varied from 5.99 MHz to 6.01 MHz. As the drive frequency approaches the eigenfrequency of mode 2 ($\omega_{20}/2\pi = 6.001$ MHz), the amplitude of mode 2 is increased, leading to a "jump" in frequency of modes 1 and 3. When ω_d is further increased, modes 1 and 3 return to their original. The white line is a guide to the eye to clarify the drive frequency.

When the drive frequency reaches the eigenfrequency of mode 2, the amplitude of mode 2 increases abruptly, causing a "jump" in frequency of modes 1 and 3. Additionally two satellite peaks arise around mode 2, again being caused by thermal fluctuations. As the drive frequency is further increased and therefore the amplitude of mode 2 is decreased again, modes 1 and 3 approach their original, unperturbed eigenfrequencies.
If the drive frequency is close to the eigenfrequency of the driven mode, the frequency response of this mode transitions from the undriven linear Brownian motion to a nonlinear Duffing resonator. Depending on the sign of the Duffing constant γ_{ii} (see chapter 1.3) of the driven mode, the frequencies of the respective coupled modes either "jump" and then shift back to their eigenfrequencies like shown in Fig. 6.3 (for $\gamma_{ii} < 0$, see chapter 1.3), or they first experience the fre-

quency shift and then "jump" back to their eigenfrequencies (for $\gamma_{ii} > 0$). Figure 6.4 shows the extracted amplitude of mode 2 as function of the drive frequency. For a drive frequency close to the eigenfrequency of mode 2 ($\omega_{20}/2\pi = 6.001\,\text{MHz}$), the amplitude starts to rise and "jumps" to the maximum if the eigenfrequency is reached and then decreases to its initial value, thus showing characteristic behavior of a softening Duffing resonator.

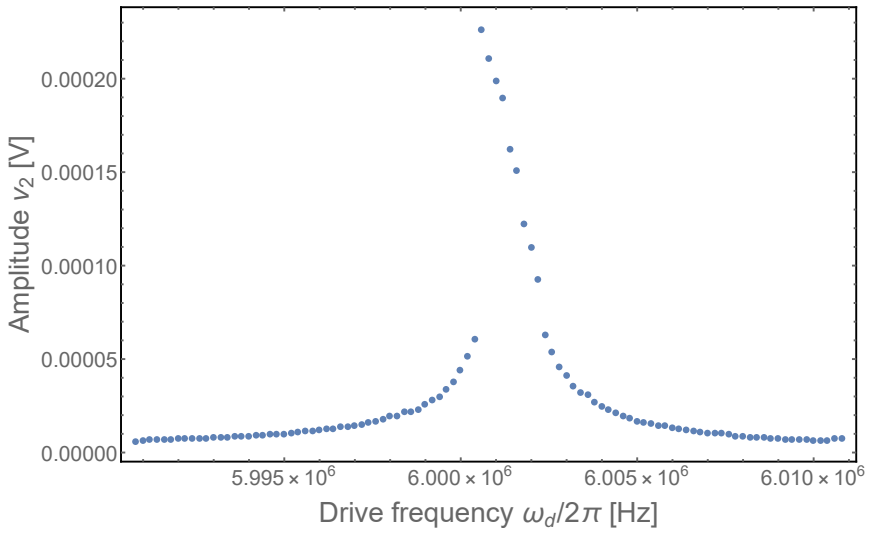

Figure 6.4: Extracted linearized amplitude v_2 of mode 2 as a function of the drive frequency reflecting the Duffing nonlinearity.

In order to obtain the dispersive coupling coefficients γ_{ij}, modes 1 and 3 are extracted from the spectrum of the frequency sweep (Fig. 6.3). In Fig. 6.5 the extracted eigenfrequencies of modes 1 (green dots, left) and 3 (orange dots, right) are presented.

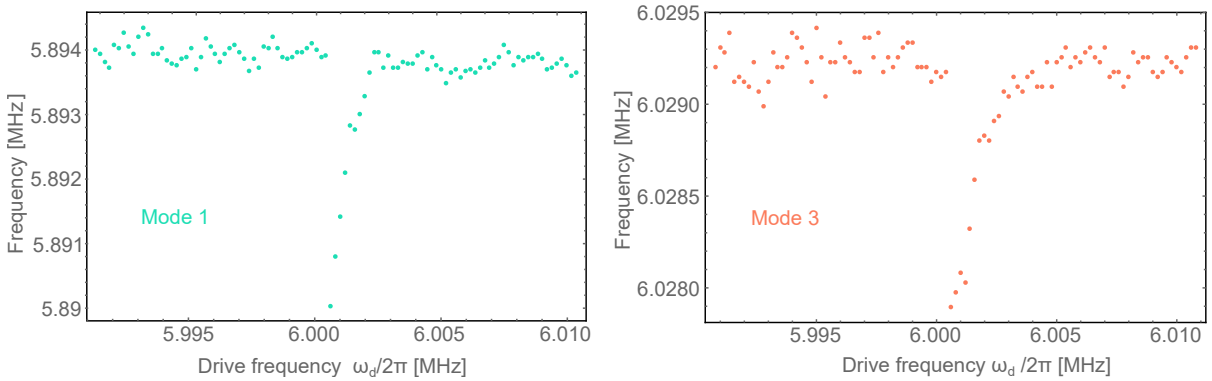

Figure 6.5: Extracted eigenfrequencies of modes 1 (green, left) and 3 (orange, right) as a function of the drive frequency, showing a "jump" when the drive frequency hits the eigenfrequency of mode 2 ($\omega_{20}/2\pi = 6.001\,\text{MHz}$).

The dispersive coupling coefficients γ_{ij} can be obtained by fitting the eigenfrequencies of mode

1 and 3 as a function of the amplitude v_2 of mode 2, which is given in units of volts (see Eq. (1.20)). The equation for the dispersive mode coupling reads

$$\omega_j^{\diamond} = \sqrt{(\omega_{j0})^2 + \gamma_{ij} * v_i^2}, \tag{6.1}$$

where ω_{i0} is the start frequency for the fit (here $i = 2$), precisely, the unperturbed eigenfrequency for the respective given voltage and $\omega_i^{\diamond}$ is the coupling dependent frequency of the respective non-driven mode for one fixed voltage. The coupling coefficient γ_{ij} (here $j = 1, 3$) is a free fit-parameter. This equation can be derived from the equation of motion (Eq. (1.21)), if the linear (strain- and dielectric) coupling is neglected, but the nonlinear interaction from Eq. (1.25) is taken into account.
In Fig. 6.6 the eigenfrequencies $\omega_1^{\diamond}$ of mode 1 (red dots, left) and $\omega_3^{\diamond}$ of mode 3 (red dots, right) as a function of the amplitude of mode 2 is displayed. The blue lines show the respective fits corresponding to Eq. (6.1).

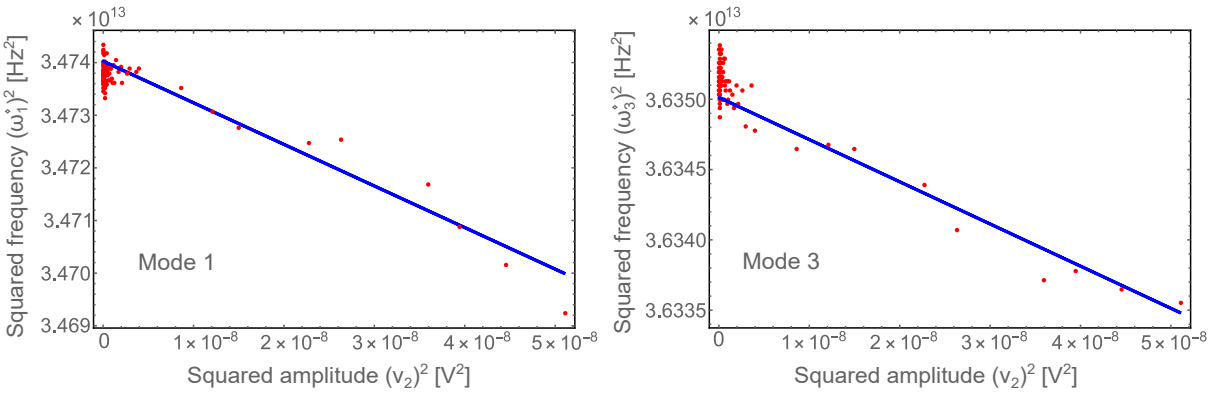

Figure 6.6: Dependence of the eigenfrequency $\omega_1^{\diamond}$ (red dots) of mode 1 (left) and mode 3 (right) on the amplitude v_2 of mode 2. The blue lines depict the fit of Eq. (6.1) to the data yielding a dispersive coupling coefficient of $\gamma_{21} = -3.347 \cdot 10^{19}\text{Hz}^2/\text{V}^2$ and $\gamma_{23} = -1.184 \cdot 10^{19}\text{Hz}^2/\text{V}^2$.

The fits yield dispersive coupling coefficients of $\gamma_{21} = -3.3474 \cdot 10^{19}\text{Hz}^2/\text{V}^2$ between mode 2 and 1, and $\gamma_{23} = -1.184 \cdot 10^{19}\text{Hz}^2/\text{V}^2$ for the coupling between mode 2 and 3. For a more detailed picture of the dispersive mode coupling in this system, the dependence of the dispersive coupling on the mode polarization has to be investigated.

6.3 Polarization dependent coupling and Duffing-constant

As the modes of the system can be tuned in frequency by changing the DC voltage, and hence can be brought in resonance, the polarization of the modes also depends on the DC voltage. When the modes start to hybridize, the polarization of the modes rotates. The DC voltage dependence of the mode polarization is given in Fig. 6.7, where the eigenvectors e_{ij} of the linearly coupled modes are displayed. Each eigenvector consists of three components, as three modes

are coupled and each mode can give a contribution (if hybridized) to every other mode.

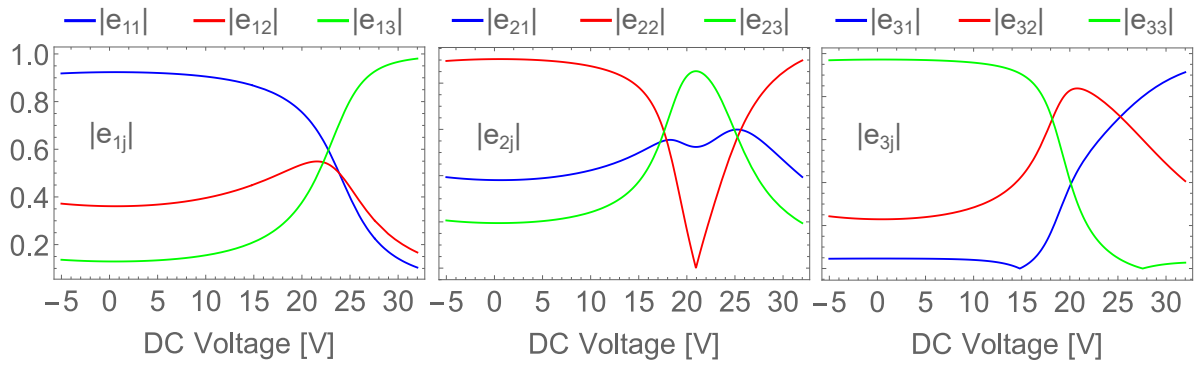

Figure 6.7: Eigenvectors e_{1j} e_{2j} and e_{3j} (from left to right) with normalized length as a function of the DC voltage, plotted for voltages from -5 V to 32 V. The hybridization of the linear coupled modes (compare to Fig. 6.1) can be reconstructed via the individual components of each eigenvector: for voltages between 17 V and 27 V the modes hybridize.

As the behavior of the modes is symmetric for positive and negative voltages (see Fig. 6.1), so is the DC voltage dependence of the eigenvectors. Therefore, the eigenvectors are plotted here for DC voltages from -5 V to 32 V. The individual components of each eigenvector show the contribution of each other resonator. For -5 V eigenvector e_{1j} has a contribution of component e_{11} close to one, from e_{12} near 0.4 and e_{13}, which is below 0.2, meaning that at this voltage, mode 1 is almost not hybridized, and thus can be considered a pure mode. When the modes hybridize (between 17 V and 27 V), the contributions of the participating modes 2 and 3 increase. For voltages higher than 27 V the modes are again dehybridized, only now mode 1 and 3 are interchanged. In particular, mode 1 was defined as the mode with the lowest frequency throughout the whole voltage range. A comparison with Fig. 6.1 shows, that at -5 V mode 1 can be identified as the out-of-plane mode of resonator 1, whereas at 30 V it has transformed into the in-plane mode of resonator 1. The inverse holds for mode 3. For mode 2, which can be identified as the out-of-plane mode of resonator 2 at -5 V, we find that it hybridizes with modes 1 and 3 and finally transitions back into the out-of-plane mode of resonator 2 at 30 V. This classification is based on the DC tuning behavior of the mode branches (for more information see chapter 3.2) and shall only illustrate how the actual mode evolution in Fig. 6.1 can be reconstructed from the eigenvectors e_{ij}. Please note, that for the following evaluation of the DC dependence of the dispersive coupling and the Duffing-coefficient the property of being an in-plane or-out-of-plane mode, or the assignment to a specific resonator is not of interest.
The eigenvectors can be calculated from the theoretical model presented in chapter 1.4. Therefore the model was computed with start parameters for the eigenfrequencies of the modes in absence of nonlinear coupling $\bar{\omega}_{i0}$, the quadratic and cubic DC tuning factors c_i and d_i, as well as the vertex offset U_{i0} of the DC tuning parabola of each mode and the linear coupling constants κ_{ij}. As in the spectrum shown in Fig. 6.1, no linear frequency tuning (see chapter 5.2.2) could be observed, this was not takin into account for the theoretical model. The start parameters were

obtained by applying a genetic fit (for more details see chapter 4) to the mode spectrum shown in Fig. 6.1. The values for the respective start parameters are listed in the following table.

$\bar{\omega}_{10}$	:	$2\pi \cdot 5.8606 \cdot 10^6$ MHz
$\bar{\omega}_{20}$	:	$2\pi \cdot 5.9897 \cdot 10^6$ MHz
$\bar{\omega}_{30}$	:	$2\pi \cdot 6.1117 \cdot 10^6$ MHz
U_1	:	-0.656 V
U_2	:	-1.1 V
U_3	:	0.485 V
c_1	:	$2\pi \cdot 186.59$ Hz^2/V
c_2	:	$2\pi \cdot 1$ Hz^2/V
c_3	:	$-2\pi \cdot 282.5$ Hz^2/V
d_1	:	$2\pi \cdot 1.368$ Hz^3/V
d_3	:	$2\pi \cdot -2.2$ Hz^3/V
κ_{12}	:	$2\pi \cdot 4.138 \cdot 10^{12}$ Hz
κ_{13}	:	$2\pi \cdot 1.9098 \cdot 10^{12}$ Hz
κ_{23}	:	$2\pi \cdot 2.546 \cdot 10^{12}$ Hz

Table 6.1: List of start parameter for evaluating the eigenvalues e_{ij}.

From Eq.s (1.27) and (1.28) in chapter 1.4 we can see, that the DC dependence of the eigenvectors necessarily leads to a DC dependence of the Duffing constants $\tilde{\gamma}_{ii}$ and the dispersive coupling coefficients $\tilde{\gamma}_{ij}$. Consequently, the frequency-sweep measurements introduced in chapter 6.2 were performed for different DC voltages from 0 V to 20 V. Additionally, nonlinear frequency response measurements were performed in order to obtain the Duffing-coefficient for each mode at the respective DC voltages. A nonlinear frequency-response measurement including a fit of the Duffing nonlinearity is shown in Fig. 6.8. The measurement was done at 13 V and shows the Duffing curve of mode 3.

The amplitude v_3 of mode 3 (black dots) is fitted (red line) as a function of the detuning $\delta\omega_d$ of the drive frequency with γ_{ii} being the only free parameter of the fit

$$\delta\omega_d = \frac{3\gamma_{ii}}{8\omega_{i0}} v_i^2 + \sqrt{\frac{F^2}{4(\omega_{i0})^2 v_i^2} - \frac{\Gamma_i^2}{4}}, \tag{6.2}$$

where ω_{i0} is the linear eigenfrequency and F the effective drive power in units of V/s^2. The linewidth of the driven mode in the linear response regime is defined as the half damping rate $\Gamma_i/2$, and hence as the half of the full width at half maximum $\Delta\omega_i/2$ (see chapter 1.1).
The fit of Eq. (1.27) to the data shown in Fig. 6.8 yields a Duffing constant of
$\gamma_{33} = -4.07 \cdot 10^{18}$ Hz^2/V^2. The effective driving force F is calibrated from the output power P_{out} of the utilized high frequency Lock-in amplifier as follows

$$F = 2\omega_i \frac{\Gamma_i}{2} P_{out}^2 \sqrt{\frac{v_{i,max}}{P_{out,lin}^2}}. \tag{6.3}$$

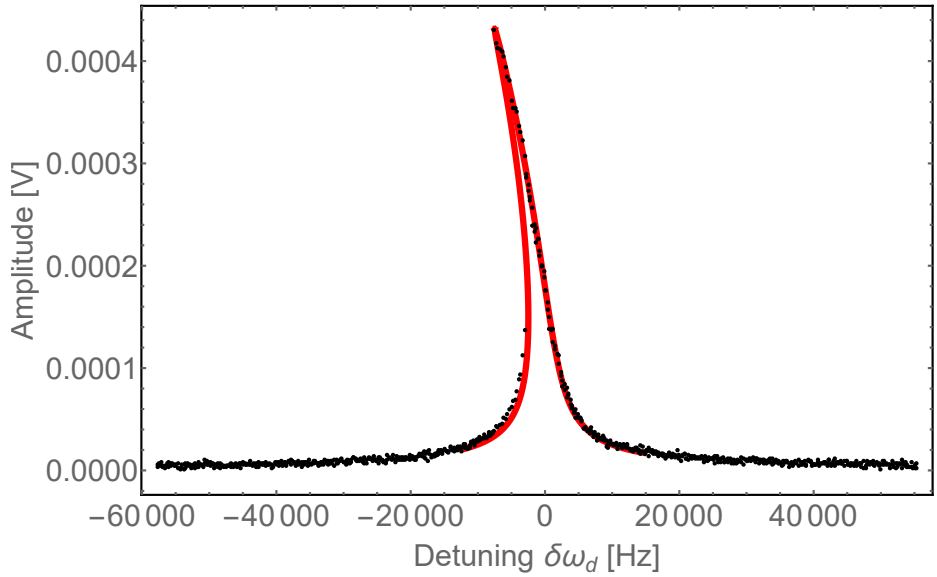

Figure 6.8: Nonlinear frequency response of mode 3 at 13 V (black dots) with the fit (red line) of the Duffing nonlinearity according to Eq. (6.2). The fit yields a Duffing constant of $\gamma_{33} = -4.07 \cdot 10^{18}\text{Hz}^2/\text{V}^2$.

Here, $v_{i,max}$ is the maximum amplitude in volt of the linear frequency response and $P_{out,lin}$ is the output power applied for measuring the linear response curve of the respective mode.
This evaluation scheme was applied for all nonlinear frequency-response measurements.
As mentioned above, these measurements were performed for different DC voltages from 0 V to 20 V to be compared with the theoretical prediction of the anayltical model of Eq. (1.27). Both, the measurements (dots) and the theoretical model (lines) are shown in Fig. 6.9.

The Duffing constants $\tilde{\gamma}_{11}$ (blue dots),$\tilde{\gamma}_{22}$ (red dots) and $\tilde{\gamma}_{33}$ (green dots) change tremendously with the applied DC voltage: being linear for small voltages, the sign of the Duffing constants change from positive to negative for increasing voltages, meaning that the Duffing curvatures of the modes transition from a stiffening behavior to a softening. For voltages between 5 V and 13 V this could be assigned to a transition from a geometric nonlinearity[69] ($\gamma_{ii} > 0$) to a dielectric nonlinearity ($\gamma_{ii} > 0$) being the dominant nonlinearity of the modes, as the DC voltage, and thus the dielectric force on the resonator is increased. For voltages higher than 13 V additionally the linear mode coupling has to be taken into account, making the dielectric nonlinearity and the effect of the linear coupling indistinguishable.
Figure 6.9 also shows that the theoretical model very well predicts the DC dependent and thereby the mode polarization dependent behavior of the Duffing constants $\tilde{\gamma}_{ii}$. Please note, that the solid lines in Fig. 6.9 do not show a fit of to the data, but the analytical model. Since the behavior of the modes, and hence the DC dependence of the eigenvectors are symmetric for positive and negative voltages, only the positive voltage range is depicted here. For some voltages, not all $\tilde{\gamma}_{ii}$ contain data sets, as for these voltages some modes were not accessible by the microwave enhanced detection technique (compare Fig. 6.1).

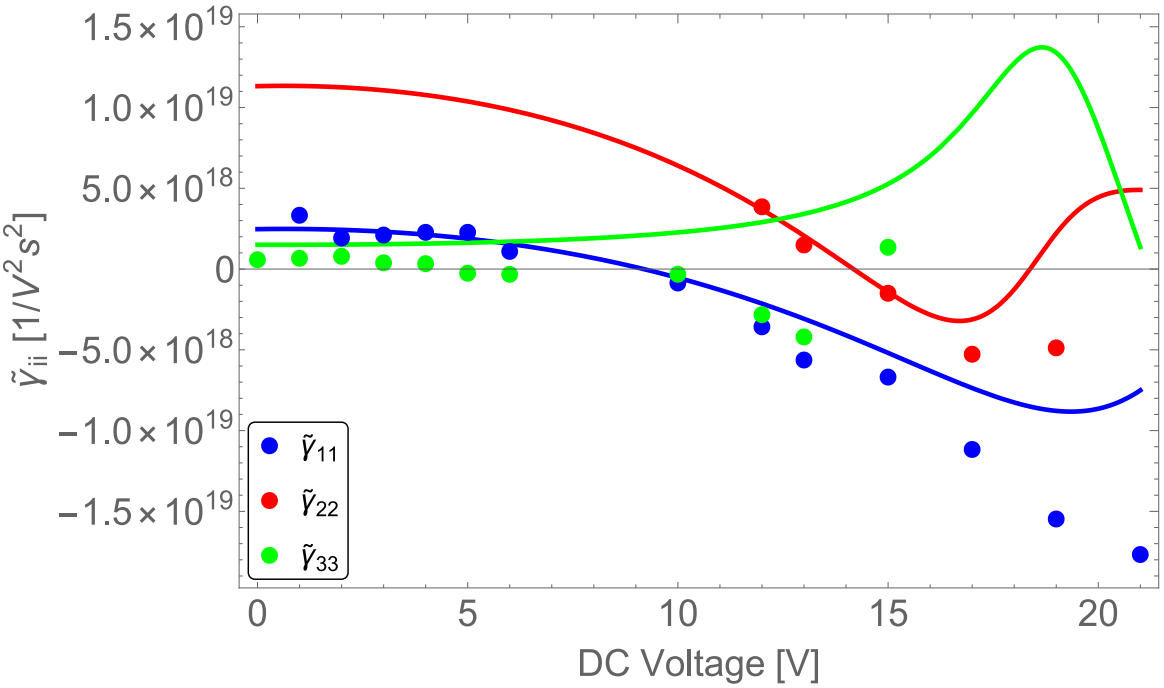

Figure 6.9: Duffing constants $\tilde{\gamma}_{11}$ (blue dots),$\tilde{\gamma}_{22}$ (red dots) and $\tilde{\gamma}_{33}$ (green dots) for different voltages from 0 to 20 V. The respective lines correspond to the theoretical model from Eq. (1.27).

In order to evaluate the theoretical model, parameters for the bare, undisturbed Duffing constants γ_{ii} and the pure dispersive coupling-coefficients γ_{ij} are required. But as the system is never completely decoupled (compare Fig. 6.7), the values obtained for the coupling-constants and Duffing-coefficients are not the bare parameters needed for the theoretical model. Therefore, the mean values of the measured γ_{11}, γ_{33} and γ_{13} were chosen and subsequently all parameters were adapted until finally a set of parameters was obtained suitable for the analytical model to qualitatively reproduce the measured DC dependence of the Duffing constants. The respective parameters are listed in table 6.3.

γ_{11}	:	$2.2 \cdot 10^{19}$ 1/(V^{2}s^2)
γ_{22}	:	$3.8 \cdot 10^{19}$ 1/(V^{2}s^2)
γ_{33}	:	$0.1 \cdot 10^{18}$ 1/(V^{2}s^2)
γ_{12}	:	-6.5 $\cdot 10^{19}$ 1/(V^{2}s^2)
γ_{13}	:	$8 \cdot 10^{18}$ 1/(V^{2}s^2)
γ_{23}	:	$1.3 \cdot 10^{19}$ 1/(V^{2}s^2)

Table 6.2: List of parameter for evaluating the polarization dependent Duffing constants $\tilde{\gamma}_{ii}$ and dispersive coupling-coefficients $\tilde{\gamma}_{ij}$.

Plugging in these parameters into Eq. (1.28), we get the theoretical model predicting the polarization dependence of the dispersive coupling-coefficients $\tilde{\gamma}_{ij}$. The model (solid lines), as

well as measured values (dots and circles) of the coupling-coefficients $\tilde{\gamma}_{12}$ (blue dots), $\tilde{\gamma}_{21}$ (blue circles), $\tilde{\gamma}_{13}$ (red dots), $\tilde{\gamma}_{31}$ (red circles) and $\tilde{\gamma}_{23}$ (green dots) and $\tilde{\gamma}_{32}$ (green circles) are shown in Fig. 6.10. Here frequency-sweep measurements were performed for different voltages from 0 to 20 V and for different drive powers from -25 Bm to -10 dBm. The data in Fig. 6.10 shows the corresponding mean value of the respective different drive powers.

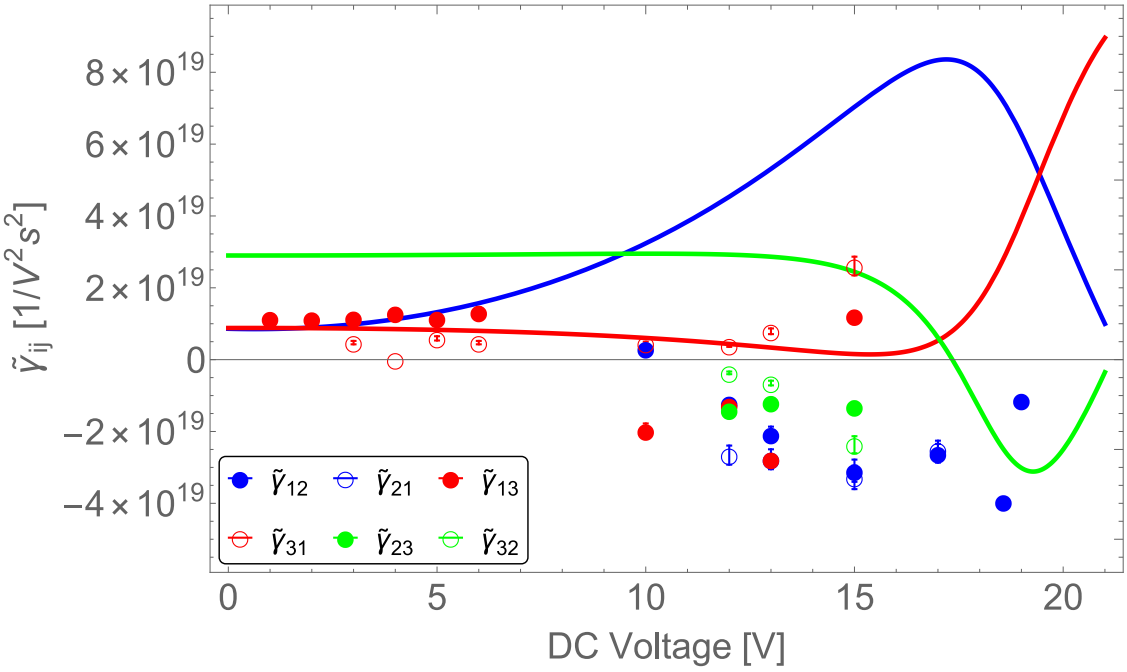

Figure 6.10: Coupling-coefficients $\tilde{\gamma}_{12}$ (blue dots), $\tilde{\gamma}_{21}$ (blue circles), $\tilde{\gamma}_{13}$ (red dots), $\tilde{\gamma}_{31}$ (red circles) and $\tilde{\gamma}_{23}$ (green dots) and $\tilde{\gamma}_{32}$ (green corcles) for different voltages from 0 to 20 V. The respective lines correspond to the theoretical model from Eq. (1.28).

We find that the theoretical model predicts a pronounced change of the coupling-coefficients when the modes hybridize.
Generally the theoretical mode from Eq. (1.28) predicts $\tilde{\gamma}_{ij} = \tilde{\gamma}_{ji}$. However, we find some deviations between the respective coupling-coefficients, for example $\tilde{\gamma}_{12}$ and $\tilde{\gamma}_{21}$. This may be caused by the unequal sensitivity of the measurement technique to the modes. Besides this, the modes themselves show a drift in frequency over time, leading to a mean variation in γ_{ij} of about 10%, as indicated by the error bars in Fig. 6.10. Additionally we find that the values scatter in the region where the modes start to hybridize (around 15 V) and can not reproduce the theoretical model. Therefore, the measurement data in this region has to be handled with care. For lower voltages, the coupling-coefficients show a better agreement with the model, though here only data from modes 1 and 2 are available.
Overall we find that the Duffing constants and the dispersive coupling-coefficients strongly depend on the hybridization of the modes. For further investigation it necessary to utilize the 3-electrode or the 5-electrode sample layout in order to access both resonators independent for

actuation and especially for detection via the microwave cavity enhanced readout. This will reduce the constrains concerning the availability of measurement data for some modes. Furthermore, a Peltier element could be added to the sample holder to stabilize the temperature fluctuations of the frequencies of the modes, and thus reduce the scattering of the obtained coupling-coefficients.

Chapter 7

Conclusion and outlook

In this thesis, the coupling mechanisms of two parallel silicon nitride string resonators sharing one clamping point were investigated, beginning from the sizing and design of the resonators, clamping points and coupling window structure, via fabrication up to the measurement of linear and nonlinear mode coupling. Finite element simulations revealed that the implementation of a window structure in the shared clamping point of the resonator pair enhances the expansion of a strain field into the clamping point, and thus favors the exchange of vibrational energy via this clamping point. Additional simulations were made to gather knowledge about the impact of size and spacing of the individual geometric parts of the system, like the distance between the resonators, the thickness of the window ledge and the coupling beam width on the mechanical coupling strength of the modes. By choosing these structural dimensions on purpose, the strength of the strain coupling can in principle be pre-adjusted. However, in practice it turned out, that fabricational intolerances are larger than the changes in coupling strength caused by small changes in the dimensions of the coupling beam and window ledge. For now, this limits the possibility to pre-adjust the mechanical coupling strength at will.
A dielectric actuation technique was applied to the resonators to tune the modes in frequency, such that two, or even three modes of the system could be brought in resonance. By these means, the linear mechanical strain- and in addition, dielectric coupling testifies itself in the appearance of avoided mode crossings. Depending on the number of involved modes, a simple two-mode avoided crossing, or a more complicated multi-mode avoided crossing arose. A genetic algorithm was developed to evaluate the coupling strength between the modes, showing that with linewidths in the range of about 10 Hz to 20 Hz and coupling strengths of 30 kHz to 130 kHz the system is well within the strong coupling regime. Furthermore, the mode polarization was calculated by solving the eigenvalue equation of the coupled equations of motion of the system. By following the mode polarizations through the avoided crossings it was possible to identify hybridized modes.
We found that the interferometric readout technique leads to temperature fluctuations in the eigenfrequencies of the modes caused by heating of the resonators by the laser. This can possibly be avoided by employing the microwave cavity enhanced readout technique. But as the

microwave cavity readout is most sensitive to the modes of the resonator coupled directly to the microwave cavity, it is necessary to supply both resonators with a separate cavity. So, another task of this work was to make the resonator system, as well as the sample holder design, suitable for the application of two microwave cavities for simultaneous and separate dielectric actuation and readout of the resonators. Therefore, the sample design was adapted to meet the needs of these requirements. New sample layouts were designed, which contain separate electrodes for each resonator, and hence allow for dielectrically addressing both resonators separately. It was shown, that the existence of a second electric field surrounding the resonators allows for modifying the frequency-tuneability of the modes. The impact of the additional static electric field on the frequency tuning strongly depends on the mode polarization. As for out-of-plane modes a strong enhancement of the DC voltage tuning strength up to 180% was found, compared to the case without the additional field, the in-plane modes were affected in a more versatile way: if the in-plane mode shows a linear dependence on the DC voltage, a change in the additional electrical field can change the tuning direction from positive to negative and vice versa, and thus opening paths to not only tune the eigenfrequency of the mode but also adjust the DC tuning strength by adjusting the additional DC bias.

Besides the linear strain- and dielectric coupling, and diverse frequency tuning opportunities, the system offers nonlinear effects like dispersive mode coupling. It was shown, that the modes of the system experience a change in eigenfrequency, if the amplitude of one mode is increased and the respective mode transitions from a linear to a Duffing resonator. Furthermore, the Duffing nonlinearity and the dispersive coupling strength strongly depend on the DC voltage and thereby on the mode polarization. Therefore, a change in polarization caused by hybridization of the modes, leads to a change in the Duffing constants and the dispersive coupling-coefficients of the modes.

A theoretical model was applied to predict this hybridization dependence. The comparison of the model with measured data showed a very good agreement for the Duffing constants. Yet, the coupling-coefficients scattered in the region of the mode hybridization, such that a clear qualitative agreement of the model and the measured data was only available for small DC voltages, where the modes were only marginally hybridized.

Additionally it was shown that the dispersive coupling-coefficients between two modes are not equal ($\gamma_{ij} \neq \gamma_{ji}$). This deviation between the coupling-coefficients γ_{ij} and γ_{ji} and their scattering in the hybridized regime may be caused by fluctuations in frequency of the mode, combined with deficiencies of the microwave cavity readout technique like unequal mode sensitivity and dielectric damping.

In a first attempt to optimize the system and eliminate these inadequacies, the sample layout should be changed to the 5-electrode geometry, as this provides individual actuation and microwave cavity enhanced readout of both resonators. With additional lock-in amplifiers for both microwave cavities, the phase correlation of the modes could be resolved, giving exmperimental insight in the exact mode shape of the hybridized modes. Moreover, this allows for intense investigation on self-oscillation, giving rise to interesting physics like frequency mixing and injection locking,[70] as well as mode-synchronization of the system. Also, replacing the $\lambda/4$ microwave cavity by a 3D cavity[71,72] holds opportunities to increase the coupling of the modes to the microwave cavity and hence, increase the sensitivity of the readout technique.

Optionally the laser for optical readout could be changed to telecommunication wavelength, reducing the absorption of silicon nitride, and thus heating and related frequency fluctuation effects drastically.
Coming back to the sample optimization, the 3- and 5-electrode geometry both enable discrete and multifunctional mode tuning and thus allow for adjusting the mechanical strain coupling. This provides the possibility to build large nanomechanical arrays[73,74] and even realize phononic cristalls with tunable band structures[23,75,76] for phonons traveling through the array.
Redesigning of the sample, for example by implementing an angle between the resonators, changing the shape of the window structure or the clamping region will certainly affect the linear strain coupling, and hence open up a tool-box for adjusting the mechanical properties of the system to meet the needs for versatile opto- and electro-mechanical applications.[21,22] Additionally, the resonators could be metalized,[77] e.g. for coupling the system to cold atoms.[65,66] To this extend we have a collaboration with the group of Prof. Dr. József Fortágh in Tübingen. We have fabricated samples suitable for coupling individual modes of silicon nitride string resonators to cold atoms, in order to realize a nanomechanical quantum galvanometer. First measurements on this are in progress.
By further engineering the design and dimensions of the resonators more nonlinear effects could be available by the system like internal resonances[27] and limit cycles,[40] or even[78] three-body interaction.[78] Beyond the study of nonlinearities, the system object to this work can access the chaotic regime, where a variety of interesting physical phenomena waits to be explored.

Appendix A

Fabrication steps and parameters

In this Appendix, a step by step sample fabrication process is given, with state of the art fabrication step order and parameters by the time of finishing this thesis. Please note, that some parameters like electron-beam lithography specific settings may vary over time and have to be readjusted properly.

Cleaning and spincoating

Process step	Device	Parameters
Label	Diamond tip	Scratch on top side of sample Labeling on bottom side
Clean	Ultrasonic bath	Acetone, 2 min Rinse in Isopropanol Dry with N_2
Spin coat	Spincoater	PMMA 950 K A6 1: 1 s at 800 rpm 2: 30 s at 5000 rpm
Soft bake	Hot plate	90 s at 180° C
Spin coat	Spincoater	Electra 92 (AR-PC 5090) 1: 60 s at 4000 rpm
Soft bake	Hot plate	120 s at 90° C

E-beam lithography for electrodes and bondpads

Process step	Device	Parameters
Lithography	REM*	Aperture: 20 µm Voltage: 10 kV Dose: 100 µC/cm^2
Remove Electra	DI-Water	Rinse for 60 s
Development	MIBK:IPA (1:3)	50 s Rinse in Isopropanol Dry with N_2

Etchmask/electrode metalization

Process step	Device	Parameters
Metalizaition of electrodes	E-beam evaporator†	200 nm Au
Lift-off	Acetone and ultrasonic bath	At 4 minutes 40°-50° C Rinse in Isopropanol Dry with N_2

Spincoating, second step

Process step	Device	Parameters
Spin coat	Spincoater	PMMA 950 K A6 1: 1 s at 800 rpm 2: 30 s at 5000 rpm
Soft bake	Hot plate	90 s at 180° C
Spin coat	Spincoater	Electra (AR-PC 5090) 1: 60 s at 4000 rpm
Soft bake	Hot plate	120 s at 90° C

Zeiss CrossBeam 1540XB

†*AJA HTC Orion 8 Deposition System*

E-beam lithography for resonators

Process step	Device	Parameters
Lithography	REM	Aperture: 20 µm Voltage: 10 kV Dose: 100 µC/cm^2 Resonator: 160 % Dose Window structure: 130 % Dose Clamping: 100 % Dose
Remove Electra	DI-Water	Rinse for 60 s
Development	MIBK:IPA (1:3)	50 s Rinse in Isopropanol Dry with N_2

Etchmask for resonators

Process step	Device	Parameters
Etchmask Lift-off	E-beam evaporator Acetone and ultrasonic bath	180 nm Al at 4 minutes 40°-50° C Rinse in Isopropanol Dry with N_2

Plasma etching

Process step	Device	Parameters
Anisotropic etching	ICP-RIE[‡]	Time: 3 min 34 s ICP-Power: 350 W RF-Power: 65 W Forwardbias: 279-290 V Volume flow: SF_6 2 sccm Volume flow: Ar 4 sccm Chamber pressure: 2 mTorr Temperature: 10° C

[‡] *Oxford Plasmalab 100*

Chemical wet etching

Process step	Device	Parameters
Etchmask removal	NaOH (50 MOl)	Time: 2 min Rinse in DI-water
Isotropic wet etch	BHF[§] (HF and NH_4)	Time: 3.5 min Rinse in DI-Wasser Clean with Isopropanol Remove sample from hot Isoprpanlo 50°-60° C Dry with N_2, or use critical point dryer[††] (Isopropanol and CO_2)

[§] *Technic France* buffered hydrofluoric acid BOE 7-1

[††] *Bal-Tec CPP 030*

Appendix B

Fabrication issues

Because of the large number of fabrication steps involved in this project, many things did not working out as expected at the beginning.
In order to make this section as useful to future nanolab "inhabitants" as possible, I try to give a solution to as many problems as possible.

B.1 Conductive layers

As SiO_2 is insulating, a conductive layer is essential for e-beam lithography. With PMMA 950K A6, the conductive polymer Electra 92 is suitable and as you can spin-coat it, it is very time saving. Also either 5-10 nm of chromium or aluminum are feasible.
At some point you may see "tree" -like shapes on your sample in the SEM; this happens when Electra 92 is old and coagulating.
Aluminum can easily be removed with NaOH (0.5 Mol). For chromium, *Transene Chromium Etchant 1020 : DI water (1:1)* works well. The polymer Electra 92 can be removed with DI water.

B.2 E-beam lithography

One issue that may cause problems for e-beam lithography is the temperature dependence of the exposure parameters, strictly speaking the dose factor. It is necessary to readjust the dose factor from time to time, especially when seasons change and it becomes colder or warmer in the fabrication lab. While temperature is mostly stable during autumn and winter, it increases and varies a lot during spring and summer time. It may even be required to do weekly dose tests, or shift the lithography process to the very early morning (finish before sunrise) or late night.
Readjustment of the dose factor is also needed, when the cathode of the SEM was changed.
All samples shown in this work were structured using the *Elphy Plus*-lithography system from

Raith Nanofabrication. This lithography system requires new basic write field adjustment from time to time, if a two-step lithography process is used for sample fabrication. This realignment has to be carried out whenever some work on the lithography system was done (this includes even minor maintenance procedures), to secure that the structure alignment that has to be performed during every two-step lithography does not have any offset.

B.3 Trying different e-beam resits

Since we use a plasma etching step during fabrication and this requires protecting the structures with some etch-mask, there is the need to evaporate a metal (see B.4 for different types) on to the sample and to do an additional lift-off. This makes two additional steps which take time and the sample can be damaged either by falling, being scratched with the tweezers, by evaporation problems, etc.
Therefore we tried two different e-beam resists, which are supposed to work well also as an etch-mask for the fluorine-etching process we do: *ma-N 2400 Negativ-Photoresist* from *micro resist technology* and *AR-P 6200 (CSAR 62)* from *Allresist*.

ma-N 2400 negative resist

This e-beam resist is supposed to work well with all kinds of silicon substrate and also with most types of conductive layers including chromium and aluminum. However, it turned out that some commercially available chromium-etchants destroy this resist (tried products:*Transene Chromiumetchant 1012*and *BASF Selectipur Chromium etchant*). Even after only 1 second in highly diluted chromium-etchant the resist on the sample will shine in many colors with an overall washed-out look. Any further development of the resist will not make any change to this surface; neither will it remove parts of the resist, nor will you see any e-beam-written structure.
We then switched to aluminum as conductive layer: aluminum etchants including HNO_3, CH_3COOH and H_3PO_4 also damage the resist. NaOH does indeed not do any harm to the resist, but it develops it. This is also a problem, since it doesn't remove the aluminum homogeneously and therefore also develops the resist inhomogeneously.

It also turned out, that ma-N 2400 is not compatible with our plasma-etch-recipe. By adjusting the recipe one would probably be able to use ma-N 2400 as an etch-mask, but as we had not a too good impression of the compatibility of this resist with parts of our fabrication-process, we dismissed this idea.

CSAR 62 positive resist

This resist is supposed to have an even better etch-mask-performance than the ma-N 2400. It turned out, that this resist is also not compatible with our plasma-etch-recipe. Even for shorter etching-times and with additional hard bake the results were not convincing. Additionally it was

not clear wether there was still resist on the sample after the plasma-etch. Different attempts to get rid of possible resist-residues failed. Among these were: rinsing in Acetone, O_2 plasma-cleaning and rinsing in *pirañha* (sulfuric acid (95%), hydrogen peroxide (30%)). Therefore we did not further investigate this resist and decided to stay with the metallic etch-mask.

B.4 Possible etch-masks

There are many different metals suitable as an etch-mask for the plasma-etch-step. In the scope of this work, three different metals were mainly used: gold, aluminum and cobalt.
As gold is rather soft, it is necessary to evaporate more than the amount you want to have on the sample after the etch. The etch rate of gold here is about 0.4 nm/s. If one wishes to have minimum 50 nm to 100 nm of gold remaining on the structures, it is recommended to evaporate 130 nm - 180 nm.

Aluminum is a good etch-mask and also very convenient during the lift-of-step. But, after the plasma-etch it may happen sometimes, that the aluminum-mask exhibits small distinct holes which go down all the way to the SiN-layer. This was observed for evaporated layer thicknesses of 40 nm - 50 nm. For thicknesses from 70 nm - 90 nm these holes do not appear. It is also possible to protect a well defined gold layer with an additional aluminum mask. Please note, that the evaporation rate is crucial to the quality of the aluminum layer. Usually "faster is better" holds here. For too low rates, the surface of the aluminum layer is very rough and you can see small clusters in the electron microscope. If the evaporation rate is high enough, the surface looks very smooth, without these clusters. However, if the rate is too high, the quality of the aluminum layer gets worse again. It may be, that the roughness of this aluminum etch mask has an impact on the deviation of the eigenfrequencies discussed in chapter 2.1.

Last but not least, cobalt is a perfectly valid alternative, as long as one does not care about magnetic materials in the evaporation chamber and on the sample. The cobalt-lift-off is easy to perform and evaporated layers of 30-50 nm are absolutely sufficient for the plasma-etch.

B.5 Evaporating system (Tom Dooley)

The old evaporating system (called *Tom Dooley* for it's shape) has some characteristic peculiarities, which one has to be aware of. As it is a non programmable device and therefore everything has to be operated manually, one has to be careful in handling it. During the time of this project, the author spent some time fixing several issues on this evaporating system. By now, all "inner" parts that can be changed, are changed and renewed, like for example the filament, copper leads, fuses and diverse ceramic insulators -including the high voltage vacuum feedthrough with ceramic insulator.
During evaporation it is very important to avoid splashing of the evaporation material as some small parts may hit the filament section, and thus cause shortages and the breakdown of the

system. If this happens, the filament has to be changed. Also the ceramics have to bee cleaned every once in a while because carbon may assemble on their surface and cause shortages (especially on the vacuum feedthrough). If the system is run thoughtfully, it is a very reliable device, suitable for diverse materials. Amongst others, these are cobalt, gold, chromium, titanium, platinum and silicon dioxide.

Appendix C

Devices in measurement setup

In the following, a list of the used devices is given. Setup specific devices are listed in the respective subsection of this appendix. Both setups are combined in one integrated measurement setup and are now only listed as individual setups in order to show the respective components.

General Devices

Turbo pump stand	Pfeiffer Vacuum HiCube 80 Eco DN40 ISO-KF with DCU
Pressure sensor	Oerlikon Leybold Vacuum Thermovac TTR100
Sandbox	Outer dimensions $54\times51\times40$ cm^3, 85 L, >224 kg
Laser	Coherent Obis $\lambda = 640$ nm frequenzstabilisiert 40 m
Optical elements	Thorlabs + LINOS 32/52 No.618 Faraday Isolator
Microscopic lens	MSPlan50 0.55 ∞/0 f = 180 IC 50
Photodiode	Manus Handwired Amplifiers
Piezo positioner	Attocube ECC100 Controller + 3 x ECS3030-S1
Power splitter	Mini-Circuits ZFSC-2-10 G+ 0°/0°
Power splitter	MARKI IQ-0307 LXP I/Q
	Mixer Mini-Circuits JSPQW-65+ 0°/90°
Low pass filter	Mini-Circuits VLFX-225, $f_g = 225$ MHz
Amplifier	MITEQ AU-1464-R, +35 dB
Bias tee	Mini-Circuits ZFBT-6 GW+
SLC single layer capacitor	Johanson Technology Microwave SLC 1800 pF
Vector network analyzer	Rhode & Schwarz ZVB 4
Signal analyzer	Rhode & Schwarz FSV 4, and/or FSV 7
2 Signal generators	Rhode & Schwarz SMA 100A
2 Waveform generators	Keysight 33500B
2 Source meters	Keithley 2401
Voltage/current source	Yokogawa GS 200
Lock-in amplifier	Zurich instruments HF2LI

C.1 Interferometric setup

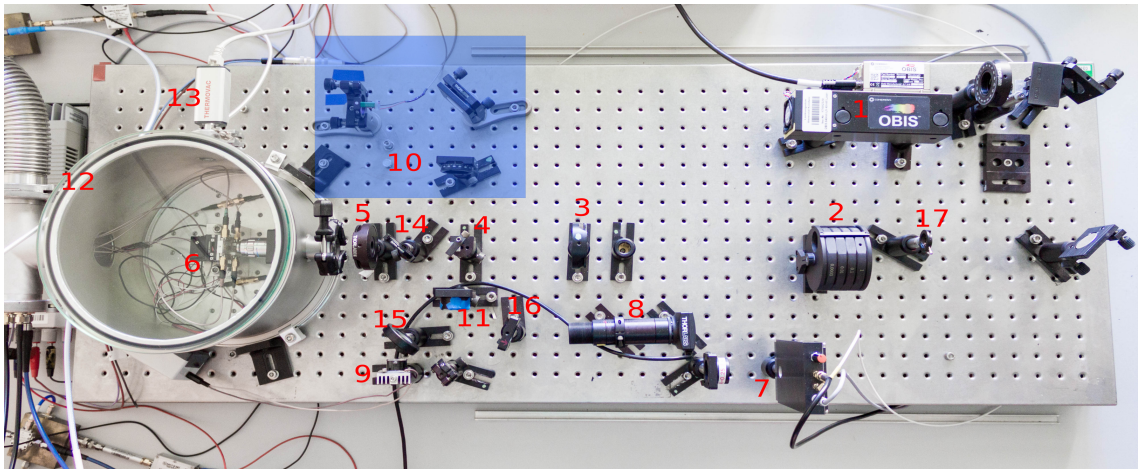

Figure C.1: Optical setup with a 640 nm Laser (1), optics (2-5,10,11,14-17), vacuum chamber with sample holder and sample (6,12) and CCD Detector (8)

1	Laser with Faraday-isolator	Vertical polarizer towards laser
2	Attenuator	Adjustable
3	$\lambda/2$ wave plate	At 152°
4	Polarizing beam splitter	
5	$\lambda/4$ wave plate	At 40°
6	Sample, sample holder, positioner, microskope lens	
7	Lens and photodiode	Focus 50 mm
8	CCD detector	connected to LCD-monitor
9	LED	At 15 V
10	Reference arm	blocked
11	Linear polarizer	At 45°
12	Vacuum chamber	Pressure lower than $5 \cdot 10^{-4}$ mbar
13	Pressure sensor	
14	92/8 Beamsplitter	
15	50/50 Beamsplitter	
16	Low-pass filter	FES0650, 650 nm
17	Apertures	

C.2 Dielectric setup

Here devices in the dielectric setup are listed and illustrated for the 2-electrode geometry. For the 3- and 5-electrode geometry, the devices are the same. For the 3-electrode geometry layout which was used in chapter 5.2, we applied two sets of devices 1 to 4 (light blue box). For the 5-electrode geometry two sets of devices 1 to 4 and two sets of devices 6 to 12 are needed (light orange box).

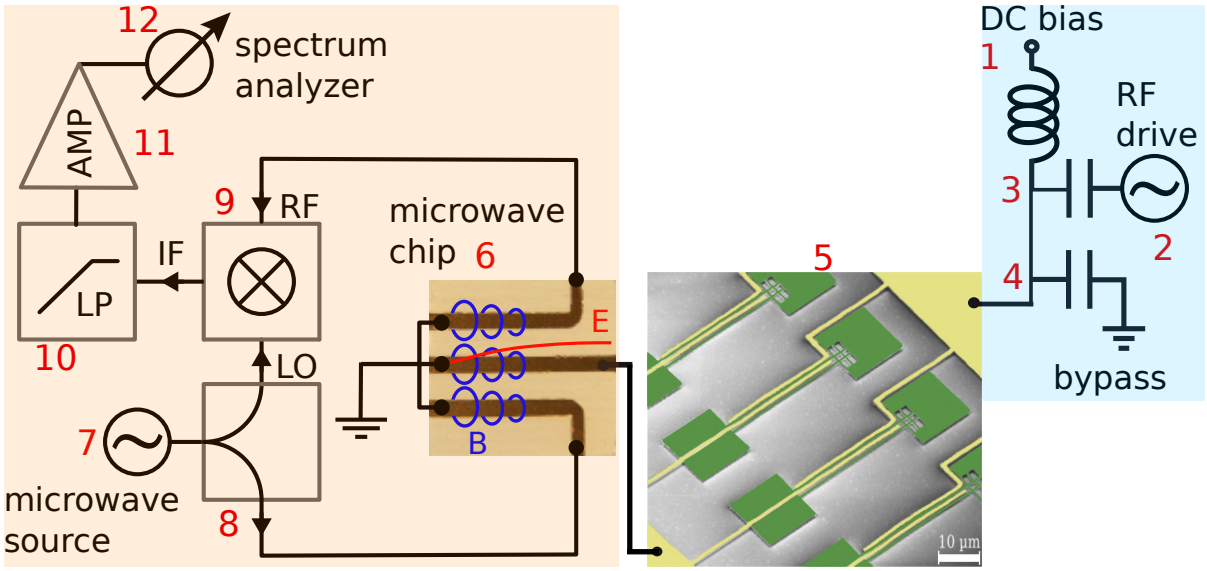

Figure C.2: Experimental setup for dielectric actuation and microwave cavity enhanced readout. For detailed information on the working principle, see chapter 3.2 and 3.3

1	Source meter
2	Waveform generator
3	Bias tee
4	SLC single layer capacitor
5	Silicon nitride resonator pair
6	λ microstrip cavity
7	SMA signal Generator
8	Power splitter 0°/0°
9	Power splitter 0°/90°
10	Low pass filter
11	Amplifier
12	Signal analyzer / Network analyzer

Appendix D

Chaotic states

The resonators subject to this work show Q factors of about 200 000 and therefore offer nonlinear effects like dispersive coupling. However, if the system is driven too strongly, it can enter the chaotic regime. Here are some examples of power sweeps like they are performed in chapter 6.2, where the coupled modes show a strong nonliear or even chaotic behavior. The measurements shown here were performed with the sample investigated in chapter 6.2 and we employed the interferometric readout technique for all measurements.

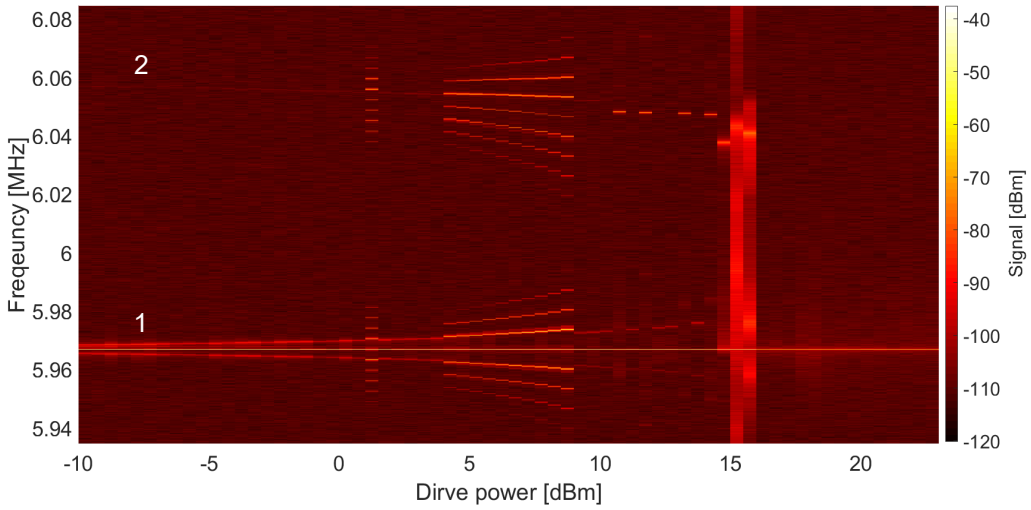

Figure D.1: Power sweep of resonant drive of mode 1 from −10 dBm to 25 dBm at 7.2 V. For a drive power of 1.5 dBm multiple satellites arise and suddenly break down for too high drive powers, where the system becomes chaotic.

Figure D.1 shows a power sweep of mode 1, varying the drive power from −10 dBm to 25 dBm at 7.2 V. Mode 1 is driven on resonance at 5.694 MHz. For a drive power higher than 1.5 dBm, the system does not just reveal dispersive mode coupling between mode 1 and 2, but shows multiple symmetric satellite peaks around each mode. If the power is further increased, these

satellites suddenly disappear and the system enters chaos at 15 dBm.

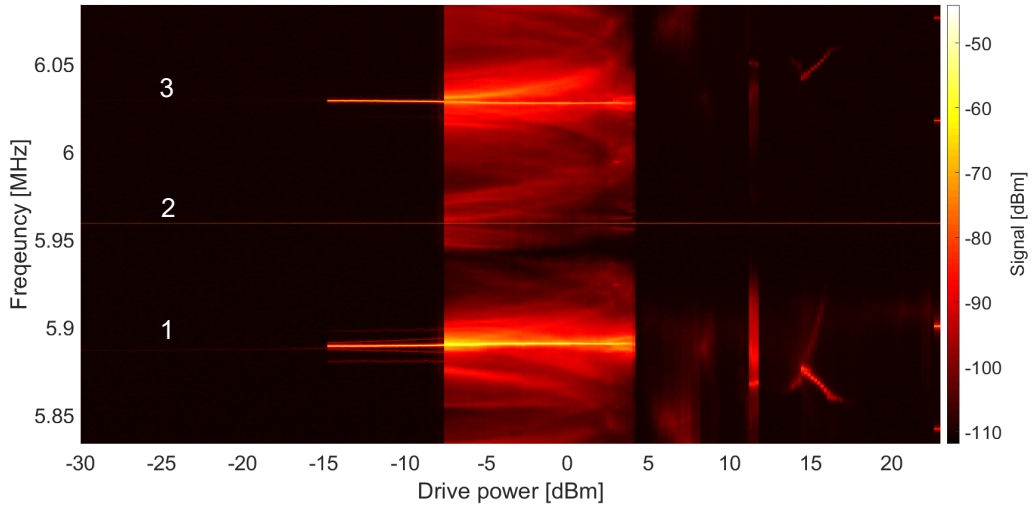

Figure D.2: Power sweep of resonant drive of mode 2 from −30 dBm to 22 dBm at 14 V. For a drive power of −15 dBm the system presumably enters self-oscillation.

In Fig. D.2 a power sweep of mode 2 is shown, varying the drive power from −30 to 22 dBm at 14 V. Mode 2 is driven on resonance at 5.627 MHz. Here we don't see the multiple satellite peaks, but an erratic increase in the amplitudes of modes 1 and 3 for a drive power of −15 dBm. This can be a state of self-oscillation. As the drive power is further increased beyond −7 dBm, nebular features appear, before the system transitions thoroughly into chaos.

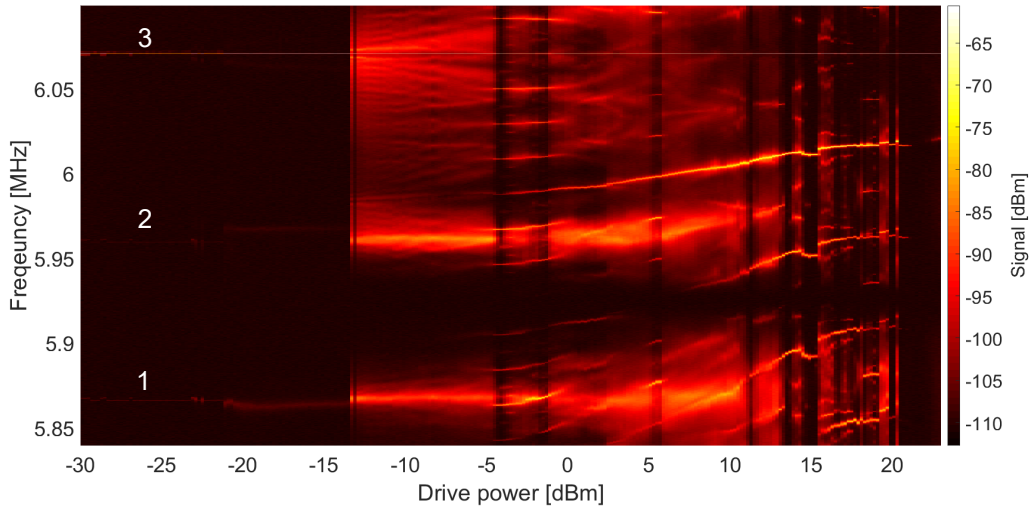

Figure D.3: Power sweep of resonant drive of mode 3 from −30 dBm to 22 dBm at 9 V. The system shows features that exhibit a symmetric behavior, even in the chaotic regime.

Another example is given in Fig. D.3, for a power sweep of mode 3, varying the drive power

from -30 to 22 dBm at a DC voltage of 9 V. Here the system enters the chaotic regime at a drive power of -15 dBm showing again nebular features. However, for drive powers between -5 dBm and -1 dBm a region appears, where clear and symmetric peaks can be distinguished. Also even in the nebular regions there are some features showing a symmetric behavior.
The examples shown here, are just a selection of chaotic states of the system, but they offer new interesting physics to be explored.

Danksagung

An dieser Stelle wird es endlich Zeit sich bei einigen Personen für einige Dinge zu bedanken.

Zu aller erst danke ich Frau Prof. Dr. Eva M. Weig für die Betreuung dieser Doktorarbeit. Es waren viereinhalb spannende und interessante Jahre in denen ich viel über Nanomechanik, Gerätereparatur und die Relativität von Zeit gelernt habe. Während der gesamten Zeit mit Dir hattest du immer ein offenes Ohr für mich und hast mich unterstützt soweit es Dir möglich war. Du hast mir stets freie Hand gelassen sowohl bei der Wahl als auch bei der Organisation meiner Projekte und ich kann sagen, dass ich auch in dieser Hinsicht viel von Dir habe lernen können. Vielen Dank Eva.
Bei Frau Prof. Dr. Elke Scheer bedanke ich mich für das Zweitgutachten dieser Arbeit und ebenso für die Übernahme der mündlichen Prüfung in einem experimentellen Spezialgebiet.
Gleichwohl danke ich Herrn Prof. Dr. Wolfgang Belzig für die Übernahme der mündlichen Prüfung in einem theoretischen Spezialgebiet.
I would like to thank Dr. Gianluca Rastelli for developing the theoretical model for the mode polarization dependence of the Duffing constants and the dispersive coupling-coefficients. You put a lot of time and effort in this project and our weekly discussions. You were there whenever I had concerns and questions and helped me a lot to understand the nonlinear behavior of our sample. Thank you very much.
Ferner möchte ich mich bei der gesammten "Cold-Atoms-NEMS"-Gruppe mit Prof. Dr. Jozsef Fortagh, Dr. Andreas Günther, Dr. Simon Bell, Dr. Peter Federsel, Carola Rogulj, Malte Reinschmidt und Maximilian Seitner für die interessante kollaboration bedanken. Ich hoffe sehr, dass das Projekt eines Tages Früchte trägt.
Spezieller Dank gilt meinen beiden Masterstudenten Simon Schüz und Martin Schill für ihren beherzten Einsatz für die Forschung :). Ohne euer Zutun hätten wir nicht so viele interessante Erkenntnisse gewinnen können. Ich wünsche euch beiden alles Gute für die Zukunft.
Ich danke außerdem Matthias Hagner für die gute Zeit, den guten Rat und die gute Organisation des Nanolabors. Mögen niemals mehr Fledermäuse oder ein Wasserschaden das Nanolab heimsuchen!
Bei der gesamten Arbeitsgruppe mit Maximilian Bückle, Juliane Doster, Yannick Klaß, Jana Huber, Irene Sánchez Arribas, Anh Tuan Le und bei meinem "Büromitbewohner" Felix Rochau bedanke ich mich für die wunderbare Zeit mit euch. Es war immer lustig und unterhaltsam und ihr standet mir immer reichlich mit Rat und Tat zur Seite. Ohne euch wäre meine Zeit als

Doktorandin sicherlich nicht so schön gewesen. Ich wünsche euch von ganzem Herzen viel Erfolg für eure eigene Promotion und alles Gute für die Zukunft.
Louis Kukk danke ich für die tollen Probenhalter und überhaupt dafür, dass du bei technischen Fragen aller Art immer zur Stelle warst und ich mir öfter dein Werkzeug ausleihen durfte.
Ganz herzlicher Dank geht an meine Familie und speziell an meine Eltern Isolde und Peter. Vielen Dank für eure unermüdliche Unterstützung: ohne euch hätte ich das alles nicht geschafft!
Ferner möchte ich Dennis Bumüller, Alexander von Weber und Maximilian Bückle danken: für eure Freundschaft, für die gute Zeit und dafür, dass ihr mich schon so lange begleitet.
Bei Joel Tschannen möchte ich mich ebenfalls recht herzlich für deine unermüdliche Unterstützung und deinen Zuspruch bedanken.
Zu guter Letzt gilt mein ganz besonderer Dank meiner Schwester Julia Gajo für ihre liebenswerte und lebenslustige Art. Du warst immer für mich da und hast mich unterstützt und auf andere Gedanken gebracht wann immer es nötig war. Ohne Dich wäre mein Leben ganz schön lasch!

Bibliography

[1] J. Chaste, A. Eichler, J. Moser, G. Ceballos, R. Rurali, and A. Bachtold. A nanomechanical mass sensor with yoctogram resolution. *Nat. Nanotech.*, 7:301, 2012.

[2] J. Moser, J. Güttinger, A. Eichler, M. J. Esplandiu, D. E. Liu, M. I. Dykman, and A. Bachtold. Ultrasensitive force detection with a nanotube mechanical resonator. *Nat. Nanotech.*, 8:493, 2013.

[3] B. P. Abbott et al. Gw170817: Observation of gravitational waves from a binary neutron star inspiral. *Phys. Rev. Lett.*, 119:161101, 2017.

[4] M. Eichenfield, R. Camacho, J. Chan, K. J. Vahala, and O. Painter. A picogram- and nanometre-scale photonic-crystal optomechanical cavity. *Nature*, 459:550, 2009.

[5] M. Eichenfield, J. Chan, R. M. Camacho, K. J. Vahala, and O. Painter. Optomechanical crystals. *Nature*, 462:78, 2009.

[6] H. Okamoto, A. Gourgout, C. Chang, K. Onomitsu, I. Mahboob, E. Y. Chang, and H. Yamaguchi. Coherent phonon manipulation in coupled mechanical resonators. *Nat. Phys.*, 9:598, 2013.

[7] J. Suh, A. J. Weinstein, C. U. Lei, E. E. Wollman, S. K. Steinke, P. Meystre, A. A. Clerk, and K. C. Schwab. Mechanically detecting and avoiding the quantum fluctuations of a microwave field. *Science*, 344:1262, 2014.

[8] F. Lecocq, J. B. Clark, R. W. Simmonds, J. Aumentado, and J. D. Teufel. Quantum nondemolition measurement of a nonclassical state of a massive object. *Phys. Rev. X*, 5:041037, 2015.

[9] C. F. Ockeloen-Korppi, E. Damskägg, J.-M. Pirkkalainen, M. Asjad, A. A. Clerk, F. Massel, M. J. Woolley, and M. A. Sillanpää. Stabilized entanglement of massive mechanical oscillators. *Nature*, 556:478, 2018.

[10] T. P. Purdy, P.-L. Yu, R. W. Peterson, N. S. Kampel, and C. A. Regal. Strong optomechanical squeezing of light. *Phys. Rev. X*, 3:031012, 2013.

[11] The L. I. G. O. Scientific Collaboration et al. A gravitational wave observatory operating beyond the quantum shot-noise limit. *Nat. Phys.*, 7:962, 2011.

[12] J. Aasi et al. Enhanced sensitivity of the ligo gravitational wave detector by using squeezed states of light. *Nat. Phot.*, 7:613, 2013.

[13] S. H. Mousavi, A.B. Khanikaev, and Z. Wang. Topologically protected elastic waves in phononic metamaterials. *Nat. Comm.*, 6:8682, 2015.

[14] X. He, C.and Ni, H. Ge, X. C. Sun, Y. B. Chen, M. H. Lu, X. P. Liu, and Y. F. Chen. Acoustic topological insulator and robust one-way sound transport. *Nat. Phys.*, 12:1124, 2016.

[15] C. Brendel, V. Peano, O. Painter, and F. Marquardt. Snowflake phononic topological insulator at the nanoscale. *Phys. Rev. B*, 97:020102, 2018.

[16] E. Gavartin, P. Verlot, and T. J. Kippenberg. A hybrid on-chip optomechanical transducer for ultrasensitive force measurements. *Nat. Nanotech.*, 7:509, 2012.

[17] H. Fu, T. H. Mao, Y. Li, J. F. Ding, J. D. Li, and G. Cao. Optically mediated spatial localization of collective modes of two coupled cantilevers for high sensitivity optomechanical transducer. *Appl. Phys. Lett.*, 105:014108, 2014.

[18] S. Mohammadi and A. Adibi. On chip complex signal processing devices using coupled phononic crystal slab resonators and waveguides. *AIP Adv.*, 1:041903, 2011.

[19] J. P. Mathew, J. del Pino, and E. Verhagen. Synthetic gauge fields for phonon transport in a nano-optomechanical system. *arXiv e-prints*, 1812.09369, 2018.

[20] I. Mahboob, K. Nishiguchi, A. Fujiwara, and H. Yamaguchi. Phonon lasing in an electromechanical resonator. *Phys. Rev. Lett.*, 110:127202, 2013.

[21] K. Fang, M. H. Matheny, X. Luan, and O. Painter. Optical transduction and routing of microwave phonons in cavity-optomechanical circuits. *Nat. Phot.*, 10:489, 2016.

[22] K. C. Balram, M. I. Davanço, J. D. Song, and K. Srinivasan. Coherent coupling between radiofrequency, optical and acoustic waves in piezo-optomechanical circuits. *Nat. Phot.*, 10:346, 2016.

[23] D. Hatanaka, A. Bachtold, and H. Yamaguchi. Electrostatically induced phononic crystal. *Phys. Rev. Appl.*, 11:024024, 2019.

[24] W. J. Venstra, H.J. R. Westra, and H. S. J. van der Zant. Mechanical stiffening, bistability, and bit operations in a microcantilever. *Appl. Phys. Lett.*, 97:193107, 2010.

[25] H. J. R. Westra, M. Poot, H. S. J. van der Zant, and W. J. Venstra. Nonlinear modal interactions in clamped-clamped mechanical resonators. *Phys. Rev. Lett.*, 105:117205, 2010.

[26] K. J. Lulla, R. B. Cousins, M. J. Venkatesan, A. andPatton, A. D. Armour, C. J. Mellor, and J. R. Owers-Bradley. Nonlinear modal coupling in a high-stress doubly-clamped nanomechanical resonator. *N. J. of Phys.*, 14:113040, 2012.

[27] A. Eichler, M. del Álamo Ruiz, J. A. Plaza, and A. Bachtold. Strong coupling between mechanical modes in a nanotube resonator. *Phys. Rev. Lett.*, 109:025503, 2012.

[28] W.J. Venstra, H. J. R. Westra, and H. S. J. van der Zant. Q-factor control of a microcantilever by mechanical sideband excitation. *Appl. Phys. Lett.*, 99:151904, 2011.

[29] I. Mahboob, V. Nier, K. Nishiguchi, A. Fujiwara, and H. Yamaguchi. Multi-mode parametric coupling in an electromechanical resonator. *Appl. Phys. Lett.*, 103:153105, 2013.

[30] J. P. Mathew, R. N. Patel, A. Borah, R. Vijay, and M. M. Deshmukh. Dynamical strong coupling and parametric amplification of mechanical modes of graphene drums. *Nat. Nanotech.*, 11:747, 2016.

[31] I. Mahboob, H. Okamoto, K. Onomitsu, and H. Yamaguchi. Two-mode thermal-noise squeezing in an electromechanical resonator. *Phys. Rev. Lett.*, 113:167203, 2014.

[32] M. H. Matheny, L. G. Villanueva, R. B. Karabalin, J. E. Sader, and M. L. Roukes. Nonlinear mode-coupling in nanomechanical systems. *Nano Lett.*, 13:1622, 2013.

[33] R. B. Karabalin, R. Lifshitz, M. C. Cross, M. H. Matheny, S. C. Masmanidis, and M. L. Roukes. Signal amplification by sensitive control of bifurcation topology. *Phys. Rev. Lett.*, 106:094102, 2011.

[34] D.K. Agrawal, J. Woodhouse, and A. A. Seshia. Synchronization in a coupled architecture of microelectromechanical oscillators. *J. of Appl. Phys.*, 115:164904, 2014.

[35] M. Pernpeintner, P. Schmidt, D. Schwienbacher, R. Gross, and H. Huebl. Frequency control and coherent excitation transfer in a nanostring-resonator network. *Phys. Rev. Appl.*, 10:034007, 2018.

[36] D. H. Antonio, D.and Zanette and D. López. Frequency stabilization in nonlinear micromechanical oscillators. *Nat. Comm.*, 3:806, 2012.

[37] P. Taheri-Tehrani, A. Guerrieri, M.l Defoort, A. Frangi, and D. Horsley. Mutual 3:1 subharmonic synchronization in a micromachined silicon disk resonator. *Appl. Phys. Lett.*, 111:183505, 2017.

[38] J. Güttinger, A. Noury, P. Weber, A. M. Eriksson, C. Lagoin, J. Moser, C. Eichler, A. Wallraff, A. Isacsson, and A. Bachtold. Energy-dependent path of dissipation in nanomechanical resonators. *Nat. Nanotech.*, 12:631, 2017.

[39] H. J. R. Westra, D. M. Karabacak, S. H. Brongersma, M. Crego-Calama, H. S. J. van der Zant, and W. J. Venstra. Interactions between directly- and parametrically-driven vibration modes in a micromechanical resonator. *Phys. Rev. B*, 84:134305, 2011.

[40] S. Houri, D. Hatanaka, M. Asano, R. Ohta, and H. Yamaguchi. Limit cycles and bifurcations in a nonlinear mems resonator with a 1:3 internal resonance. *Appl. Phys. Lett.*, 114:103103, 2019.

[41] Q. P. Unterreithmeier, E. M. Weig, and J. P. Kotthaus. Universal transduction scheme for nanomechanical systems based on dielectric forces. *Nature*, 458:1001, 2009.

[42] T. Faust, P. Krenn, S. Manus, J. P. Kotthaus, and E. M. Weig. Microwave cavity-enhanced transduction for plug and play nanomechanics at room temperature. *Nat. Comm.*, 3:728, 2012.

[43] W. Weaver, S. P. Timoshenko, D. H. Young. *Vibration problems in engineering*. John Wiley & Sons, 5th edition, 1990.

[44] K. Magnus, K. Popp, and W. Sextro. *Schwingungen: Grundlagen – Modelle – Beispiele*. Springer, 10th edition, 2016.

[45] A. Cleland. *Foundation of Nanomechanics*. Springer, 1th edition, 2003.

[46] L. Novotny. Strong coupling, energy splitting, and level crossings: A classical perspective. *Am. J. of Phys.*, 78:1199, 2010.

[47] M. Imboden and P. Mohanty. Dissipation in nanoelectromechanical systems. *Phys. Rep.*, 534:89, 2014.

[48] S. Schmid, L. G. Villanueva, and M. L. Roukes. *Fundamentals of Nanomechanical Resonators*. Springer, 1th edition, 2016.

[49] S. Schmid, M. Wendlandt, D. Junker, and C. Hierold. Nonconductive polymer microresonators actuated by the kelvin polarization force. *Appl. Phys. Lett.*, 89:163506, 2006.

[50] T. Faust, J. Rieger, M. J. Seitner, P. Krenn, J. P. Kotthaus, and E. M. Weig. Nonadiabatic dynamics of two strongly coupled nanomechanical resonator modes. *Phys. Rev. Lett.*, 109:037205, 2012.

[51] T. Faust, J. Rieger, M. J. Seitner, P. Krenn, J. P. Kotthaus, and E. M. Weig. Supplemental Material to "Nonadiabatic Dynamics of Two Strongly Coupled Nanomechanical Resonator Modes" (Ref. 50). *Phys. Rev. Lett.*, 109:037205, 2012.

[52] I. Wilson-Rae. Intrinsic dissipation in nanomechanical resonators due to phonon tunneling. *Phys. Rev. B*, 77:245418, 2008.

[53] G. D. Cole, I. Wilson-Rae, K. Werbach, M. R. Vanner, and M. Aspelmeyer. Phonon-tunnelling dissipation in mechanical resonators. *Nat. Comm.*, 2:231, 2011.

[54] J. Rieger. *AFM manipulation of damping in nanomechanical resonators*. phdthesis, Ludwig-Maximilians-Universitaet Muenchen, 2013.

[55] C. Harris, A. Piersol, and T. Paez. *Shock and Vibration Handbook*. McGraw-Hill Education Ltd, 6th edition, 2009.

[56] J. Rieger, A. Isacsson, M. J. Seitner, J. P. Kotthaus, and E. M. Weig. Energy losses of nanomechanical resonators induced by atomic force microscopy-controlled mechanical impedance mismatching. *Nat. Comm.*, 5:3345, 2014.

[57] K. Gajo, S. Schüz, and E. M. Weig. Strong 4-mode coupling of nanomechanical string resonators. *Appl. Phys. Lett.*, 111:133109, 2017.

[58] J. Rieger, T. Faust, M. J. Seitner, J. P. Kotthaus, and E. M. Weig. Frequency and Q factor control of nanomechanical resonators. *Appl. Phy. Lett.*, 101:103110, 2012.

[59] S. Schüz. Strong resonant mode-coupling between two doubly-clamped sin-nanobeam-resonators. mathesis, University of Konstanz, 2016.

[60] Z. Michalewicz. *Genetic Algorithms + Data Structures = Evolution Programs*. Springer, Berlin, Heidelberg, 3 edition, 19996.

[61] M. Mitchell. *An Introduction to Genetic Algorithms (Complex Adaptive Systems)*. The MIT Press, 1th edition, 1998.

[62] I. Gerdes, F. Klawonn, and R. Kruse. *Evolutionäre Algorithmen: Genetische Algorithmen - Strategien Und Optimierungsverfahren - Beispielanwendungen (Computational Intelligence)*. Vieweg, 1th edition, 2004.

[63] M. Schill. Dielektrische kontrolle gekoppleter nanomechanischer resonatoren. mathesis, University of Konstanz, 2018.

[64] C. Javerzac-Galy, K. Plekhanov, N. R. Bernier, L. D. Toth, A. K. Feofanov, and T. J. Kippenberg. On-chip microwave-to-optical quantum coherent converter based on a superconducting resonator coupled to an electro-optic microresonator. *Phys. Rev. A*, 94:053815, 2016.

[65] O. Kálmán, T. Kiss, J. Fortágh, and P. Domokos. Quantum Galvanometer by Interfacing a Vibrating Nanowire and Cold Atoms. *Nano Lett.*, 12:435, 2012.

[66] Z. Darázs, Z. Kurucz, O. Kálmán, T. Kiss, J. Fortágh, and P. Domokos. Parametric Amplification of the Mechanical Vibrations of a Suspended Nanowire by Magnetic Coupling to a Bose-Einstein Condensate. *Phys. Rev. Lett.*, 112:133603, 2014.

[67] M. I. Dykman and M. A. Krivoglaz. Theory of fluctuational transitions between stable states of a nonlinear oscillator. *Sov. Phys.*, 50:30, 1979.

[68] J. S. Huber, G. Rastelli, M. J. Seitner, J. Kölbl, W. Belzig, M. I. Dykman, and E. M. Weig. Squeezing of thermal fluctuations in a driven nanomechanical resonator. *arXiv e-prints*, 1903.07601, 2019.

[69] N. Kacem and S. Hentz. Bifurcation topology tuning of a mixed behavior in nonlinear micromechanical resonators. *Appl. Phys. Lett.*, 95:183104, 2009.

[70] M. J. Seitner, M. Abdi, A. Ridolfo, M. J. Hartmann, and E. M. Weig. Parametric oscillation, frequency mixing, and injection locking of strongly coupled nanomechanical resonator modes. *Phys. Rev. Lett.*, 118:254301, 2017.

[71] A. Noguchi, R. Yamazaki, M. Ataka, H. Fujita, Y. Tabuchi, T. Ishikawa, K. Usami, and Y. Nakamura. Ground state cooling of a quantum electromechanical system with a silicon nitride membrane in a 3d loop-gap cavity. *N. J. of Phys.*, 18:103036, 2016.

[72] M. A. Cohen, M. Yuan, B. W. A. de Jong, E. Beukers, S. J. Bosman, and G. A. Steele. A split-cavity design for the incorporation of a dc bias in a 3d microwave cavity. *Appl.Phys. Lett.*, 110:172601, 2017.

[73] E. Buks and M. L. Roukes. Electrically tunable collective response in a coupled micromechanical array. *J. of Microelectr. Sys.*, 11:802, 2002.

[74] P. Huang, L. Zhang, J. Zhou, T. Tian, P. Yin, C. Duan, and J. Du. Nonreciprocal radio frequency transduction in a parametric mechanical artificial lattice. *Phys. Rev. Lett.*, 117:017701, 2016.

[75] D. Hatanaka, I. Mahboob, K. Onomitsu, and H. Yamaguchi. Phonon waveguides for electromechanical circuits. *Nat. Nanotech.*, 9:520, 2014.

[76] J. Cha and C. Daraio. Electrical tuning of elastic wave propagation in nanomechanical lattices at mhz frequencies. *Nat. Nanotech.*, 13:1016, 2018.

[77] M. J. Seitner, K. Gajo, and E. M. Weig. Damping of metallized bilayer nanomechanical resonators at room temperature. *Appl. Phys. Lett.*, 105:213101, 2014.

[78] M. Abdi, M. Pernpeintner, R. Gross, H. Huebl, and M. J. Hartmann. Quantum state engineering with circuit electromechanical three-body interactions. *Phys. Rev. Lett.*, 114:173602, 2015.